

Global Biogeochemical Cycles®

RESEARCH ARTICLE

10.1029/2023GB007848

Key Points:

- Ocean models and machine learning estimates agree on the mean Southern Ocean CO₂ sink, but the trend since 2000 differs by a factor of two
- REgional Carbon Cycle Assessment and Processes Project Phase 2 estimates a 50% smaller Southern Ocean CO₂ sink for the same region and timeframe as RECCAP1
- Large model spread in summer and winter indicates that sustained efforts are required to understand driving processes in all seasons

Supporting Information:

Supporting Information may be found in the online version of this article.

Correspondence to:

J. Hauck,
judith.hauck@awi.de

Citation:

Hauck, J., Gregor, L., Nissen, C., Patara, L., Hague, M., Mongwe, P., et al. (2023). The Southern Ocean carbon cycle 1985–2018: Mean, seasonal cycle, trends, and storage. *Global Biogeochemical Cycles*, 37, e2023GB007848. <https://doi.org/10.1029/2023GB007848>

Received 19 MAY 2023

Accepted 2 OCT 2023

Author Contributions:

Conceptualization: Judith Hauck, Luke Gregor

Data curation: Judith Hauck, Luke Gregor, Cara Nissen, Lavinia Patara, Mark Hague, Precious Mongwe, Seth Bushinsky

Formal analysis: Judith Hauck, Luke Gregor, Cara Nissen, Lavinia Patara, Mark Hague, Precious Mongwe, Seth Bushinsky

Funding acquisition: Judith Hauck

© 2023, The Authors.

This is an open access article under the terms of the [Creative Commons Attribution License](#), which permits use, distribution and reproduction in any medium, provided the original work is properly cited.

The Southern Ocean Carbon Cycle 1985–2018: Mean, Seasonal Cycle, Trends, and Storage



Judith Hauck¹ , Luke Gregor² , Cara Nissen^{1,3} , Lavinia Patara⁴ , Mark Hague², Precious Mongwe⁵, Seth Bushinsky⁶ , Scott C. Doney⁷ , Nicolas Gruber² , Corinne Le Quéré⁸ , Manfredi Manizza⁹ , Matthew Mazloff⁹ , Pedro M. S. Monteiro^{5,10} , and Jens Terhaar^{11,12,13}

¹Alfred-Wegener-Institut, Helmholtz-Zentrum für Polar- und Meeresforschung, Bremerhaven, Germany, ²Environmental Physics, Institute of Biogeochemistry and Pollutant Dynamics, ETH Zurich, Zürich, Switzerland, ³Department of Atmospheric and Oceanic Sciences and Institute of Arctic and Alpine Research, University of Colorado Boulder, Boulder, CO, USA, ⁴GEOMAR Helmholtz Centre for Ocean Research Kiel, Kiel, Germany, ⁵Southern Ocean Carbon-Climate Observatory, CSIR, Pretoria, South Africa, ⁶University of Hawai'i Mānoa, Honolulu, HI, USA, ⁷Department of Environmental Sciences, University of Virginia, Charlottesville, VA, USA, ⁸School of Environmental Sciences, University of East Anglia, Norwich, England, ⁹Scripps Institution of Oceanography, University of California San Diego, La Jolla, CA, USA, ¹⁰School for Climate Studies, Stellenbosch University, Stellenbosch, South Africa, ¹¹Climate and Environmental Physics, Physics Institute, University of Bern, Bern, Switzerland, ¹²Oeschger Centre for Climate Change Research, University of Bern, Bern, Switzerland, ¹³Department of Marine Chemistry and Geochemistry, Woods Hole Oceanographic Institution, Falmouth, MA, USA

Abstract We assess the Southern Ocean CO₂ uptake (1985–2018) using data sets gathered in the REgional Carbon Cycle Assessment and Processes Project Phase 2. The Southern Ocean acted as a sink for CO₂ with close agreement between simulation results from global ocean biogeochemistry models (GOBMs, $0.75 \pm 0.28 \text{ PgC yr}^{-1}$) and *p*CO₂-observation-based products ($0.73 \pm 0.07 \text{ PgC yr}^{-1}$). This sink is only half that reported by RECCAP1 for the same region and timeframe. The present-day net uptake is to first order a response to rising atmospheric CO₂, driving large amounts of anthropogenic CO₂ (C_{anth}) into the ocean, thereby overcompensating the loss of natural CO₂ to the atmosphere. An apparent knowledge gap is the increase of the sink since 2000, with *p*CO₂-products suggesting a growth that is more than twice as strong and uncertain as that of GOBMs (0.26 ± 0.06 and $0.11 \pm 0.03 \text{ Pg C yr}^{-1} \text{ decade}^{-1}$, respectively). This is despite nearly identical *p*CO₂ trends in GOBMs and *p*CO₂-products when both products are compared only at the locations where *p*CO₂ was measured. Seasonal analyses revealed agreement in driving processes in winter with uncertainty in the magnitude of outgassing, whereas discrepancies are more fundamental in summer, when GOBMs exhibit difficulties in simulating the effects of the non-thermal processes of biology and mixing/circulation. Ocean interior accumulation of C_{anth} points to an underestimate of C_{anth} uptake and storage in GOBMs. Future work needs to link surface fluxes and interior ocean transport, build long overdue systematic observation networks and push toward better process understanding of drivers of the carbon cycle.

Plain Language Summary The ocean takes up CO₂ from the atmosphere and thus slows climate change. The Southern Ocean has long been known to be an important region for ocean CO₂ uptake. Here, we bring together all available data sets that estimate the Southern Ocean CO₂ uptake, from models that simulate ocean circulation and physical and biological processes that affect the ocean carbon cycle, from surface ocean observation-based estimates, from atmospheric transport models that ingest atmospheric CO₂ observations, and from interior ocean biogeochemical observations. With these data sets, we find good agreement on the mean Southern Ocean CO₂ uptake 1985–2018, which is 50% smaller than previous estimates when recalculated for the time period and spatial extent used in the previous estimate. However, the estimates of the temporal change of the Southern Ocean CO₂ uptake differ by a factor of two and thus are not in agreement. We further highlight that knowledge gaps exist not only in winter when observations are typically rare, but equally in summer when biology plays a larger role, which is typically represented too simplistically in the dynamic models.

1. Introduction

The Southern Ocean (Figure 1) is the primary conduit between the surface and the deep ocean (Morrison et al., 2022; Talley, 2013) making it a key region for the global carbon cycle and the climate system across time-scales from paleo to present day and into the future (Canadell et al., 2021). First, water mass formation of

Investigation: Judith Hauck, Luke Gregor, Cara Nissen, Lavinia Patara, Mark Hague, Precious Mongwe, Seth Bushinsky

Methodology: Judith Hauck, Luke Gregor, Cara Nissen, Lavinia Patara, Mark Hague, Precious Mongwe, Seth Bushinsky

Project Administration: Judith Hauck, Luke Gregor, Nicolas Gruber

Software: Judith Hauck, Luke Gregor, Cara Nissen, Lavinia Patara, Mark Hague, Precious Mongwe, Seth Bushinsky

Supervision: Judith Hauck, Luke Gregor, Nicolas Gruber

Visualization: Judith Hauck, Luke Gregor, Cara Nissen, Lavinia Patara, Mark Hague, Precious Mongwe, Seth Bushinsky

Writing – original draft: Judith Hauck, Luke Gregor, Cara Nissen, Lavinia Patara, Mark Hague, Precious Mongwe, Scott C. Doney, Manfredi Manizza, Matthew Mazloff

Writing – review & editing: Judith Hauck, Luke Gregor, Cara Nissen, Lavinia Patara, Mark Hague, Precious Mongwe, Seth Bushinsky, Scott C. Doney, Nicolas Gruber, Corinne Le Quéré, Manfredi Manizza, Matthew Mazloff, Pedro M. S. Monteiro, Jens Terhaar

Antarctic surface water occurs during large-scale upwelling of deep, old and carbon-rich water masses due to strong westerly winds (Marshall & Speer, 2012; Russell et al., 2006). Part of this water moves northwards by Ekman transport and contributes to the formation of Southern mode and intermediate waters (Ito et al., 2010; Morrison et al., 2022; Sallée et al., 2012) together with subtropical water masses (Iudicone et al., 2016). Another part moves southward and circulates in the large gyres of the Weddell and Ross Seas (Klatt et al., 2005). A fraction of these Antarctic surface waters densify on the Antarctic shelves through cooling and brine rejection during sea-ice formation on the Antarctic shelves to then flow down the Antarctic slope and form Antarctic Bottom Water (Jacobs, 2004; Orsi et al., 1999).

In pre-industrial times, the Southern Ocean was a net source of CO_2 to the atmosphere due to upwelling of carbon-rich deep waters (Mikaloff Fletcher et al., 2007). Importantly, the large-scale upwelling that drove the natural outgassing fluxes in the polar and subpolar Southern Ocean still occurs today. However, since industrialization, increasing atmospheric levels of CO_2 have shifted the equilibrium of CO_2 partial pressure between the ocean and the atmosphere in the favor of the latter, thus overcompensating the natural outgassing (e.g., Hoppema, 2004). The contemporary net flux in the Southern Ocean can thus be understood as the sum of the outgassing of natural CO_2 and uptake of anthropogenic CO_2 (Gruber et al., 2009; Gruber, Landschützer, & Lovenduski, 2019). Importantly, the Southern Ocean has acted as the primary region of uptake for anthropogenic CO_2 (Caldeira & Duffy, 2000; Frölicher et al., 2015; Khatiwala et al., 2009; Mikaloff Fletcher et al., 2006; Orr et al., 2001; Sarmiento et al., 1992), which is attributed to upwelling of old water masses (with low anthropogenic carbon) in a region of high wind speeds, as well as subsequent transport of excess carbon from the surface into the ocean interior through the formation of Subantarctic Mode and Antarctic Intermediate Water (Bopp et al., 2015; Langlais et al., 2017; Mikaloff Fletcher et al., 2006; Sallée et al., 2012; Waugh et al., 2006). In the absence of evidence of substantial changes in the biological carbon pump over the past decades, the role of biology for anthropogenic carbon uptake is thought to be small (Holzer & DeVries, 2022; Murnane et al., 1999). However, the biological carbon pump can have a strong imprint on the net fluxes during the summer when primary production draws down natural CO_2 at the surface (e.g., Bakker et al., 1997; Hoppema et al., 1995, 1999; E. Jones et al., 2012, 2015) despite it being generally considered inefficient due to widespread limitation by iron (De Baar et al., 1995; Ryan-Keogh et al., 2023; Smetacek et al., 2012) and possibly other trace metals (Browning et al., 2021).

While the general importance of the Southern Ocean for the ocean carbon sink is recognized, it is also the region with the largest uncertainty in the mean and trend of the sink (Friedlingstein et al., 2022; Hauck et al., 2020). This is partly because the observation-based estimates and model-based estimates measure different components of the ocean carbon sink, and assumptions on fluxes associated with river discharge need to be made, which carry high uncertainty themselves (Aumont et al., 2001; Lacroix et al., 2020). Further, the decadal variability of the Southern Ocean and the underlying mechanisms thereof are a key contributor to the uncertainty and are a topic of continued discussion (Canadell et al., 2021; Gruber, Landschützer, & Lovenduski, 2019; Hauck et al., 2020; Landschützer et al., 2015; Le Quéré et al., 2007; McKinley et al., 2020). A stagnation in the growth of the Southern Ocean carbon sink in the 1990s is commonly attributed to a strengthening of the westerly winds and associated intensified upwelling of carbon- and nutrient-rich deep water (Hauck et al., 2013; Le Quéré et al., 2007; Lovenduski et al., 2007). Indeed, evidence for this stronger upwelling is indirectly observed by enhanced surface nutrient concentrations in all Southern Ocean basins (Ayers & Strutton, 2013; Hoppema et al., 2015; T. Iida et al., 2013; Panassa et al., 2018; Pardo et al., 2017). The early 2000's marked the start of the so-called reinvigoration of the Southern Ocean carbon sink (Landschützer et al., 2015). The strength of the reinvigoration is uncertain due to the observation-based products potentially overestimating the trends owing to data sparsity (Gloege et al., 2021; Hauck et al., 2023; Landschützer et al., 2015), while further analysis on the trends in the models is needed. Furthermore, the drivers of the reinvigoration are less well understood than for the stagnation, but may be linked to changes in the atmospheric forcing (Gruber, Landschützer, & Lovenduski, 2019) and/or changes in the overturning circulation (DeVries et al., 2017). There is also evidence that both the stagnation and the reinvigoration are part of a global response to variations in atmospheric CO_2 growth rate, ocean temperature and circulation induced by the 1992 eruption of Mount Pinatubo (Eddebar et al., 2019; McKinley et al., 2020).

The Southern Ocean carbon sink is projected to continue to play an important role in the future carbon cycle as shown by Earth System Model simulations (Canadell et al., 2021; Hauck et al., 2015; Kessler & Tjiputra, 2016; Terhaar et al., 2021). However, there are indications that system changes may occur, such as a shift to a larger proportion of the CO_2 uptake occurring in the polar Southern Ocean (Hauck et al., 2015), and a strong sensitivity

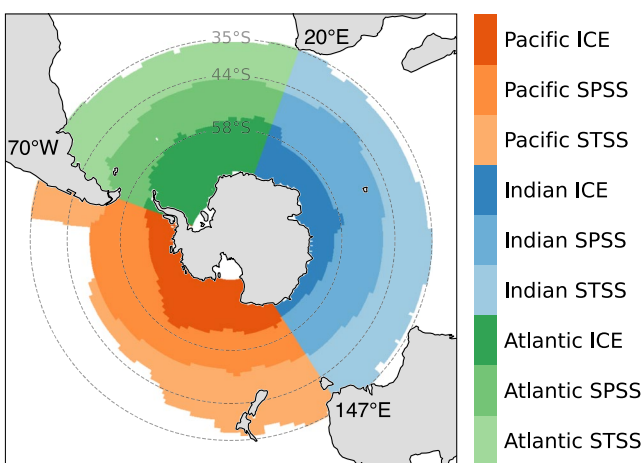


Figure 1. Study region. The Southern Ocean covers three biomes: The subtropical seasonally stratified (STSS), the subpolar seasonally stratified (SPSS), and the ice (ICE) biome. The biomes are defined following Fay and McKinley (2014). We further consider the Atlantic, Pacific, and Indian Ocean sectors separately in parts of the analysis. The dashed lines show the REgional Carbon Cycle Assessment and Processes Project Phase 2 Southern Ocean northernmost extent (35°S), the RECCAP1 Southern Ocean northernmost extent (44°S), and RECCAP1's boundary for the circumpolar region (58°S).

of Southern Ocean carbon storage to physical ventilation and warming (Bourgeois et al., 2022; Katavouta & Williams, 2021; Terhaar et al., 2021).

In this study, we aim to synthesize and assess information on the Southern Ocean carbon sink over the period 1985 to 2018 in the framework of the REgional Carbon Cycle Assessment and Processes project, Phase 2 (RECCAP2). This work builds on a previous assessment, RECCAP Phase 1 (referred to as RECCAP1 for clarity), for the period 1990 to 2009 (Lenton et al., 2013). In RECCAP1, the Southern Ocean was defined as the ocean south of 44°S (building on earlier classification in the atmospheric inversion community), which, however, cut through the major anthropogenic CO₂ uptake region at the northern edge of the Southern Ocean. The assessment was based on five global ocean biogeochemical models, 11 atmospheric inversions, 10 ocean inversions and a single *p*CO₂ observation-based data set, the climatology of Takahashi et al. (2009). RECCAP1 resulted in a best estimate of the net Southern Ocean CO₂ uptake (1990–2009) of $0.42 \pm 0.07 \text{ PgC yr}^{-1}$ based on all models (including inversions), with a surface *p*CO₂-based climatology (Takahashi et al., 2009) suggesting a lower number of $0.27 \pm 0.13 \text{ PgC yr}^{-1}$ Lenton et al. (2013). The interannual variability was estimated to be $\pm 25\%$ around this mean value. The largest proportion of the mean flux occurred in the region 44–58°S which spans large parts of the Subantarctic Zone and of the Polar Frontal Zone with similar contributions from the Atlantic, Pacific and Indian Ocean sectors. In the Antarctic Zone (south of 58°S), individual estimates did not agree on the sign of the net CO₂ flux.

A major advance since RECCAP1 is the release and ongoing updates of the Surface Ocean CO₂ Atlas (SOCAT, Bakker et al., 2016), which currently provides 33.7 million quality-controlled and curated surface ocean *p*CO₂ measurements with an accuracy of $<5 \text{ \mu atm}$ in the 2022 release (Bakker et al., 2022). The release of SOCAT allowed for the development of the surface ocean *p*CO₂ observation-based products (*p*CO₂-products) that interpolate and extrapolate sparse ship-based observations from SOCAT to global coverage. Based on these maps of surface *p*CO₂, the air-sea CO₂ flux is then calculated using gas-exchange parameterizations and input data fields such as sea surface temperature (SST) and wind fields (Wanninkhof, 2014). Since RECCAP1, a diverse set of statistical and machine-learning approaches have been developed (e.g., Chau et al., 2022; Gregor et al., 2019; Landschützer et al., 2014; Rödenbeck et al., 2014). The *p*CO₂-products allowed for observation-based investigation of interannual and decadal variability. They confirmed the reported stagnation of the Southern Ocean carbon sink in the 1990s (Le Quéré et al., 2007), and identified the aforementioned reinvigoration in the 2000s (Landschützer et al., 2015; Ritter et al., 2017). However, these *p*CO₂-products have made the Southern Ocean's long-standing issue of sparse observations even more evident. Observing system simulation experiments (OSSEs) have shown that these methods are prone to regional and temporal biases (Denvil-Sommer et al., 2021) and some *p*CO₂-products may overestimate the decadal variability by 30% (Gloege et al., 2021). In fact, a recent study showed that the SOM-FFN *p*CO₂-product used in the reinvigoration study of Landschützer et al. (2015) overestimates the model-based decadal trend 2000–2018 by 130% in an ocean model subsampling experiment (Hauck et al., 2023). However, these OSSEs have also shown that augmenting ship-based observations with well-placed, high accuracy *p*CO₂ observations from autonomous platforms can reduce these biases (Denvil-Sommer et al., 2021; Djeutchouang et al., 2022; Gloege et al., 2021; Hauck et al., 2023).

The gap in ship-based *p*CO₂ observations is slowly being addressed by a second major advance, that is autonomous measurement devices. Among these are pH-equipped biogeochemical Argo floats (BGC-floats) (Johnson et al., 2017; Williams et al., 2016). With this approach, float pH measurements are combined with multi-linear regression-derived alkalinity (Carter et al., 2016, 2018, 2021; Williams et al., 2016), to estimate *p*CO₂. Although uncertainties of the BGC-float based estimates of *p*CO₂ are, to date, higher (theoretical uncertainty of 11 \mu atm , Williams et al., 2017) than for direct *p*CO₂ measurements (2 \mu atm , Bakker et al., 2016), some of these indirect *p*CO₂ estimates fill critical gaps in the sparsely sampled winter months. These novel data, either on their own (Gray et al., 2018) or as additional input for *p*CO₂-products (Bushinsky et al., 2019), reported a strong winter outgassing of CO₂ in the subpolar Southern Ocean for the years 2015 through 2017 that also led to a substantially smaller estimate of the annual Southern Ocean CO₂ uptake for these years. However, these larger-than-expected

winter outgassing estimates were challenged by airborne flux estimates and direct $p\text{CO}_2$ measurements from a circumpolar navigation by an uncrewed sailing drone (Long et al., 2021; Sutton et al., 2021). The sailing drone observations were in agreement with ship-based $p\text{CO}_2$ -product estimates throughout all seasons (Sutton et al., 2021). The authors attributed the discrepancy between BGC-floats and other estimates to either a bias of the float measurement devices or interannual variability. In support of the latter argument, the BGC-Argo-based air-sea CO_2 flux in the years 2017–2019 also did not reveal the strong winter outgassing signal of the years 2015 and 2016 (Sutton et al., 2021).

Another advance since RECCAP1 is that more global ocean biogeochemical models (GOBMs) have become available with improvements in resolution and physical and biogeochemical process representation (Friedlingstein et al., 2022; Wanninkhof et al., 2013). While the ability of the GOBMs to capture interannual variability of air-sea CO_2 fluxes (FCO_2) was questioned by the larger variability of $p\text{CO}_2$ -product estimates (Le Quéré et al., 2018), the lower interannual variability of GOBMs now falls within the range of the larger ensemble of $p\text{CO}_2$ -products (Hauck et al., 2020; McKinley et al., 2020). For the decadal variability of FCO_2 , there is a moderate agreement between GOBMs and $p\text{CO}_2$ -products on a stagnation of the sink in the 1990s and an increase of the sink in 2002–2011 but with a larger amplitude of the multi-year/decadal variability in the $p\text{CO}_2$ -products (Gruber et al., 2023; Hauck et al., 2020; McKinley et al., 2020). Although the GOBMs compare reasonably well to global and Southern Ocean observations of surface ocean $p\text{CO}_2$ (Hauck et al., 2020), their estimates of the global ocean carbon sink remain below those of interior ocean anthropogenic carbon accumulation estimates from 1994 to 2007 (Gruber, Clement, et al., 2019), atmospheric inversions, observed O_2/N_2 ratios (Friedlingstein et al., 2022; Tohjima et al., 2019), and a similar underestimation was found in Earth System Models (Terhaar et al., 2022).

The final major advance in the last decade are regional and global data-assimilating global ocean biogeochemistry models (Carroll et al., 2020; Verdy & Mazloff, 2017). These models bring together the process-based knowledge from GOBMs, but use data assimilation schemes to minimize mismatches between simulated fields, and physical and biogeochemical observations.

Despite these recent advances in observations and models, the Southern Ocean is still the region with the largest discrepancy in mean CO_2 flux (although within the uncertainty of the fluxes associated with river discharge, which are implicitly included in the observation-based estimates, but not in the models, see Sections 2.2.1 and 2.3.1) and variability, as well as largest model spread (Canadell et al., 2021; Fay & McKinley, 2021; Friedlingstein et al., 2022). In this study, we aim to quantify the Southern Ocean (following the RECCAP2 biome shown in Figure 1) surface CO_2 fluxes and interior storage of anthropogenic carbon over the period 1985–2018 from different classes of models and observations, and to identify knowledge gaps and ways forward.

This study is organized in the following way. In our methods, we describe the region (Section 2.1), the data sets that we use throughout this synthesis (Section 2.2), and how the data were processed (Section 2.3). Our results contain first the estimates of the mean fluxes 1985–2018 and their decomposition into anthropogenic and natural fluxes, and atmospheric CO_2 versus climate effects (Section 3.1). This is followed by an analysis of summer and winter fluxes and the full seasonal cycle, where we also decompose $p\text{CO}_2$ into seasonal thermal and non-thermal contributions (Section 3.2). In an annually resolved perspective, we revisit mean fluxes accounting for data sets with short temporal coverage (Section 3.3) before we then analyze the regionally averaged temporal trends of CO_2 flux (Section 3.4). The latter also encompasses a $p\text{CO}_2$ comparison with in situ $p\text{CO}_2$ observations, as well as atmospheric CO_2 and climate effects as drivers of the trends. In the final part of the results, the study then evaluates the GOBM simulation results with observation-based estimates of ocean interior storage of anthropogenic carbon in the Southern Ocean (Section 3.5). The discussion first summarizes the results with a comparison of the RECCAP1 and RECCAP2 results (Section 4.1). We also discuss the drivers of the seasonal cycle (Section 4.2), the interannual and decadal variability (Section 4.3), and the zonal asymmetry of the fluxes in the Southern Ocean (Section 4.4). Lastly, we discuss how our study links with and can inform observational programs (Section 4.5), before presenting a conceptual characterization of the Southern Ocean carbon cycle in the conclusions (Figure 14 in Section 5).

2. Methods

2.1. Regions

We use the RECCAP2 regions (De Vries et al., 2023) to define the Southern Ocean and its northern boundary (Figure 1). This definition of the Southern Ocean covers the subtropical seasonally stratified biome (STSS), the

Table 1

Overview of Data Sets Used in This Paper (Continued in Table 2)

| Data set | Time period | Specific information | Reference |
|---|-------------|----------------------|---|
| Global ocean biogeochemistry models | | | |
| CCSM-WHOI | 1985–2017 | A, B, C, D | Doney et al. (2009) |
| CESM-ETHZ | 1985–2018 | A, B, C, D | Lindsay et al. (2014) and S. Yang and Gruber (2016) |
| CNRM-ESM2-1 | 1985–2018 | A, B, C, D | Séférian et al. (2019), Berthet et al. (2019), and Séférian et al. (2020) |
| EC-Earth3 | 1985–2018 | A, B, C, D | Dösscher et al. (2022) |
| FESOM-RECoM-HR | 1985–2018 | A, B | Hauck et al. (2013) and Schourup-Kristensen et al. (2014, 2018) |
| FESOM-RECoM-LR | 1985–2018 | A, B, C, D | Hauck et al. (2013), Schourup-Kristensen et al. (2014), and Hauck et al. (2020) |
| MOM6-Princeton | 1985–2018 | A, B | Liao et al. (2020) and Stock et al. (2020) |
| MPIOM-HAMOCC | 1985–2018 | A, B, C, D | Ilyina et al. (2013), Paulsen et al. (2017), and Mauritsen et al. (2019) |
| MRI-ESM2-1 | 1985–2018 | A, B, C, D | Urakawa et al. (2020) |
| NorESM-OC1.2 | 1985–2018 | A, B, C, D | Schwinger et al. (2016) |
| ORCA025-GEOMAR | 1985–2018 | A, B, C, D | Madec and the NEMO team (2016), Kriest and Oschlies (2015), and Chien et al. (2022) |
| ORCA1-LIM3-PISCES (IPSL-NEMO-PISCES) | 1985–2018 | A, B, C, D | Aumont et al. (2015) |
| NEMO-PlankTOM12.1 | 1985–2018 | A, B, C, D | Le Quéré et al. (2016), Buitenhuis et al. (2019), and Wright et al. (2021) |
| Regional ocean biogeochemical models | | | |
| ROMS-SouthernOcean-ETHZ | 1985–2018 | A, B, D | A. Haumann (2016) and Nissen et al. (2018) |
| Data-assimilated models | | | |
| B-SOSE | 2013–2018 | | Verdy and Mazloff (2017) |
| ECCO-Darwin | 1992–2017 | | Carroll et al. (2020, 2022) |
| OCIMv2021 | 1780–2018 | A, B, C | DeVries (2022) |

Note. Sorted by data class, here: Global Ocean Biogeochemistry Models (GOBMs), Regional Ocean Biogeochemistry Model, and data assimilated models.

subpolar seasonally stratified biome (SPSS), and the ice biome (ICE) and is based on the global open ocean biome classification of Fay and McKinley (2014). This covers a larger area than the definition used in RECCAP1 (44–58°S, 58–75°S, Lenton et al., 2013) and has the advantage that it does not cut through the subtropical region with its large CO₂ flux into the ocean. The northernmost extent of the Southern Ocean in this definition is 35°S. For parts of our analysis, we further separate the Atlantic, Indian, and Pacific Ocean sectors along longitudes of 20°E, 147°E, and 290°E (Figure 1).

2.2. Data Sets

Here, we introduce data sets across four different data classes that are used for the assessment of the Southern Ocean CO₂ fluxes and storage, namely: ocean biogeochemistry models (14), surface pCO₂-based data-products (11), data assimilated and ocean inverse models (3), and atmospheric inversion models (6).

2.2.1. Ocean Biogeochemistry Models

We used 13 global ocean biogeochemistry models (GOBMs) and 1 regional ocean biogeochemistry model (Table 1). These models simulate ocean circulation and biogeochemical fluxes caused by physics (advection, mixing, gas-exchange) and by biological processes. They are forced with atmospheric fields from reanalysis products, for example, by either heat and freshwater fluxes directly or by air temperature, wind speed, precipitation and humidity, which are converted to heat and freshwater fluxes using bulk formulae (see references in Table 1; Large et al., 1994). From these 14 models, 11 models are global ocean models with roughly 1° × 1°

Table 2
Overview of Data Sets Used in This Paper (Continued)

| Data set | Time period | Specific information | References |
|--------------------------------------|-----------------------|---|-----------------------------------|
| pCO₂-products | | | |
| AOML-EXTRAT | 1998–2018 | | Wanninkhof (2023) |
| CMEMS-LSCE-FFNN | 1985–2018 | | Chau et al. (2022) |
| CSIR-ML6 | 1985–2018 | | Gregor et al. (2019) |
| Jena-CarboScope (Mixed layer scheme) | 1985–2018 | | Rödenbeck et al. (2013, 2022) |
| JMA-MLR | 1985–2018 | | Y. Iida et al. (2021) |
| LDEO-HPD | 1985–2018 | | Gloege et al. (2022) |
| NIES-ML3 | 1985–2018 | | Zeng et al. (2022) |
| OceanSODA-ETHZ | 1985–2018 | | Gregor and Gruber (2021) |
| MPI-SOM-FFN | 1985–2018 | | Landschützer et al. (2016, 2020) |
| Jena-CarboScope (SOCCOM) | 2015–2018 | | Bushinsky et al. (2019) updated |
| MPI-SOM-FFN (SOCCOM) | 2015–2018 | | Bushinsky et al. (2019) updated |
| Watson2020 | 1988–2018 | | Watson et al. (2020) |
| LDEO-climatology (Takahashi legacy) | Climatology | | Takahashi et al. (2009) |
| Atmospheric inversions | | | |
| Jena CarboScope | 1957–2020 (1990–2020) | CarboScope pCO ₂ -product | Rödenbeck et al. (2018) |
| CAMS | 1979–2020 (1990–2020) | CMEMS-LSCE-FFNN pCO ₂ -product | Chevallier et al. (2005) |
| NISMON-CO ₂ | 1990–2020 | JMA-MLR pCO ₂ -product | Niwa et al. (2017) |
| CarbonTrackerEurope (CTE) | 2001–2020 | CarboScope pCO ₂ -product | van der Laan-Luijkx et al. (2017) |
| UoE | 2001–2020 | Takahashi climatology | Feng et al. (2016) |
| CMS-Flux | 2010–2020 | MOM6 GOBM | Liu et al. (2021) |

Note. Sorted by data class, here: pCO₂-products and atmospheric inversions. The atmospheric inversions were provided only since 1990.

resolution, and two global models (FESOM_RECoM_HR and ORCA025-GEOMAR) and the regional model (ROMS-SouthernOcean-ETHZ) are available in ca. $0.25^\circ \times 0.25^\circ$ resolution. Details of global model set-ups are given in DeVries et al. (2023). The ROMS-based regional Southern Ocean model has a northern boundary at 24°S .

For the ocean-models listed above, up to four different simulations were provided (see also Table S1 in Supporting Information S1 and DeVries et al., 2023). These differ in whether atmospheric CO₂ and all other atmospheric forcing variables vary on interannual time scales, are repeated for a single year, or follow a multi-year climatology. In simulation A, the historical run, both atmospheric CO₂ and all other physical forcing variables vary on interannual time scales. In simulation B, the preindustrial control run, a repeated year or climatological physical atmospheric forcing is used, and the atmospheric CO₂ levels are held constant at pre-industrial levels. In simulation C, the atmospheric CO₂ varies interannually and only the physical atmospheric forcing is climatological. In simulation D, the atmospheric CO₂ levels are held constant at pre-industrial levels, whereas the physical atmospheric forcing varies interannually. These simulations allow for the separation of the effects of the increase in atmospheric CO₂ and climate change and variability on air-sea CO₂ fluxes: the steady-state and non-steady state components of both natural and anthropogenic carbon. Here *anthropogenic* refers to the direct effect of increasing atmospheric CO₂ and *non-steady state* encompasses the effects of climate change and variability. For a detailed explanation, please see DeVries et al. (2023) and further explanation in Le Quéré et al. (2010), McNeil and Matear (2013), Hauck et al. (2020), Crisp et al. (2022), and Gruber et al. (2023). Simulation A includes all components of the carbon fluxes. In the control simulation B, only the steady-state component of natural carbon is considered. In simulation C, only the steady-state components of both natural and anthropogenic carbon are accounted for. Finally, in simulation D, only the steady state and non-steady state components of natural carbon are represented.

The majority of models do not account for the river-induced outgassing of carbon (DeVries et al., 2023; Terhaar et al., 2023), hence the air-sea CO₂ flux in simulation A corresponds to the S_{OCEAN} definition used in the Global

Carbon Budget (Friedlingstein et al., 2022), which differs from $p\text{CO}_2$ -product estimates by the river-induced term. Note that the river-induced term will be discussed in greater detail in Section 4.1. In addition, simulation A may include a model bias (mean offset) and drift (temporally changing offset). We assess the model drift of the air-sea CO_2 flux by calculating the linear trend of the integrated CO_2 flux time series for the period 1985–2018 in simulation B for each model and each biome. The time series plots and the linear trends reported in Figure 8 are drift corrected by subtracting the trend from simulation B. We note that this drift-correction only marginally impacts the reported trends in the result section, as the trends in simulation B are small compared to the mean fluxes for all models (see Text S1 and Figure S1 in Supporting Information S1). In contrast to a global bias (any deviation of the global mean CO_2 flux from 0 in simulation B, see Hauck et al. (2020)), the regional bias in the simulated flux cannot be assessed by the set of simulations as it cannot be separated from the natural steady-state air-sea CO_2 flux (Terhaar et al., 2023), which is non zero on a regional level.

We use the full suite of models in all analyses, with two exceptions. First, we excluded the MPIOM-HAMOCC model in all seasonal analyses (Figures 4–7) because its amplitude of the seasonal cycle is a factor 3–6 larger than in the other models in the three main Southern Ocean biomes (Figure S2 in Supporting Information S1), and including this outlier would skew the ensemble mean disproportionately. The exaggerated seasonal cycle in the MPIOM-HAMOCC model was found in earlier studies and is attributed to excessive net primary production in the Southern Ocean (Mongwe et al., 2018). Second, the decomposition into natural and anthropogenic CO_2 fluxes was not possible with GOBMs that only provided simulations A and B (MOM6-Princeton and FESOM-RECoM-HR). See Section 2.3.5 for further restrictions on GOBM use and interpretation for the interior ocean anthropogenic carbon accumulation.

2.2.2. Surface $p\text{CO}_2$ -Based Data-Products

As a second data class, we use surface ocean $p\text{CO}_2$ observation-based data products ($p\text{CO}_2$ -products) (Table 2, for more details see DeVries et al. (2023)). These $p\text{CO}_2$ -products extrapolate or interpolate sparse ship-based measurements of $p\text{CO}_2$ using statistical modeling approaches. All $p\text{CO}_2$ -based data-products use SOCAT as the target data set. The majority of $p\text{CO}_2$ -products use similar gridded prediction data sets to fill the gaps, including SST, sea surface salinity (SSS), mixed-layer depth, and chlorophyll-a estimates for the open ocean. We use eight such $p\text{CO}_2$ -products that all cover the full time-series 1985–2018 for the ensemble mean of $p\text{CO}_2$ -products. AOML_EXTRAT covers a shorter period, and is thus not included in the ensemble mean 1985–2018, but is included in the ensemble mean 2015–2018. The largest methodological difference between the $p\text{CO}_2$ -products stems from the algorithm choice. The majority of the methods use regression approaches (a.k.a. machine learning) such as artificial neural networks (e.g., MPI-SOM-FFN) and gradient boosted decision trees (e.g., CSIR-ML6) to capture the relationship between the ship-based measurements and the predictor variables. The Jena-CarboScope product includes a mechanistic understanding of mixing, entrainment, and fluxes of CO_2 into and out of the mixed layer (Rödenbeck et al., 2014). The HPD-LDEO method adjusts global ocean biogeochemistry model estimates of $p\text{CO}_2$ to be closer to observed ship-based measurements and is thus an observation-based posterior correction to the GOBM estimates (Gloegel et al., 2022).

Further, two additional variants of MPI-SOM-FFN and Jena-CarboScope by Bushinsky et al. (2019, ship + float estimates are used here) include additional BGC-float-derived $p\text{CO}_2$ for the Southern Ocean (referred to as BGC-float $p\text{CO}_2$ -products, 2015–2018). We also use the Watson2020 product, which is a neural network approach (based on MPI-SOM-FFN) but applies an adjustment to SOCAT $p\text{CO}_2$ that accounts for the difference between ship intake temperature and satellite SST (Watson et al., 2020). The BGC-float $p\text{CO}_2$ -products (2015–2018) and Watson2020 (1988–2018) are not included in the $p\text{CO}_2$ -product ensemble averages, as they are based on fundamentally different $p\text{CO}_2$ values. We also use a monthly climatology product (LDEO-clim) that is centered on the year 2010 (Takahashi et al., 2009). The LDEO-clim product fills the gaps using a combination of inverse distance weighted interpolation and a diffusive-advection interpolation scheme (Takahashi et al., 2009). Note that this product is only used in representations of the seasonal cycle, and not for trend analyses. All these $p\text{CO}_2$ -products estimate the bulk air-sea CO_2 flux with:

$$FCO_2 = K_0 \cdot k_w \cdot (p\text{CO}_2^{\text{sea}} - p\text{CO}_2^{\text{atm}}) \cdot (1 - \text{ice}) \quad (1)$$

where K_0 is the solubility of CO_2 in seawater, k_w is the gas transfer velocity, $p\text{CO}_2^{\text{sea}}$ is the oceanic estimate of $p\text{CO}_2$ from the $p\text{CO}_2$ -product, $p\text{CO}_2^{\text{atm}}$ is the atmospheric $p\text{CO}_2$, and ice is the sea-ice fraction, with the majority of the open ocean having a fraction of 0. Other than $p\text{CO}_2^{\text{sea}}$, k_w is the largest source of uncertainty in the

calculation of bulk air-sea CO_2 fluxes (Wanninkhof, 2014; Fay et al., 2021). However, most of the $p\text{CO}_2$ -products use a quadratic formulation of k_w as described by Wanninkhof et al. (1993) meaning that the product spread is reduced due to similar choices—details are shown in Global chapter's Table S2 in Supporting Information S1 (DeVries et al., 2023). An exception is the Watson2020 product (Watson et al., 2020) that calculates air sea CO_2 fluxes using the formulation described in Woolf et al. (2016) where a cool and salty skin adjustment is applied.

2.2.3. Data-Assimilated Models

We use three data-assimilating models (Table 1). The Biogeochemical Southern Ocean State Estimate (B-SOSE, Verdy & Mazloff, 2017) is an eddy-permitting 1/6-degree resolution data-assimilating model, which assimilates the data from Southern Ocean Carbon and Climate Observations and Modeling (SOCCOM) BGC-Argo floats as well as shipborne and other autonomous observations (i.e., GLODAP and SOCAT) over the period 2013–2018. In situ and satellite observations of the physical state are also assimilated. B-SOSE is based on the MIT general circulation model (MITgcm, Campin et al., 2011) and uses software developed by the consortium for Estimating the Circulation and Climate of the Ocean (ECCO, Stammer et al., 2002; Wunsch & Heimbach, 2013) to build on the SOSE physical model framework by adding the Nitrogen version of the Biogeochemistry with Light, Iron, Nutrients, and Gases (N-BLING; evolved from Galbraith et al. (2010)) biogeochemical model. Consistency with the data is achieved by systematically adjusting the model initial conditions and the atmospheric state through the 4D-Var assimilation methodology. This B-SOSE assimilation methodology does not break the model biogeochemical or physical budgets. The budgets are closed, which allows one to understand signal attribution, though limits the control over the solution. For this reason B-SOSE is only consistent with the data on the timescales longer than approximately 90 days; the mesoscale eddies are reproduced statistically and not deterministically. Even with this assimilation methodology some seasonal biases still exist, and B-SOSE is still a work in progress.

The ECCO-Darwin data-assimilation model (Carroll et al., 2020) is based on a global ocean and sea ice configuration (about 1/3°) of the MIT general circulation model and is available from January 1992 to December 2017. Besides being global and covering a longer duration than B-SOSE, this product also uses a different biogeochemical model and assimilation technique. The ECCO circulation estimates used in this version are coupled online with the Darwin ecosystem model (Dutkiewicz et al., 2009), which represents the planktonic ecosystem dynamics coupled with biogeochemical cycles in the ocean. The Wanninkhof (1992) parameterization of gas transfer velocity is used and $p\text{CO}_2^{\text{atm}}$ is the National Oceanic and Atmospheric Administration Marine Boundary Layer Reference product (Dlugokencky et al., 2021). The biogeochemical observations used to evaluate and adjust ECCO-Darwin include (a) surface ocean fugacity ($f\text{CO}_2$) from the monthly gridded Surface Ocean CO_2 Atlas (SOCATv5, Bakker et al., 2016), (b) GLODAPv2 ship-based profiles of NO_3 , PO_4 , SiO_2 , O_2 , dissolved inorganic carbon (DIC), and alkalinity (Olsen et al., 2016), and (c) BGC-Argo float profiles of NO_3 and O_2 (Drucker & Riser, 2016; Riser et al., 2018). To adjust the model's fit to the global biogeochemical observations, the Green's function approach is used to adjust biogeochemical initial conditions and model parameters.

OCIMv2021 is an inverse model that assimilates observations of temperature, salinity, CFCs, and radiocarbon to achieve an estimate of the climatological mean ocean circulation (DeVries, 2022). This steady-state circulation model is used together with an abiotic carbon cycle model and atmospheric CO_2 forcing to simulate anthropogenic carbon uptake and its redistribution within the ocean. It uses a monthly time-step and simulates the period 1780 to 2018. No assimilation takes place during this period.

2.2.4. Atmospheric Inversions

Six atmospheric inversions are available for our analysis (Table 2). Atmospheric inversions make use of the worldwide network of atmospheric CO_2 observations. They ingest a data set of fossil fuel emissions, which are assumed to be well known, into an atmospheric transport model and then solve for the spatio-temporal distribution of land and ocean CO_2 fluxes while minimizing the mismatch with atmospheric CO_2 observations (Friedlingstein et al., 2022). Thus, the resulting land and ocean carbon fluxes are bound to the atmospheric CO_2 growth rate, but the estimated regional fluxes depend on the number of stations in the observational network. The inversions also start from prior estimates of land and ocean fluxes. For four inversion data sets that we use here, the ocean prior is taken from $p\text{CO}_2$ -products that are used in this analysis as well (Table 2). One inversion (UoE) uses the Takahashi climatology as a prior and one (CMS-Flux) an ocean biogeochemical model. The atmospheric inversions are thus not independent from the other data classes (Friedlingstein et al., 2022, their Table A4). The atmospheric inversion data were submitted for RECCAP in the same version as in the Global Carbon Budget 2021 (Friedlingstein

et al., 2022), but only since 1990. The three inversions starting later (2001 or 2010) are only included in averages reported for 2015–2018 (Figures 4 and 5), and as individual lines in the time-series figure (Figure 8).

2.3. Processing

Throughout this study, we report the air-sea CO_2 exchange as the net flux (FCO_2), which is the sum of natural, anthropogenic, and river-induced air-sea CO_2 flux (see e.g., Crisp et al., 2022; DeVries et al., 2023; Hauck et al., 2020). As the GOBMs vary widely in their choices on river carbon and nutrient input into the ocean and burial at the seafloor (see DeVries et al., 2023; Terhaar et al., 2023), an adjustment is applied to make all data classes comparable.

2.3.1. River Flux Adjustment

Globally, the majority of GOBMs produce a small imbalance of riverine carbon inflow and burial globally ($<0.14 \text{ PgC yr}^{-1}$), which is smaller than the current best estimate of river-induced CO_2 ocean outgassing of 0.65 PgC yr^{-1} (Regnier et al., 2022). The imbalances are due to manifold choices and illustrate the lack of a closed land-ocean carbon loop in the GOBMs. As the GOBMs do not adequately account for the river discharge and its fate within the ocean, and thus for river-derived ocean CO_2 outgassing (Terhaar et al., 2023), we account for this outgassing by using the spatial patterns of river-induced air-sea CO_2 fluxes from Lacroix et al. (2020) that are scaled to the global value of 0.65 PgC yr^{-1} (Regnier et al., 2022). Southern Ocean outgassing from rivers amounts to 0.04 PgC yr^{-1} , that is, around 6% of the global river flux. It is distributed over the Southern Ocean biomes as follows (positive outgassing): $0.00036 \text{ PgC yr}^{-1}$ in the ICE biome, $0.053 \text{ PgC yr}^{-1}$ (SPSS biome), $-0.014 \text{ PgC yr}^{-1}$ (STSS biome). The estimated riverine CO_2 fluxes were added to biome-integrated fluxes in simulation A for all GOBMs, so that these are comparable to the $p\text{CO}_2$ -products. They are not added to spatial maps of CO_2 fluxes due to large uncertainties in the regional attribution by Lacroix et al. (2020). The riverine fluxes are one (ICE) to multiple (SPSS, STSS) orders of magnitude smaller than the mean fluxes quantified in this study. The uncertainty associated with the river flux adjustment is discussed in Section 4.1.

2.3.2. Treatment of Different Area Coverage

Air-sea CO_2 fluxes in all data classes were integrated over the area available for each GOBM, $p\text{CO}_2$ -product etc., that is, fluxes were not scaled to the same ocean area here. Relative to the ocean area in the RECCAP mask, the covered ocean areas in the GOBMs and data-assimilating models corresponds to 96.2%–100% (minimum for CCSM-WHOI) and to 95.6%–100% in the $p\text{CO}_2$ -products (minimum for JMA-MLR). These differences mainly stem from the ICE biome. We assume that the discrepancy arising from differences in covered area are smaller than the uncertainty arising from any extrapolation to the same area.

2.3.3. Trend Calculation

The reported linear trends between 1985 and 2018, 1985 and 2000 or 2001 and 2018 were obtained from a linear regression of the annual mean time series (using Python's scikit-learn). The slope of the respective fit was multiplied by a factor of 10 to obtain decadal CO_2 flux trends. The start and end year of the trend calculation were chosen based on the RECCAP2 protocol and are supported by the reported stagnation of the Southern Ocean carbon sink in the 1990s and the reinvigoration since the early 2000s (Hauck et al., 2020; Landschützer et al., 2015; Le Quéré et al., 2007).

2.3.4. $p\text{CO}_2$ Decomposition

To separate temperature driven changes in $p\text{CO}_2$ from biological processes and mixing-driven entrainment, $p\text{CO}_2$ is decomposed into thermal and non-thermal components (Takahashi et al., 1993). The thermal component ($p\text{CO}_2^T$) is calculated as

$$p\text{CO}_2^T = \overline{p\text{CO}_2} \cdot e^{(0.0423 \cdot \Delta T)} \quad (2)$$

where $\overline{p\text{CO}_2}$ is the annual mean of $p\text{CO}_2$ and ΔT difference of the monthly mean temperature from the annual mean temperature. The non-thermal contribution ($p\text{CO}_2^{nonT}$) is estimated as the difference of the thermal contribution ($p\text{CO}_2^T$) from the monthly averaged $p\text{CO}_2$. The first derivatives of these two components are subtracted from each other to create the $p\text{CO}_2$ seasonal driver metric, denoted as $\lambda p\text{CO}_2$:

$$\lambda p\text{CO}_2 = \left| \frac{\delta p\text{CO}_2^T}{\delta t} \right| - \left| \frac{\delta p\text{CO}_2^{nonT}}{\delta t} \right| \quad (3)$$

where δt is 1 month. Here, a positive $\lambda p\text{CO}_2$ indicate periods when the thermal component is a larger contributor to $p\text{CO}_2$, and negative values show where the DIC processes (non-thermal) play a dominant role in surface $p\text{CO}_2$ changes. We also denote the first derivatives as $p\text{CO}_2^{T'}$ and $p\text{CO}_2^{nonT'}$ for brevity.

2.3.5. Anthropogenic Carbon Inventories

Anthropogenic CO_2 (C_{ant}) is defined as the change in ocean DIC since preindustrial times due to the direct effect of increasing CO_2 concentration in the atmosphere. It is computed as the DIC difference between experiments A and D. The accumulation of C_{ant} can be separated into a steady-state component (C_{ant}^{ss} , DIC difference between experiments C and B), that is influenced only by the increased atmospheric CO_2 , and a nonsteady state component (C_{ant}^{ns}), which considers the effect of climate variability and change on C_{ant} (and which is maximally 10%–20% of C_{ant} Text S2 and Figures S3 and S4 in Supporting Information S1). Here we focus mainly on the change in C_{ant} that has occurred over the period 1994–2007 (hereafter ΔC_{ant}), to correspond to the years covered by the eMLR(C*) observation-based estimate (Gruber, Clement, et al., 2019). The eMLR(C*) method (Clement & Gruber, 2018) uses ocean measurements of DIC from GLODAP2 (Olsen et al., 2016) over more than 30 years as the foundation to determine ΔC_{ant} between nominal years 1994 and 2007. The method has been shown to be accurate at global and basin scales, but is more uncertain at sub-basin scales and should not be used below 3,000 m depth. The (2 sigma) uncertainty of the eMLR(C*) product is estimated to be around 19% for the Southern Hemisphere (Gruber, Clement, et al., 2019). The eMLR(C*) method differs fundamentally from past indirect or model-based methods used to estimate C_{ant} accumulated since pre-industrial times (DeVries, 2014; Gruber et al., 1996; Sabine et al., 2004; Waugh et al., 2006). Of these, we used the 1800–1994 cumulative C_{ant} estimate based on Sabine et al. (2004), which is characterized by an uncertainty of about 20% globally (Matsumoto & Gruber, 2005; Sabine et al., 2004). In terms of GOBMs, we used all those listed in Table 1, with the exception of FESOM-REcoM-HR and MOM6-Princeton who provided only experiments A and B. For most GOBMs, we analyze C_{ant}^{tot} , to allow for a more accurate comparison with the observation-based data set (eMLR(C*)). However, for MPIOM-HAMOCC and CNRM-ESM2-1 it was only possible to compute C_{ant}^{ss} , because of physical forcing inconsistencies between experiments A and D. We believe that the advantage of including all GOBMs in the analysis outweighs the disadvantages of having an incoherent definition of C_{ant} among GOBMs. It should be noted that the spin-up procedure of ROMS-SouthernOcean-ETHZ, which uses atmospheric CO_2 from 1969 to 1978 (for a 10 year spin-up of the biogeochemical component), makes it suitable only for the analysis of ΔC_{ant} between 1994 and 2007, and not of cumulative C_{ant} until 1994 nor of air-sea C_{ant} fluxes in specific years. As explained in the RECCAP2 model evaluation chapter (Terhaar et al., 2023), all GOBMs are forced with a very similar atmospheric CO_2 mixing ratio ($x\text{CO}_2$) over the historical period. However, the atmospheric $x\text{CO}_2$ in the pre-industrial control simulations across the GOBM ensemble varies between 278 and 287.4 ppm, leading to an underestimate of the C_{ant} storage for those models with a late starting date (Terhaar et al., 2023).

3. Results

3.1. Mean Air-Sea CO_2 Fluxes 1985–2018

We start with a comparison of the average air-sea CO_2 flux in the two data classes (GOBMs, $p\text{CO}_2$ -products) that cover the full period 1985–2018. We exclude data classes with fewer products for the sake of robustness, and show the comparison between all data classes in Sections 3.2 and 3.4. The mean net Southern Ocean air-sea CO_2 flux 1985–2018 by the GOBM ensemble is -0.75 ± 0.28 and $-0.73 \pm 0.07 \text{ PgC yr}^{-1}$ (flux into the ocean) for the $p\text{CO}_2$ -product ensemble mean (Figure 2a). While both ensemble means result in an almost identical ocean uptake of CO_2 , the GOBM ensemble spread is four times larger.

All Southern Ocean regions are sinks of CO_2 based on the ensemble averages of the GOBMs and $p\text{CO}_2$ -products (Figure 2). The subtropical seasonally stratified biome (STSS), which is a subduction area with deep winter mixed layer depth and intermediate chlorophyll concentration (Fay & McKinley, 2014), is the largest sink according to all data sets (GOBMs: $-0.53 \pm -0.17 \text{ PgC yr}^{-1}$, $p\text{CO}_2$ -based products: $-0.62 \pm 0.05 \text{ PgC yr}^{-1}$, Figure 2a). Second is the subpolar seasonally stratified biome (SPSS) (GOBMs: $-0.13 \pm 0.14 \text{ PgC yr}^{-1}$, $p\text{CO}_2$ -products: $-0.06 \pm 0.02 \text{ PgC yr}^{-1}$), which is characterized by upwelling of old water, rich in natural carbon but with low anthropogenic carbon content. The upwelled water is also rich in nutrients, and thus a region with important biological activity. Note that three GOBMs simulate the SPSS to be a source of CO_2 to the atmosphere. The marginal sea ice (ICE) biome is the weakest CO_2 sink (GOBMs: $-0.09 \pm 0.13 \text{ PgC yr}^{-1}$; $p\text{CO}_2$ -products:

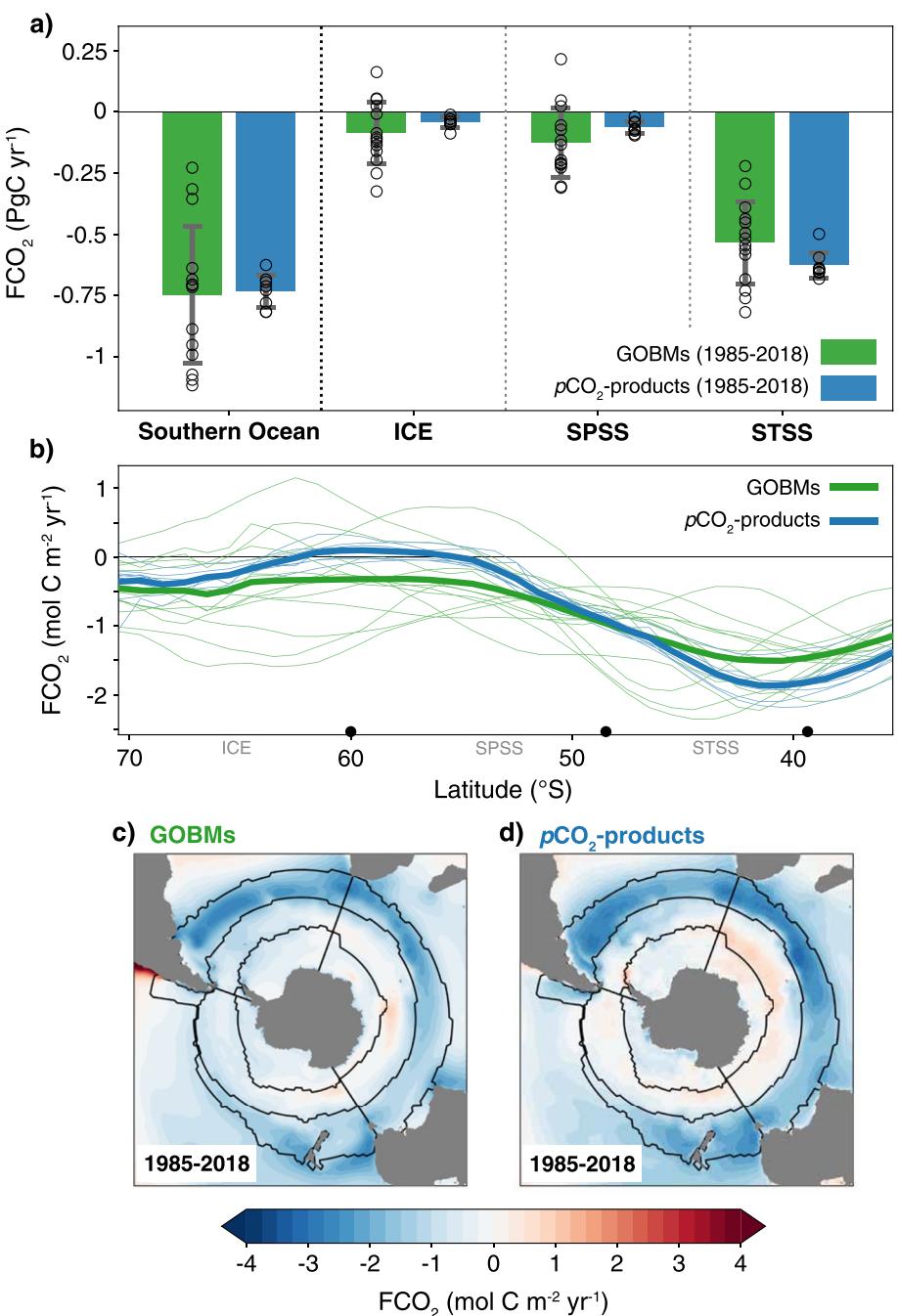


Figure 2. Temporal average of the Southern Ocean CO_2 net flux (FCO_2). A positive flux denotes outgassing from ocean to atmosphere. The temporal average is calculated over the period 1985 to 2018 for the global ocean biogeochemistry models (GOBMs) and $p\text{CO}_2$ -products (Tables 1 and 2). (a) The green and blue bar plots show the ensemble mean of the GOBMs and $p\text{CO}_2$ -based data-products, and open circles indicate the individual GOBMs and $p\text{CO}_2$ -products. The ensemble standard deviation (1σ) is shown by the error bars. The river flux adjustment added to the GOBMs is small (0.04 PgC yr^{-1}), its distribution over the biomes is described in Section 2.3.1. (b) Zonal mean flux density of the different data sets. Thick green and blue lines show the ensemble means, and thin green and blue lines show the individual GOBMs and $p\text{CO}_2$ -products. Approximate boundaries for biomes are marked with black points on the x -axis. (c, d) Maps of spatial distribution of net CO_2 flux for ensemble means of GOBMs, and $p\text{CO}_2$ -products.

$-0.04 \pm 0.02 \text{ PgC yr}^{-1}$) due to sea ice acting as a lid that prevents carbon outgassing in winter, and is the smallest of all three biomes covering an area of about 60% the size of STSS or SPSS (Fay & McKinley, 2014). Four individual models suggest that the ICE biome is a weak outgassing region, but no other data set supports this. Though

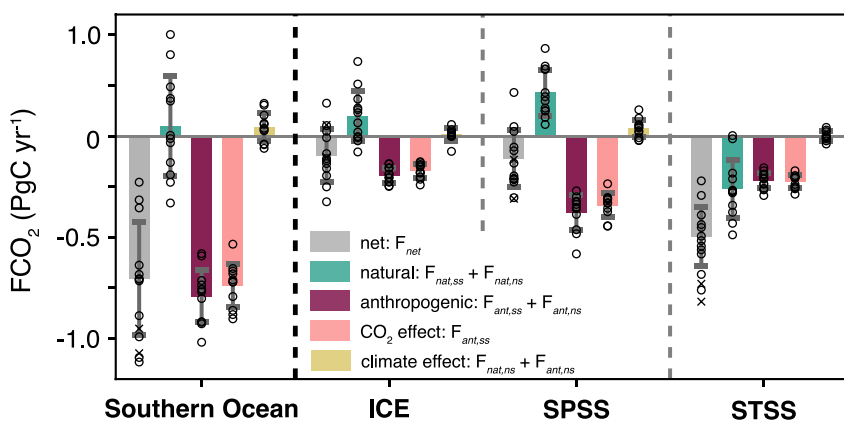


Figure 3. Decomposition of the modeled net air-sea CO_2 flux 1985–2018 into natural and anthropogenic CO_2 fluxes; as well as into CO_2 and climate effects. See method Section 2.2.1 for explanation on this decomposition. The separation into natural and anthropogenic CO_2 fluxes is not possible for FESOM-RECoM-HR and MOM6-Princeton models as only simulations A and B are available. These models are only shown as crosses for net FCO_2 but not used for averaging. Hence, separation within this figure is coherent, but the net FCO_2 is slightly different from the net FCO_2 in Figure 2.

small, the differences between GOBM and $p\text{CO}_2$ -product FCO_2 at the biome-level compensate each other leading to the near-identical estimates for the whole Southern Ocean (Figures 2a and 2b).

In a zonal mean view (Figure 2b), the smallest uptake occurs between 62 and 55°S and the largest uptake around 40°S. However, the amplitude differs between data classes, with the $p\text{CO}_2$ -products having a larger difference between minima and maxima ($1.96 \text{ mol C m}^{-2} \text{ yr}^{-1}$), than the GOBM ensemble mean ($1.19 \text{ mol C m}^{-2} \text{ yr}^{-1}$). Some of the individual GOBMs deviate from this pattern (see Figure S5a in Supporting Information S1 for zonal means of individual models).

Regionally, significant differences emerge between the Atlantic, Indian and Pacific sectors of the Southern Ocean (Figures 2c and 2d). Within the STSS, large CO_2 fluxes into the ocean occur in the Atlantic and Indian sector across all data classes (Figures 2b and 2c, mean flux density: -1.93 and $-2.05 \text{ mol C m}^{-2} \text{ yr}^{-1}$ for GOBMs and $p\text{CO}_2$ -products, respectively, in the Atlantic sector, -1.44 and $-1.89 \text{ mol C m}^{-2} \text{ yr}^{-1}$ in the Indian sector, and -1.22 and $-1.54 \text{ mol C m}^{-2} \text{ yr}^{-1}$ in the Pacific sector). CO_2 outgassing locations differ across the data classes. In the GOBM ensemble mean, the outgassing is mainly confined to the Indian sector of the SPSS, whereas it is more widely spread in the $p\text{CO}_2$ -product ensemble mean covering the Pacific and Indian Ocean sectors of the SPSS and the Indian sector in the ICE biome. The smooth appearance of the outgassing signal in the GOBM and $p\text{CO}_2$ -product ensemble means may be partly attributable to averaging over multiple data sets and months and years.

3.1.1. Decomposition Into Anthropogenic and Natural Carbon Fluxes and Climate Versus Atmospheric CO_2 Effects on the Mean CO_2 Flux

With the aid of the additional model simulations, we can decompose the net Southern Ocean air-sea CO_2 flux into natural and anthropogenic components, and separate the indirect effects of physical climate change and the direct geochemical effect of increasing atmospheric CO_2 mixing ratios. The GOBM ensemble mean indicates that the *natural* Southern Ocean carbon cycle without anthropogenic perturbation would be a small CO_2 source to the atmosphere of 0.05 PgC yr^{-1} , although with a large model spread as indicated by the standard deviation of 0.25 PgC yr^{-1} (Figure 3 green bars). In fact, six GOBMs simulate negative natural CO_2 fluxes, that is, into the ocean, and six GOBMs simulate positive natural fluxes, that is, out of the ocean. This also illustrates that the GOBM spread of net fluxes (gray bars in Figure 3, standard deviation: 0.28 PgC yr^{-1}) is, to the first order, dominated by the model differences of natural fluxes (standard deviation: 0.25 PgC yr^{-1}), which may contain artifacts from model biases and drift (Terhaar et al., 2023). The spread of anthropogenic fluxes is smaller (0.13 PgC yr^{-1} , dark red in Figure 3). The small *natural* outgassing signal in the ensemble mean is a balance of natural CO_2 uptake in the STSS ($-0.26 \pm 0.14 \text{ PgC yr}^{-1}$) and outgassing in the SPSS ($0.21 \pm 0.11 \text{ PgC yr}^{-1}$) and ICE ($0.10 \pm 0.12 \text{ PgC yr}^{-1}$) biomes. This is in qualitative agreement with the patterns of natural CO_2 fluxes by Mikaloff Fletcher et al. (2007) who report outgassing of natural CO_2 in the Southern Ocean with the largest contribution from the subpolar region.

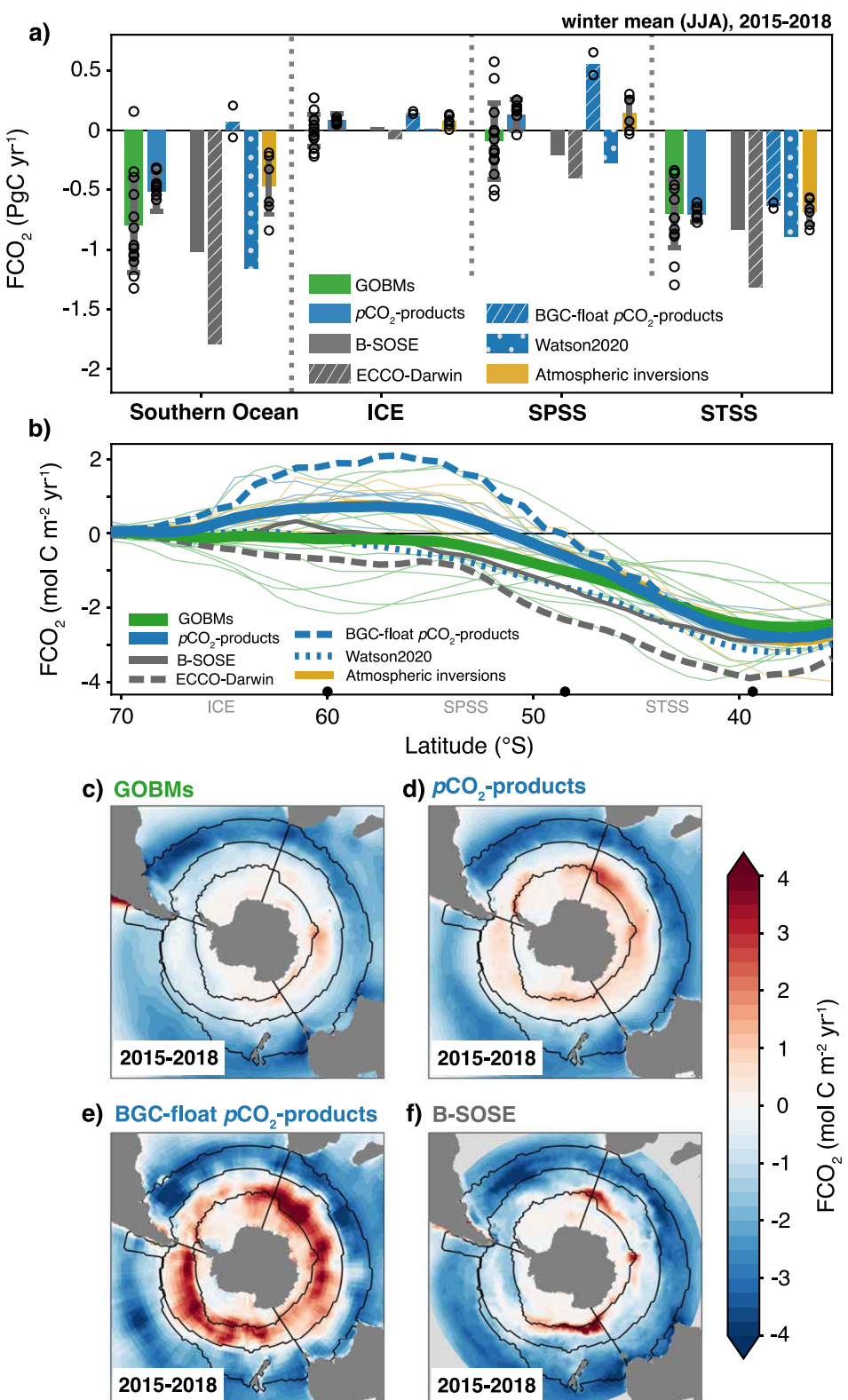


Figure 4. Average winter (June–August) air-sea CO₂ fluxes (FCO₂) in the period 2015–2018, (a) averaged over biomes, (b) zonal mean flux density, and (c–f) maps of flux density. Same as Figure 2, but including also data sets with shorter coverage, and a map of the CO₂ flux from the BGC-float $p\text{CO}_2$ -products (panel (e)), and Biogeochemical Southern Ocean State Estimate (f), and hence focusing on the period 2015–2018 for all data sets for comparability. Note that the MPI model is excluded here. The zonal mean of individual models are presented in Figure S5c in Supporting Information S1.

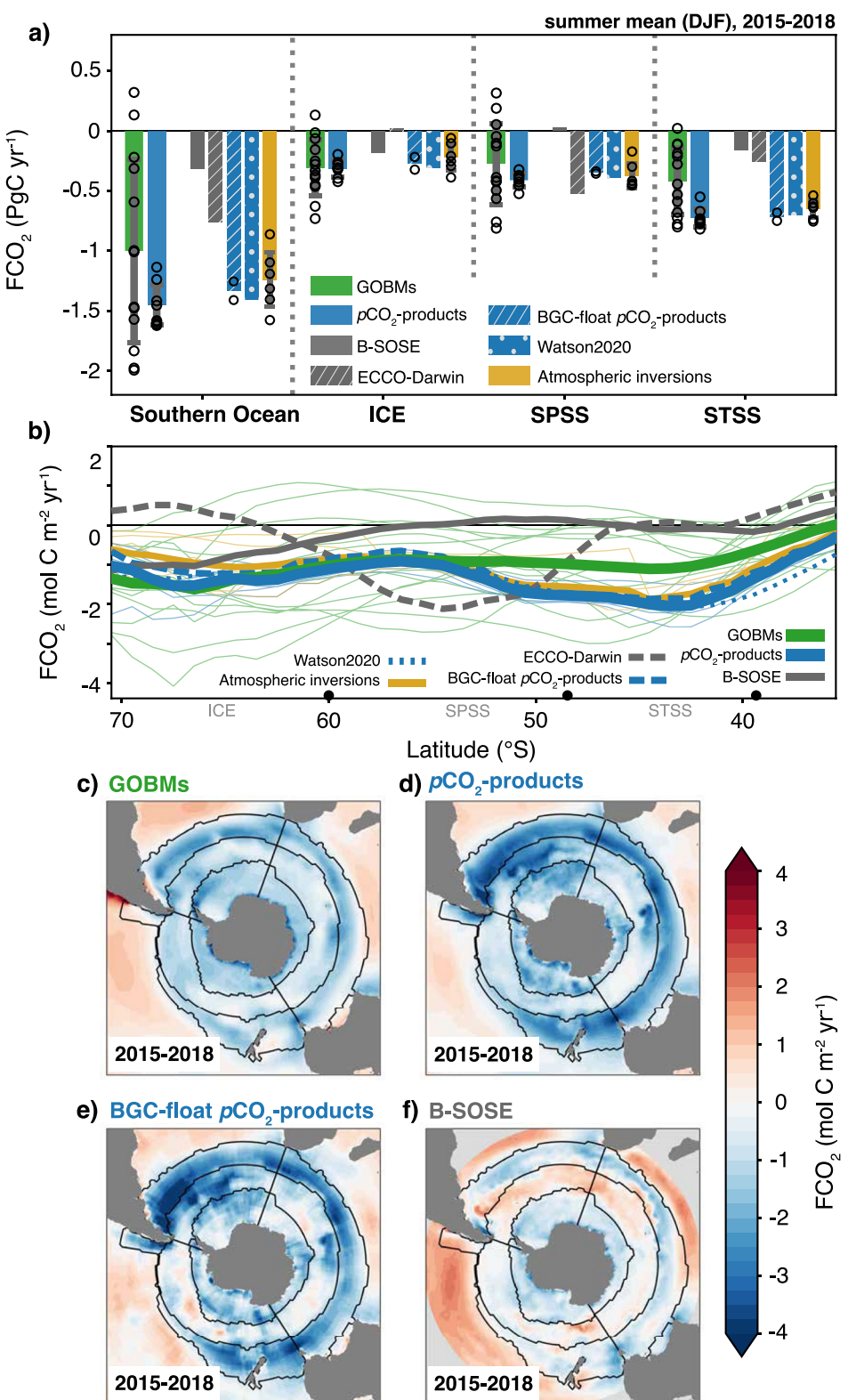


Figure 5. Average summer (December–February) air-sea CO_2 fluxes (FCO_2) in the period 2015–2018. Same as Figure 4, but for summer. The zonal mean of individual models are presented in Figure S5b in Supporting Information S1.

The *anthropogenic* perturbation ($-0.79 \pm 0.13 \text{ PgC yr}^{-1}$, dark red Figure 3) has turned the SPSS and ICE biomes, and possibly the entire Southern Ocean, from source to sink. The large anthropogenic flux contribution in the SPSS ($-0.38 \pm 0.08 \text{ PgC yr}^{-1}$) suppresses the natural CO_2 outgassing flux. The STSS is a sink for both natural and anthropogenic flux components. The *direct effect of increasing atmospheric CO_2* enhances the Southern Ocean sink by $-0.74 \pm 0.11 \text{ PgC yr}^{-1}$ (light red Figure 3) and is the largest signal in the anthropogenic perturbation. A smaller component stems from the climate change effect on this steady state CO_2 -induced flux (Figure S6 in Supporting Information S1). The direct CO_2 effect is largest in the SPSS ($-0.34 \pm 0.06 \text{ PgC yr}^{-1}$) where old water masses reach the surface that are undersaturated in anthropogenic carbon, followed by the STSS and ICE biomes (-0.23 ± 0.03 and $-0.17 \pm 0.03 \text{ PgC yr}^{-1}$). In the upwelling regions, the primary effect of rising atmospheric CO_2 is thus to suppress the outgassing of natural carbon.

The *effect of physical climate change and variability*, that is, warming and changes in wind speed patterns and strength that provoke changes in circulation (Hauck et al., 2013; Le Quéré et al., 2007; Lovenduski et al., 2007), reduces the CO_2 flux into the ocean ($+0.04 \pm 0.07 \text{ PgC yr}^{-1}$, yellow in Figure 3), but is overall small in comparison to the direct CO_2 effect. This climate change induced outgassing stems nearly entirely from the SPSS ($+0.04 \pm 0.04 \text{ PgC yr}^{-1}$), with the largest contribution from the Indian sector followed by the Pacific (Figure S7 in Supporting Information S1). Thus, the climate change effect amplifies the natural CO_2 outgassing, which is also the largest in the Indian and Pacific sectors of the SPSS. The climate effect is a combination of climate effects on natural and anthropogenic CO_2 fluxes, which partly oppose each other (Figure S6 in Supporting Information S1).

3.2. The Seasonal Cycle of Air-Sea CO_2 Fluxes in the Southern Ocean 2015–2018

We now shift our focus to seasonal fluxes by separating fluxes into separate winter (Figure 4) and summer (Figure 5) mean CO_2 fluxes. For this, we examine the period 2015–2018, for which all data sets are available (see Figure S8 in Supporting Information S1 for an annual mean figure for 2015–2018 and Table S4 in Supporting Information S1 for an overview of numbers and comparison to annual means 2015–2018 and 1985–2018). The characteristics of the seasonal cycle and differences between data classes described below are robust to choice of period (2015–2018, 1985–2018).

3.2.1. Winter

In winter, all but two data sets (one GOBM and BGC-float $p\text{CO}_2$ -products) agree that the Southern Ocean is a sink of CO_2 (GOBMs: $-0.83 \pm 0.40 \text{ PgC yr}^{-1}$, $p\text{CO}_2$ products: $-0.51 \pm 0.17 \text{ PgC yr}^{-1}$; Figure 4a, Table S4 in Supporting Information S1). The general pattern of strong uptake toward the north and a reduction toward the south is common to all data classes, though exceptions for individual GOBMs do exist (Figures 4a and 4b). Expounding on this, the strong uptake in the STSS is shown by all data sets, but further south the coherence disintegrates. Within the SPSS, there is considerable variation in position and magnitude of maximum outgassing with some GOBMs being a sink along the entire zonal mean (Figures 4a and 4b). Toward the southern reaches of the ICE biome, fluxes are more coherent as they are constrained by sea-ice cover in winter (Figure 4b). For the zonal means of individual GOBMs, see Figure S5 in Supporting Information S1.

The divergence between data class average flux estimates for the Southern Ocean are explained nearly entirely by differences in the SPSS (GOBMs: $-0.15 \pm 0.32 \text{ PgC yr}^{-1}$ and $p\text{CO}_2$ products: $0.13 \pm 0.13 \text{ PgC yr}^{-1}$, in Figure 4a). Note also that the spread of the individual GOBMs is the largest in the SPSS (0.32 PgC yr^{-1}), although it is also substantial in the other biomes (STSS: 0.29 PgC yr^{-1} , ICE: 0.13 PgC yr^{-1}) (Figure 5a). The SPSS is also where we see the largest impact of the inclusion of floats in the BGC-float $p\text{CO}_2$ -products (Figures 4d and 4e), with the mean outgassing flux more than doubling that of the regular $p\text{CO}_2$ -product ensemble. Interestingly, differences between B-SOSE and BGC-float $p\text{CO}_2$ -products are large ($\sim 1 \text{ PgC yr}^{-1}$, whole Southern Ocean) and FCO_2 from these data sets even have a different sign for whole Southern Ocean and SPSS biome (Figure 4) although they both include BGC float data.

The zonal differences and features of fluxes between data classes are also most distinct in the SPSS (Figures 4c–4f). In short, the Atlantic sector of the SPSS has the lowest flux (weak source or even sink), while the Indian and Pacific sectors dominate the outgassing. The data-assimilated model B-SOSE has stronger localized outgassing compared with the other data classes but bear in mind that B-SOSE is only one data sets (Figure 4f), while the other data classes (Figures 4c–4e) represent up to 13, thus potentially averaging out local signals. The outgassing hotspot at the boundary between the Atlantic and Indian sectors of the SPSS can also be recognized in the

$p\text{CO}_2$ -products (Figure 4d). The second hotspot in the western Pacific SPSS is not distinguishable in the other data sets.

3.2.2. Summer

In summer, GOBMs, $p\text{CO}_2$ -products and inversions largely show CO_2 uptake within the three Southern Ocean biomes, and outgassing north of the STSS (Figures 5a and 5b, Table S4 in Supporting Information S1). In contrast to winter, the GOBM ensemble mean for summer 2015–2018 ($-1.04 \pm 0.77 \text{ PgC yr}^{-1}$) underestimates the CO_2 uptake relative to the $p\text{CO}_2$ -product ensemble mean ($-1.45 \pm 0.17 \text{ PgC yr}^{-1}$, Figure 5a). This also holds true for the data-assimilated models, where B-SOSE even simulates outgassing in the SPSS (Figures 5a, 5b, and 5f). Otherwise, the data-assimilated models, B-SOSE and ECCO-Darwin, deviate substantially from the other data classes. The differences between $p\text{CO}_2$ -products with and without BGC-float data are hardly apparent in summer (Figure 5a, compared to Figure 4a). This could be due to a smaller discrepancy between float and ship-data in summer, and/or a dominance of SOCAT data in summer for the ship + float estimate. For context, for the period 2015 through 2018, BGC-float data account for up to 70% of winter $p\text{CO}_2$ monthly by $1^\circ \times 1^\circ$ measurements in the Southern Ocean (SOCAT + floats), while in summer the floats represent only 20% (Bakker et al., 2016; Bushinsky et al., 2019).

While the STSS was a region of coherence between data classes in winter (Figure 4), it is the main source of the discrepancy between the GOBM and $p\text{CO}_2$ -product ensemble means in summer (GOBMs: $-0.40 \pm 0.28 \text{ PgC yr}^{-1}$, $p\text{CO}_2$ -products: $-0.73 \pm 0.07 \text{ PgC yr}^{-1}$). The discrepancy is comparatively smaller in the SPSS (GOBMs: $-0.33 \pm 0.34 \text{ PgC yr}^{-1}$, $p\text{CO}_2$ -products: $-0.41 \pm 0.06 \text{ PgC yr}^{-1}$). We note that CO_2 fluxes for both GOBMs and $p\text{CO}_2$ -products show less variation from ICE to STSS in summer compared to winter (Figure 4b vs. Figure 5b, respectively). There is, nevertheless, an offset with lower GOBM CO_2 uptake than in $p\text{CO}_2$ -products north of 55°S , and vice versa to the south. Also, the GOBM spread in the represented magnitude of the fluxes is large. In absolute terms, the GOBM ensemble spread of fluxes in summer (from -2.03 to $+0.28 \text{ PgC yr}^{-1}$) is larger than in winter (from -1.36 to 0.12 PgC yr^{-1}) or than the spread in the annual mean (from -1.30 to $-0.38 \text{ PgC yr}^{-1}$; see Figure S5b in Supporting Information S1 for zonal means of individual GOBMs). This mirrors the difficulty in representing the balance between physical and biological processes in summer, which is further assessed in the next two Sections 3.2.3 and 3.2.4.

3.2.3. The Full Seasonal Cycle

We diagnose distinctly different seasonal cycles in the three biomes. The ICE biome has a rather clear maximum uptake in summer in the GOBM and $p\text{CO}_2$ -product ensemble means, as well as most individual data sets (Figure 6a). In the STSS, the $p\text{CO}_2$ -products suggest a weak seasonal cycle with a maximum uptake in autumn (Figure 6c), while the majority of GOBMs simulate a maximum CO_2 uptake in winter and a substantially smaller flux in summer.

The largest disagreement occurs in the SPSS, where the seasonal cycle transitions from winter outgassing in the ICE biome to summer outgassing in the STSS biomes. Here, in the SPSS, atmospheric inversions and $p\text{CO}_2$ -products (including the BGC-float $p\text{CO}_2$ -products), suggest the maximum CO_2 uptake to be in summer. In winter, the BGC-float $p\text{CO}_2$ -products more than double the estimates of outgassing relative to the other $p\text{CO}_2$ -products (Figure 6b). The GOBM ensemble average roughly agrees with this seasonal pattern, but simulates a reduced seasonal cycle amplitude (Figure 6b). The reduced amplitude in the SPSS is also due to different seasonal cycle phasing within the GOBM ensemble, with 8 out of 13 GOBMs simulate the maximum uptake between November and January (Figures 6b and 6d–6r), illustrating the complexity of representing the transition between the different seasonal cycle regimes. As already seen in Figures 4 and 5, the seasonal cycle differs substantially between B-SOSE and BGC-float $p\text{CO}_2$ -products, particularly in the SPSS despite the new information provided by the BGC-floats. Further, the two data-assimilating models differ by a similar amount as other GOBMs differ from each other, suggesting that the model dynamics dominate over assimilated data.

In summary, most GOBMs and $p\text{CO}_2$ -products agree on a summer peak in the ICE biome (but exceptions exist, Figures 6d–6r), and a winter peak at the northern boundary of the Southern Ocean. The largest discrepancy between data sets is where and how swift this transition occurs. While the use of static biomes adds to the discrepancies seen in the averaged seasonal cycles (Figures 6a–6c), the disagreement between the phasing of individual GOBMs is likely a much larger contributor to these discrepancies (Figures 6d–6p). We now turn to an investigation of the thermal and non-thermal effects on the seasonal cycle, which may help explain these discrepancies.

3.2.4. Thermal Versus Non-Thermal Effects on the Seasonal Cycle

The seasonal cycle of CO_2 fluxes in the Southern Ocean is a balancing act between competing thermal and non-thermal drivers (Mongwe et al., 2016, 2018; Prend et al., 2022). DIC draw-down by biological production leads to a summer minimum in $p\text{CO}_2$ and maximum in CO_2 uptake (Figures 7a–7c, Metzl et al., 2006; Mongwe et al., 2018). Whereas in autumn and winter, upwelling and entrainment of DIC-rich water into the mixed layer leads to a maximum in $p\text{CO}_2$ and a minimum in CO_2 uptake or even outgassing. Seasonal variations in mixed layer temperature further affect the solubility of CO_2 , with lower (higher) temperatures increasing (decreasing) solubility and thus promoting CO_2 uptake (outgassing) (Takahashi et al., 2002).

The thermal and non-thermal components of $p\text{CO}_2$ can be decomposed to determine the dominant driver on monthly timescales (Figure 7; Mongwe et al., 2018). Here, we do this by estimating the absolute difference of the rate of change of the thermal ($p\text{CO}_2^{T'}$) and non-thermal ($p\text{CO}_2^{nonT'}$) components (Figure 7; Equation 3). The contribution of salinity and total alkalinity to seasonal $p\text{CO}_2$ changes are small in the Southern Ocean and compensate for each other on a seasonal scale (e.g., Lauderdale et al., 2016; Sarmiento & Gruber, 2006), thus we here consider $p\text{CO}_2^{nonT'}$ to be predominantly DIC-driven.

In general, the seasonal cycle phasing of the thermal component of the GOBMs agrees well with those of the $p\text{CO}_2$ -products (Figures 7d–7f). This should not come as a surprise, as GOBMs are forced by atmospheric reanalyses which assimilate observed SST (Doney et al., 2007). As a result, $p\text{CO}_2^{T'}$ of the $p\text{CO}_2$ seasonal cycle in the GOBMs (forced by reanalyses) compare much better to $p\text{CO}_2^{T'}$ derived from the $p\text{CO}_2$ -products than fully coupled Earth System Models (Mongwe et al., 2016, 2018). The non-thermal contribution is thus the primary reason for the spread between GOBMs, and for the differences between GOBMs and $p\text{CO}_2$ -products (Figures 7d–7f). Thus, we group GOBMs based on whether they are predominantly DIC or thermally driven across all three biomes (Figures 7g–7i, Table S2 in Supporting Information S1), which we term DIC-dominant or DIC-weak respectively.

In DIC-weak GOBMs, the strong underestimation of $p\text{CO}_2^{nonT'}$ causes these models to be too strongly temperature driven across the year (Figure 7). This reverses the seasonal cycle of $p\text{CO}_2$ (Figure 7c) and shifts the timing of uptake toward the colder months (when CO_2 solubility is largest). While in spring and summer, the role of biologically driven uptake is suppressed in favor of warming driven outgassing. This effect is largely confined to the STSS and to a lesser extent also the SPSS, and can account for the mismatch in the seasonal cycle of $p\text{CO}_2$ and CO_2 flux seen in some GOBMs (Figures 7b and 7c and Figures 6b and 6c). For example, in the STSS, nearly all GOBMs and specifically all DIC-weak GOBMs have a shifted season of maximum uptake from summer to winter/spring, that is, toward the colder months (Figures 7c and 7f and Table S2 in Supporting Information S1). In terms of the underlying mechanisms driving the underestimated $p\text{CO}_2^{nonT'}$, we hypothesize that a lack of deep vertical mixing in winter leads to too little entrainment of DIC-rich deep waters, while simultaneously allowing for too early primary production (which may then shift the growing season earlier and reduce biologically driven summer uptake). Notably, the bias in $p\text{CO}_2$ is largest in summer (DJF), followed by autumn (MAM), and is about twice as large in the DIC-weak GOBMs than in the DIC-dominant GOBMs (Figure S13 in Supporting Information S1). This further supports the lesser importance of thermal processes in the STSS and SPSS regions evident in the $p\text{CO}_2$ -products.

In the ICE biome, fluxes of the GOBMs and $p\text{CO}_2$ -products tend to agree much more closely in terms of their representation of the seasonal cycle (Figure 6a). This is likely related to the strong role the seasonal advance and retreat of sea ice plays in air-sea CO_2 fluxes, primarily through its effect as a physical barrier. The large difference in the seasonal cycle of $p\text{CO}_2$ (Figure 7a) between the GOBMs and $p\text{CO}_2$ -products thus has little impact on the fluxes (Figure 6a). Further, sea ice can also have an effect on vertical mixing and light availability, thus impacting both physical and biological pathways of DIC into and out of the mixed layer (Bakker et al., 2008; Shadwick et al., 2021; M. Yang et al., 2021).

3.3. Mean Air-Sea CO_2 Flux of All Data Classes

We next inspect the mean fluxes for data sets that are not available for the full time-period in an annually resolved perspective (Figure 8) in this section and the temporal evolution of the air-sea CO_2 fluxes from 1985 to 2018 in the next Section 3.4.

Acknowledging some agreement between GOBMs and $p\text{CO}_2$ -based product ensemble means despite large spread across GOBMs (Figure 8 bars), substantial deviations among individual data sets appear. B-SOSE (2015–2018)

suggests a 0.25 PgC yr^{-1} smaller uptake than the GOBM and $p\text{CO}_2$ -product ensemble means for the entire Southern Ocean (Figure 8a). ECCO-Darwin has the largest flux estimate into the ocean in the SPSS and the entire Southern Ocean (1.30 PgC yr^{-1} , 1985–2018). Notably, the two data-assimilated models B-SOSE and ECCO-Darwin differ by a factor of 2 for the Southern Ocean wide estimate. In agreement with previous reports (Bushinsky et al., 2019), BGC-float $p\text{CO}_2$ -products suggest Southern Ocean uptake to be 40% (0.4 PgC yr^{-1}) smaller than the $p\text{CO}_2$ -products without BGC-float data (2015–2018). This discrepancy originates largely in the SPSS, where the BGC-float $p\text{CO}_2$ -products estimate outgassing of 0.14 PgC yr^{-1} , and the ensemble mean of the SOCAT-only-based $p\text{CO}_2$ -products estimate a CO_2 uptake of $-0.13 \text{ PgC yr}^{-1}$.

Smaller contributions to the deviation stem from the STSS and ICE biomes where BGC-float $p\text{CO}_2$ -products report a smaller uptake by 0.14 PgC yr^{-1} when compared with the regular $p\text{CO}_2$ -products. The Watson2020-product is generally close to the other $p\text{CO}_2$ -products, with the exception of the SPSS where it suggests a flux of $-0.18 \text{ PgC yr}^{-1}$ (1985–2018), which is larger than any other $p\text{CO}_2$ -product. The origin of the large SPSS difference in Watson2020 could, in part, be attributed to subtle differences in method choices in addition to different flux parameterizations (Watson et al., 2020). The atmospheric inversions produce a somewhat lower sink ($-0.64 \text{ PgC yr}^{-1}$, average over three inversions 1985–2018), but are generally close to the $p\text{CO}_2$ -products, as they mostly use surface $p\text{CO}_2$ -products as a prior (Table 2 and Friedlingstein et al., 2022).

3.4. Temporal Variability and Trends in Air-Sea CO_2 Flux 1985–2018

While the STSS was a net-sink region throughout the period (Figure 8), the SPSS and ICE have turned from neutral (around 0 PgC yr^{-1}) to net sink regions since 1985, based on GOBM and $p\text{CO}_2$ -product ensemble mean estimates. In the case of the $p\text{CO}_2$ -products, the trends should be interpreted in the context of the sparse observations, particularly prior to the 2000s (Figures 9a and 10c). However, most individual GOBMs support the shift from neutral to uptake, with only two GOBMs (CCSM-WHOI and EC-Earth3) simulating either the ICE or SPSS biomes as regions of outgassing after 2015.

The temporal variability is quantified as the amplitude of “interannual variability” (IAV). This is calculated as the standard deviation of the detrended time-series, as defined in Rödenbeck et al. (2015) and Friedlingstein et al. (2022), which, in reality, captures both interannual and decadal variability components. Following this definition, the $p\text{CO}_2$ -products have a larger interannual variability for the Southern Ocean wide integrated flux (0.09 PgC yr^{-1} , range 0.04 – 0.16 PgC yr^{-1}) compared to the GOBMs (0.06 PgC yr^{-1} , range 0.03 – 0.10 PgC yr^{-1} , Table S3 in Supporting Information S1). Notably, the MPI-SOM-FFN $p\text{CO}_2$ -product, which formed the basis of previous reports on Southern Ocean decadal variability (Landschützer et al., 2015), has the largest IAV of 0.16 PgC yr^{-1} , about 60% larger than the next largest $p\text{CO}_2$ -product IAV. This is in line with previous studies that found that the MPI-SOM-FFN approach may overestimate Southern Ocean variability by 30% (Gloegel et al., 2021) and the decadal trend 2000–2018 by 130% (Hauck et al., 2023). The amplitude of interannual variability in the atmospheric inversion ensemble mean can only be calculated for the period since 1990 based on three ensemble members. The resulting IAV is higher than in any other data class (0.15 PgC yr^{-1} , range 0.1 – 0.2 PgC yr^{-1}), which appears to be variability on multi-year to decadal scale (Figure 8), but is probably less robust due to the small ensemble size and different period.

Within the Southern Ocean, the strongest IAV is found in the SPSS region (0.04 PgC yr^{-1} GOBMs, 0.05 PgC yr^{-1} $p\text{CO}_2$ -products, 0.08 PgC yr^{-1} atm. inversions), followed by the STSS (0.02 PgC yr^{-1} GOBMs, 0.03 PgC yr^{-1} $p\text{CO}_2$ -products, 0.06 PgC yr^{-1} atm. inversions) and ICE biome (0.02 PgC yr^{-1} for GOBMs and $p\text{CO}_2$ -products, 0.03 PgC yr^{-1} atm. inversions). Within the subpolar biome, the Indo-Pacific sector has a higher IAV (0.02 PgC yr^{-1} GOBMs and $p\text{CO}_2$ -products, 0.04 – 0.05 PgC yr^{-1} atm. inversions) than the Atlantic sector (0.01 PgC yr^{-1} GOBMs, 0.02 PgC yr^{-1} $p\text{CO}_2$ -products and atm. inversions). The large contribution to interannual variability in the SPSS may well be linked to the largest amplitude of the seasonal cycle of CO_2 flux (see Section 3.2.3).

To assess the decadal-scale trends, we fit linear trends to the periods 1985–2000 and 2001–2018 (Section 2.3.3, Figures 8e–8h). This choice is motivated by the fact that the year 2000 marks roughly the mid of the considered time period and the inflection point in global and Southern Ocean CO_2 uptake (Gruber et al., 2023; Landschützer et al., 2015, 2016; Le Quéré et al., 2007). We acknowledge that trend calculations are sensitive to choice of start and end years (Easterling & Wehner, 2009; Fay & McKinley, 2013), but the general statements on the two periods hold also when start and end years are varied (Table S5 in Supporting Information S1). The $p\text{CO}_2$ -products suggest a stagnation of the flux in the STSS, and even a flux decrease in the SPSS prior to 2000. In contrast,

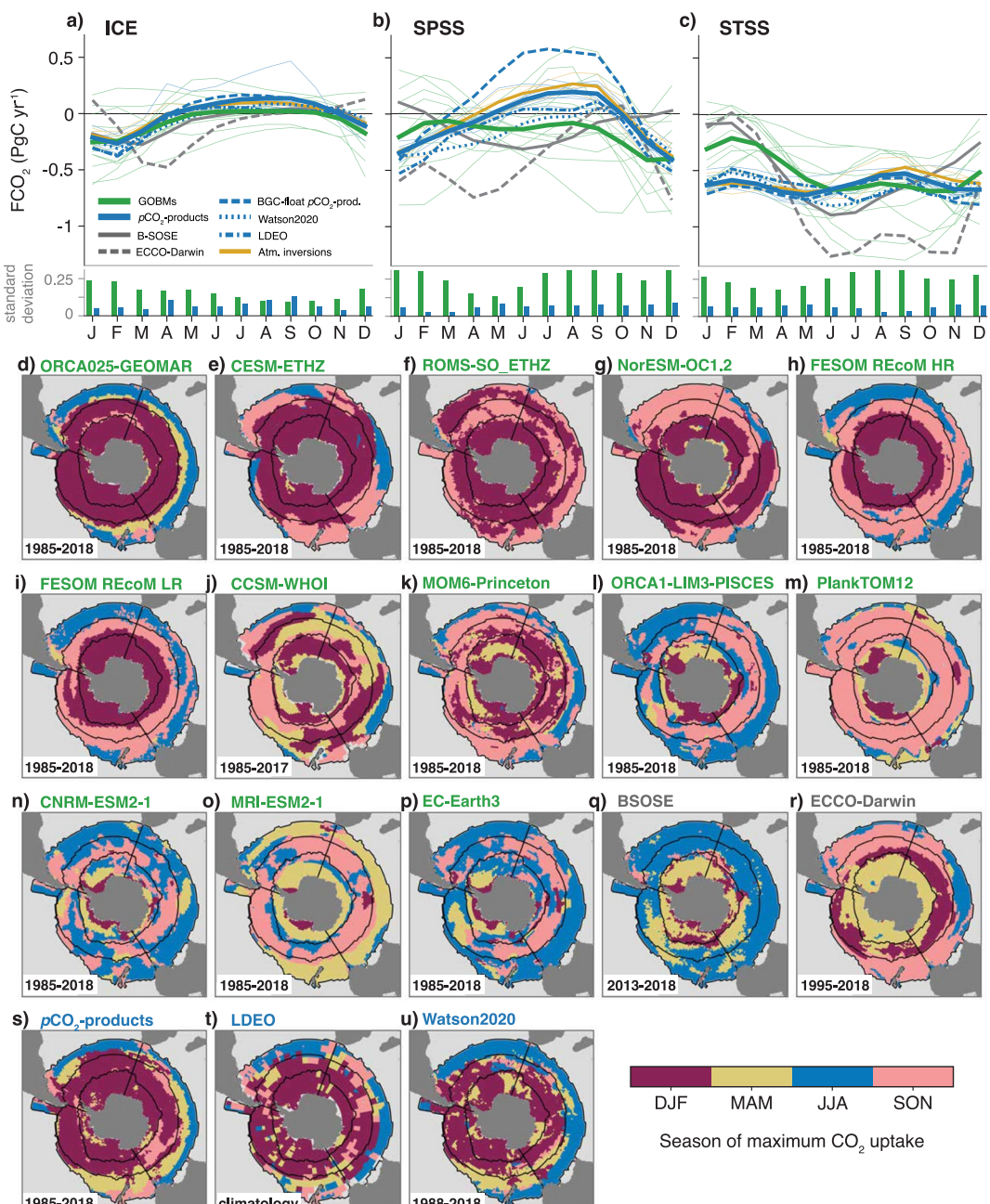


Figure 6. The seasonal cycle of air-sea CO_2 flux in the Southern Ocean separated by biomes for all data sets as indicated in the legend, (a) subtropical seasonally stratified biome, (b) subpolar seasonally stratified biome, and (c) ice biome. Thin green and blue lines depict individual global ocean biogeochemistry models (GOBMs) and $p\text{CO}_2$ -products, and thick lines indicate their ensemble means. Note that the MPI model is excluded here. The ensemble standard deviation (1σ) is shown by the bars for each month. Panels (d–u) present the season of maximum CO_2 uptake per grid cell in the individual GOBMs, data-assimilated models and the ensemble mean of the $p\text{CO}_2$ -products over the period indicated in the panels (varies by data set). See Figure S9 in Supporting Information S1 for the individual $p\text{CO}_2$ -products (panel (d–u) equivalents) and Figure S10 in Supporting Information S1 for the seasonal cycle in all nine subregions (equivalent to panels (a–c) but further split into Atlantic, Pacific, and Indian Ocean sectors).

GOBMs suggest a continued increase in the sink in the STSS and SPSS in the same period. In the ICE biome, GOBMs and $p\text{CO}_2$ -products result in an increasing trend (Figure 8h). After 2000, $p\text{CO}_2$ -products and GOBMs agree on a trend toward more CO_2 uptake, which is significantly different from zero in all biomes except for $p\text{CO}_2$ -products in the ICE biome (see numbers in Figures 8e–8h). However, they differ substantially in magnitude

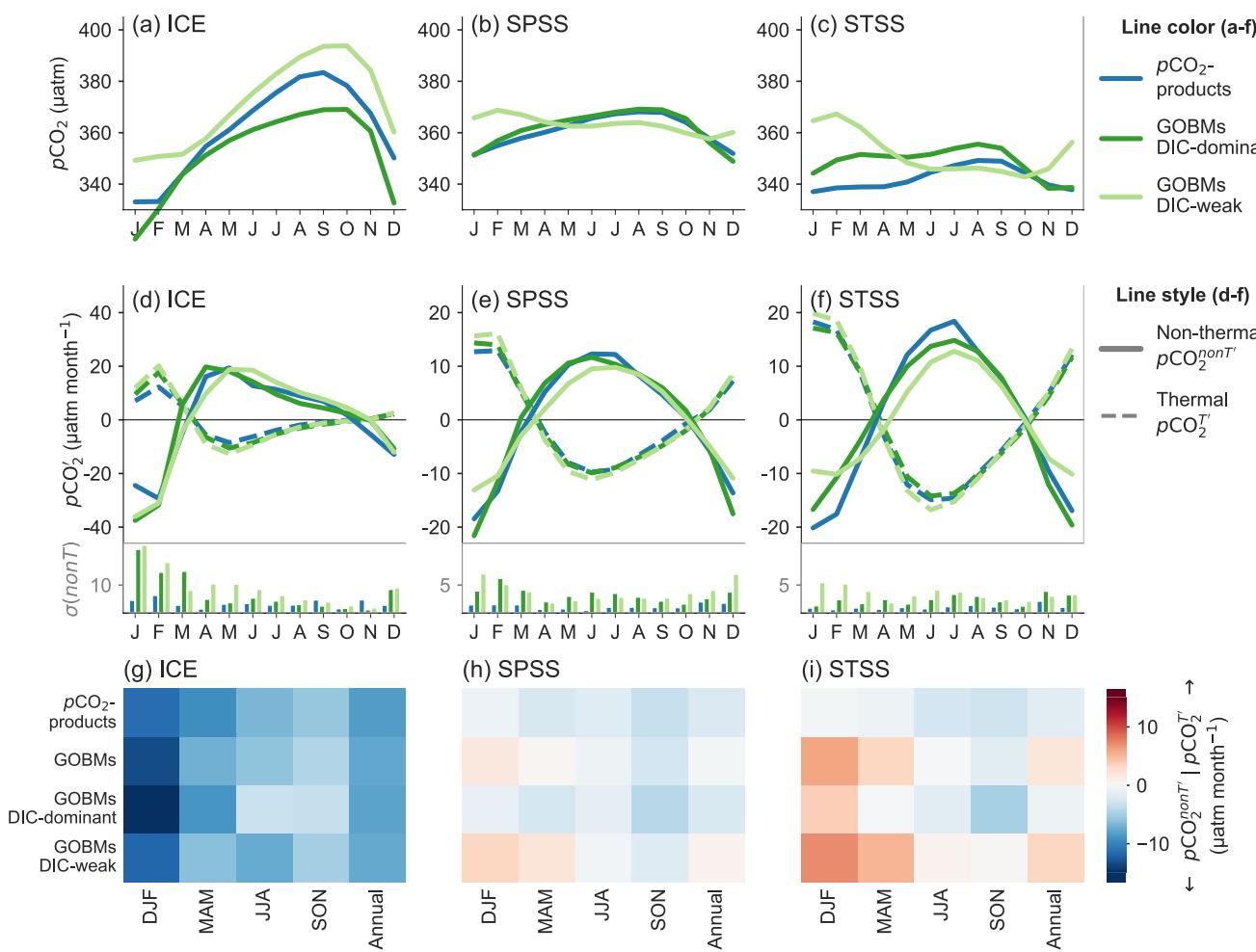


Figure 7. (a–c): The climatological seasonal cycle of $p\text{CO}_2$ on a monthly scale. (d–f): Seasonal cycle of the rate of change of the thermal ($p\text{CO}_2^{T'}$, dashed lines) and non-thermal ($p\text{CO}_2^{nonT'}$, solid lines) components of ocean surface $p\text{CO}_2$ on monthly time scales given in $\mu\text{atm month}^{-1}$ (Equation 2). The bars on the bottom show standard deviations of the non-thermal component. Models have been grouped into DIC-dominant/weak, where the DIC-weak models have a thermal contribution >0 for the mean of the subtropical seasonally stratified and subpolar seasonally stratified (shown in panel (g–i); see Figure S11 in Supporting Information S1 for individual global and regional ocean biogeochemistry models, and Table S2 in Supporting Information S1 for the DIC-dominant/weak model groups). (g–i): $\lambda p\text{CO}_2$, the difference of the thermal and non-thermal (dissolved inorganic carbon [DIC]) components of ocean surface $p\text{CO}_2$ as in Mongwe et al. (2018). When $\lambda p\text{CO}_2 > 0$ (red) indicates temperature dominance, and $\lambda p\text{CO}_2 < 0$ (blue) indicates that the non-thermal component (i.e., DIC) is dominant. The MPI model is excluded in this analysis.

between GOBM and $p\text{CO}_2$ -product ensemble means, particularly in the STSS (Figure 8f). The discrepancies in the magnitude of the trend act to decrease the gap between GOBM and $p\text{CO}_2$ -product ensemble means in the SPSS and ICE biomes, but lead to the divergence in the flux estimate in the STSS.

On a sub-biome level (i.e., Atlantic, Indian, and Pacific sectors), all three sectors in the STSS were CO_2 sinks throughout the period and had weaker trends (less negative) before 2000 compared to the period after 2000 (Figure S12 in Supporting Information S1). In the SPSS, the Indian and Pacific sectors are characterized by intermittent outgassing and uptake patterns, in line with observations from BGC-floats (Prend et al., 2022). In the SPSS, only the Atlantic sector has a net uptake throughout the period, and the Indian Ocean sector shows the largest model spread of all three sectors (as in the STSS). In the ICE biome, a consistent quasi-linear evolution is apparent in all sectors. We further analyze divergence and drivers of trends in Section 3.4.2.

3.4.1. Comparison With In Situ $p\text{CO}_2$

Here, we evaluate the accuracy of $p\text{CO}_2$ across data classes since $p\text{CO}_2$ is the dominant driver of air-sea CO_2 flux variability at a monthly scale (Landschützer et al., 2016). All data sets are compared with observations (monthly gridded SOCAT v2022 data set Bakker et al., 2016, 2022; Sabine et al., 2013). The RECCAP2 data sets are

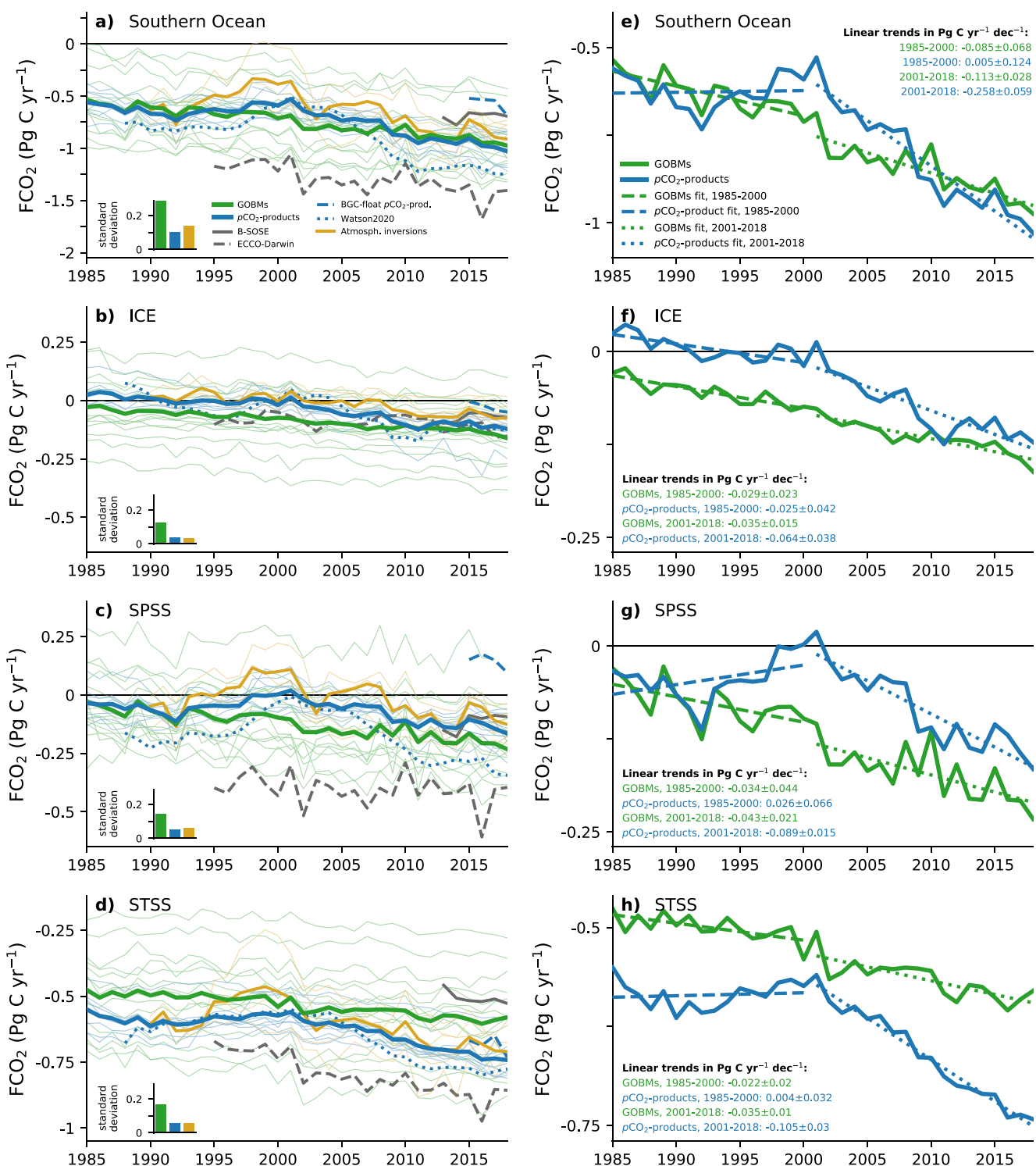


Figure 8. Temporal evolution of the Southern Ocean air-sea CO₂ flux for (a) the entire Southern Ocean, the (b) subtropical seasonally stratified, (c) subpolar seasonally stratified, and (d) ice biomes. The ensemble standard deviation (1 σ) averaged over the whole time series, is shown by the bars. Panels (e-h) are the same as panels (a-d) for the global ocean biogeochemistry model (GOBM) ensemble average and pCO₂-product ensemble average only, with linear trends between 1985–2000 and 2001–2018 as the dashed and dotted lines, respectively. The uncertainty range of the trend is calculated as one standard deviation of the trends across all GOBMs and pCO₂-products, respectively. Note the different y-axis scales. The separation into Atlantic, Pacific, and Indian Ocean sectors is shown in Figure S12 in Supporting Information S1.

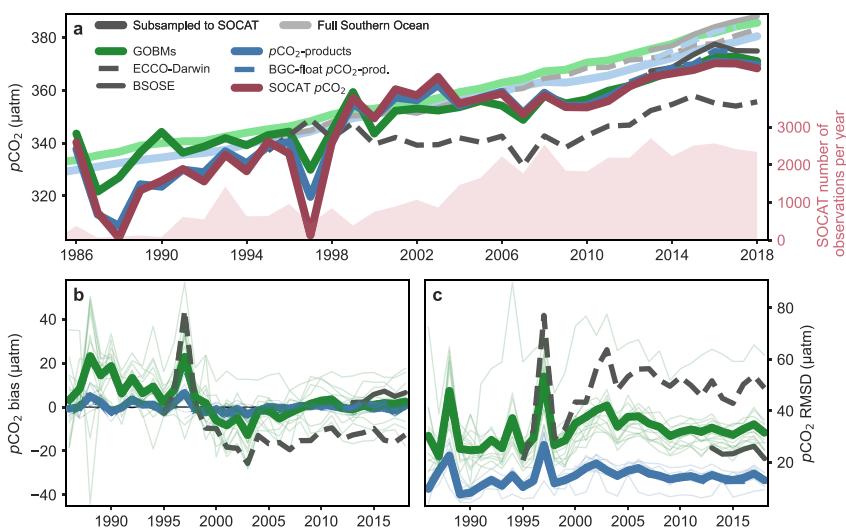


Figure 9. Comparison of surface mean $p\text{CO}_2$ for the whole Southern Ocean between global ocean biogeochemistry models (GOBMs) and $p\text{CO}_2$ -products with in situ observations (gridded SOCAT v2022 data set Sabine et al., 2013). (a) Time-series of annually averaged $p\text{CO}_2$ from GOBMs (green), data-assimilated models (grays), and $p\text{CO}_2$ -products (blue). The darker shaded lines show the annual mean as calculated from the data sets subsampled to match the historic SOCAT sampling. The lighter shades show the annual mean calculated for the full coverage. The dark red line depicts the annual mean $p\text{CO}_2$ from SOCAT observations without interpolation. The assimilation products (ECCO-Darwin and Biogeochemical Southern Ocean State Estimate) are kept separate as they have different time series lengths (shown by dashed and solid gray lines, respectively). The light red area plot (right y-axis) shows the number of monthly by $1^\circ \times 1^\circ$ gridded SOCAT observations per year. (b) The bias of $p\text{CO}_2$ for all data classes (subsampled to match SOCAT observations, dark lines in panel (a)) relative to SOCAT $p\text{CO}_2$ observations (solid dark red line in panel (a)). (c) The root mean squared difference (RMSD) between SOCAT observations and estimates for all data classes. Bias and RMSD were calculated on a monthly by $1^\circ \times 1^\circ$ resolution, and the bias and RMSD were averaged to annual means afterward. A plot of RMSE and bias for subpolar seasonally stratified and subtropical seasonally stratified biomes and different seasons is presented in Figure S13 in Supporting Information S1.

subsampled to match the SOCAT observations in time and space, meaning that we do not assess sampling biases, but rather the mismatch between the observed and estimated $p\text{CO}_2$.

The comparison of the RECCAP2 GOBMs and $p\text{CO}_2$ -products with gridded in situ $p\text{CO}_2$ from SOCAT v2022 shows relatively good agreement (Figure 9a). The SOCAT $p\text{CO}_2$ data shows large interannual variability due to spatially and temporally varying sampling efforts from year to year, particularly prior to 2000 when samples are fewer and thus carry more weight (Figure 9a). For example, in 1997, SOCAT $p\text{CO}_2$ is anomalously low due to high sampling density in the Ross Sea during summer when primary production drives intense CO_2 drawdown (Arrigo & van Dijken, 2007). The $p\text{CO}_2$ products have a lower bias and a narrower spread than the GOBMs prior to 2000 (1.7 ± 4.3 and 10.7 ± 8.0 μatm, respectively), with the bias and the spread decreasing after 2000 for both classes (-0.3 ± 2.6 and -0.9 ± 3.9 μatm, Figure 9b). This comparison of simulated to observed $p\text{CO}_2$ at observation sites demonstrates that GOBMs are capable of reproducing SOCAT $p\text{CO}_2$ and its temporal evolution on large spatial and annual time-scales. Thus, for the period after 2000, the differences in CO_2 flux trend for the entire Southern Ocean between GOBMs and $p\text{CO}_2$ -products (Figure 8) cannot be attributed to differences in $p\text{CO}_2$ in the regions where observations were taken. Instead, the differences arise primarily from areas where no $p\text{CO}_2$ observations exist, as also concluded in Hauck et al. (2020). The $p\text{CO}_2$ time-series calculated from the full coverage results in a lower $p\text{CO}_2$ value in the $p\text{CO}_2$ -products than in the GOBMs (Figure 9a), which could explain the stronger CO_2 flux trend in the $p\text{CO}_2$ -products (Figure 8). This discrepancy between $p\text{CO}_2$ -products and GOBMs is larger in the last 10 years (2009–2019: 5.8 μatm) than the previous decade (1999–2008: 2.8 μatm, Figure 9a). Nevertheless, the root mean squared difference calculated from monthly mean data is higher in GOBMs than in $p\text{CO}_2$ -products (Figure 9c). This is expected as the $p\text{CO}_2$ -products are trained to fit the observations and further illustrates the GOBMs' deficiencies in simulating seasonal and spatial variability of the CO_2 uptake.

The assimilation model, ECCO-Darwin, has a negative bias after 2000 (-13.5 ± 3.0 μatm; Figure 9b), but this negative bias is not strongly reflected in the mean of the non-subsampled data, with the mean $p\text{CO}_2$ still being larger than that of the $p\text{CO}_2$ -products, which do not underestimate the $p\text{CO}_2$ relative to SOCAT. This further emphasizes that sampling distribution may play an important role in the magnitude of the biases calculated in any model. The

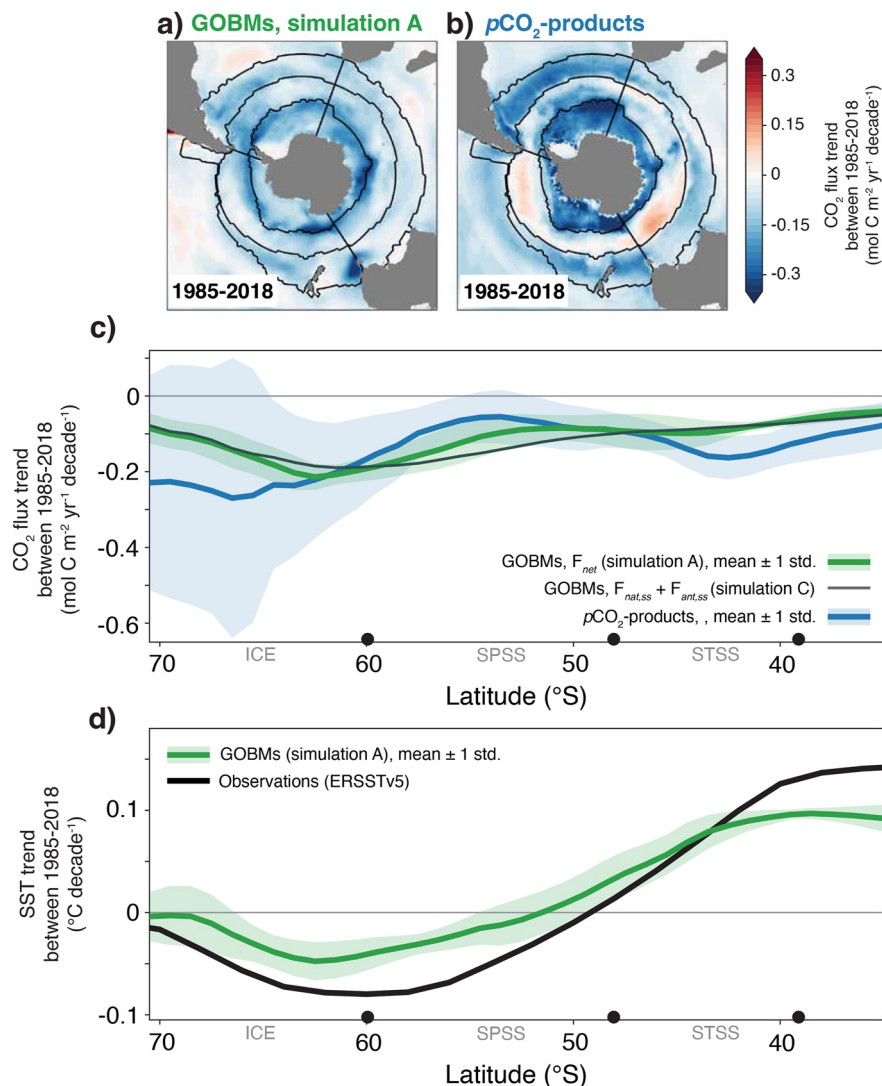


Figure 10. CO₂ flux trend between 1985 and 2018. (a, b) Spatial maps of the net CO₂ flux trend, for (a) the global ocean biogeochemistry models and (b) the pCO₂-products. (c) Zonal mean CO₂ flux trend 1985–2018 for the net CO₂ flux (blue: pCO₂-products and green: global ocean biogeochemistry models [GOBMs]) and the GOBM flux of F_{nat,ss} and F_{ant,ss}, that is, the flux as expected from increasing atmospheric CO₂ alone (green, dashed). (d) The sea surface temperature (SST) trend 1985–2018 in the GOBMs (green) and in the observational data set (black, NOAA Extended Reconstructed SST, ERSST, Version 5 (Huang et al., 2017)). Figures S14 and S15 in Supporting Information S1 split this analysis in the periods 1985–2000 (Figure S14 in Supporting Information S1) and 2001–2018 (Figure S15 in Supporting Information S1). Individual GOBM trends for F_{net}, as well as F_{nat,ss} plus F_{ant,ss} and SST are shown in Figure S16 in Supporting Information S1.

pCO₂ summer sampling bias in the Southern Ocean has long been recognised as a potential source of biases in pCO₂ estimates, particularly for the pCO₂-products that rely heavily on the in situ data (Djeutchouang et al., 2022; Gregor et al., 2017; Metzl et al., 2006; Ritter et al., 2017). The SOCCOM project increased the number of winter samples with pH-enabled profiling floats (from 2014), suggesting stronger outgassing during winter than previously shown (Gray et al., 2018). In RECCAP2, the B-SOSE assimilation model and the BGC-float pCO₂-products both make use of this data (Bushinsky et al., 2019; Verdy & Mazloff, 2017). Both of these estimates overestimate pCO₂ relative to SOCAT pCO₂ highlighting the challenge in consolidating ship-based SOCAT and BGC-float data.

3.4.2. Climate Versus CO₂ Effects on Trends in CO₂ Flux

Our analysis so far has indicated that the GOBMs reproduce seasonal temperature effects on CO₂ flux reasonably well (Figures 7d–7f), and a larger uncertainty is associated with imprints of circulation and biological activity. Next, we inspect the zonal mean and spatial patterns of the CO₂ flux trend between 1985 and 2018 (Figure 10).

Perhaps the most striking feature of the latitudinally averaged trends (Figure 10c) is that the uncertainty of the $p\text{CO}_2$ -products (blue) is much larger than that of the GOBMs (green). This is contrary to the seasonal cycle (Figures 7d–7f), where the $p\text{CO}_2$ -products are in much closer agreement than the GOBMs. This supports past studies which found that the sparse data in the Southern Ocean has a much larger influence on the accuracy of the decadal variability than on the seasonal variability (Gloege et al., 2021).

The $p\text{CO}_2$ -products place the largest trend of CO_2 uptake in the entire ICE biome; however, note the large variability between $p\text{CO}_2$ -products (blue shading in Figure 10c). The $p\text{CO}_2$ -products show a smaller (negative) peak in the trends in the STSS between about 40 and 45°S. The GOBMs, in contrast, exhibit less zonal variability with a large meridional gradient in the ICE biome with the strongest (negative) growth rate of the trend between ~60 and 65°S. The secondary peak in the STSS (observed in the $p\text{CO}_2$ -products) is not seen in the GOBM ensemble mean (green line).

Decadal variability, particularly for the $p\text{CO}_2$ -products, leads to weaker trends over the full period due to opposing trends over shorter time scales (see Figure 8, Figures S14 and S15 in Supporting Information S1). For example, the $p\text{CO}_2$ -products exhibit weakening CO_2 uptake in the Pacific and eastern Indian sector of the SPSS for the full period (Figure 10b). However, the same location experiences a growth in the sink for the period 2001–2018 (Figure S14b in Supporting Information S1). Differences between GOBMs and $p\text{CO}_2$ -products in the ICE biome are large, but the smaller area of the higher latitude region decreases the influence of the discrepancy (Figure 8). Although the difference in flux density between GOBMs and $p\text{CO}_2$ -products is larger in the ICE biome, the discrepancy in the STSS contributes more to the total flux trend discrepancy due to the larger area of the STSS biome (Figure 8).

We can attribute the growth in the strength of the CO_2 sink almost entirely to increasing atmospheric CO_2 levels, as shown by simulation C in the GOBMs (F_{ss} as black line in Figure 10c). The trends are only slightly modulated by climate change and variability, driving a weakening in the SPSS and strengthening in the northern part of the ICE biome (green F_{net} vs. black F_{ss} in Figure 10c). Thus, the effect of climate change and variability is substantially smaller than the uncertainty in the $p\text{CO}_2$ -products. But then what could be the cause of the discrepancies between the CO_2 flux trends of the GOBMs and $p\text{CO}_2$ -products?

Past work has found that fully coupled Earth System Models in CMIP6 do not capture circulation trends accurately, which is also observed as a deviation in SST trends, with no cooling simulated in the polar Southern Ocean (Beadling et al., 2020). However, we demonstrate that the GOBMs simulate SST trends from 1985 to 2018 rather well, including the cooling in the southern parts (Figure 10d), as also shown for the thermally driven component of the $p\text{CO}_2$ seasonal cycle (Figure 8). We can therefore not ascribe the discrepancies between GOBMs and $p\text{CO}_2$ -products in the trend of the CO_2 flux to temperature biases in the SST trends of the GOBMs.

The well-represented SST trends in the GOBMs is related to the choice of forcing the GOBMs with reanalysis data that itself depends on SST observations (Doney et al., 2007). In contrast to fully coupled Earth System models in CMIP6 (Beadling et al., 2020), the suite of models used here capture the decadal trend pattern of warming along the northern flank of the Antarctic Circumpolar Current (ACC), and cooling in the south (Figure 10, Armour et al., 2016; F. Haumann et al., 2020). The lack of warming south of 50°S was previously related to the wind-driven upwelling of deep water that had not yet been exposed to anthropogenic warming and by northward heat transport (Armour et al., 2016). More recently, the cooling was suggested to be caused by increased freshwater export from the ice region, which increases stratification and thus reduces the upward heat flux from below by warm water masses (F. Haumann et al., 2020). While the GOBM ensemble mean captures the latitudinal structure of the SST trend well, it underestimates the magnitude of peak cooling at around 60°S as well as peak warming north of 40°S.

We thus ascribe data sparsity as a reason for potential biases in the trend in the $p\text{CO}_2$ -products, with the large uncertainty in $p\text{CO}_2$ -products underlining that their estimate is currently not robust. Trends simulated in GOBMs are consistent within the ensemble, suggesting that they are caused by rising CO_2 acting on commonly reproduced characteristics of the Southern Ocean biomes. Nevertheless, biases in ocean circulation, sea ice and biology remain as possible reasons for biases in GOBMs.

3.5. Interior Ocean Storage of Anthropogenic Carbon 1994–2007

The focus of this section is the anthropogenic perturbation of DIC in a subset of the GOBMs (see Section 2.2.1), and in particular its accumulation rate over the period 1994 to 2007 ($\Delta\text{C}_{\text{ant}}$), in comparison with the eMLR(C^*)

observational estimate (Gruber, Clement, et al., 2019) and the ocean inverse model OCIMv2021 (DeVries, 2022). The eMLR(C*) product uses a multiple linear regression approach to estimate ΔC_{ant} and captures both the influence of CO₂-driven and climate-driven change in sea-air CO₂ fluxes and transports, whereas OCIMv2021 captures only the CO₂-driven changes.

All data classes agree in having the largest ΔC_{ant} inventories within and to the north of the STSS biome (Figure 11), whose southern boundary approximately corresponds to the northern edge of the ACC. This pattern is related to the mechanisms by which C_{ant} is taken up at the surface and exported to depth (Bopp et al., 2015; Mikaloff Fletcher et al., 2006; Morrison et al., 2022). Subpolar upwelling exposes old C_{ant}-poor waters to elevated atmospheric CO₂ concentrations and this, combined with strong winds, drives a large influx of C_{ant} in the SPSS biome (Figures 12a–12c). A small fraction of the C_{ant} moves southward and is exported within Antarctic Bottom Waters, while the largest fraction is transported northward within the upper cell of the meridional overturning circulation. C_{ant} air-sea fluxes remain elevated throughout the northward path, and are reinforced by the deep mixed layers in the regions where mode and intermediate waters are formed, which results in a secondary peak at around 40°S in some GOBMs, diluted by the ensemble mean (Figure 12c).

The effective transport of C_{ant} into the ocean interior relies on a number of physical processes, the dominant of which is the northward transport by the overturning circulation of the C_{ant} ventilated in the ocean interior by deep winter mixing (Frölicher et al., 2015; Morrison et al., 2022). The absorbed C_{ant} spreads northward along density surfaces within mode and intermediate waters (Figures 12d–12f) and is circulated within and out of the Southern Ocean by the subtropical gyres (Frölicher et al., 2015; D. C. Jones et al., 2016; Waugh et al., 2019). As a result, the largest C_{ant} inventories are displaced to the north with respect to the maximum air-sea C_{ant} influx (Figures 12b and 12c). Another pathway by which the C_{ant} inventory can build up without a corresponding surface influx is by southward advection and subsequent subduction of high-C_{ant} Subtropical Waters (Iudicone et al., 2016; Morrison et al., 2022).

The observation-based product eMLR(C*) and the ocean inverse model OCIM-v2021 have similar ΔC_{ant} accumulation rates when integrated over the Southern Ocean for the period 1994 through 2007 (0.52 and 0.47 PgC yr⁻¹, respectively, Figure 13), but differ in their horizontal (Figure 11) and vertical (Figure 12) patterns. The eMLR(C*) exhibits particularly low ΔC_{ant} values at subpolar and high latitudes (Figure 12g), especially in the Pacific sector (Figure 11). The GOBMs multi-model-mean of ΔC_{ant} accumulation rates over the same 1994 through 2007 period and integrated within the Southern Ocean (Figure 13) is 0.46 ± 0.11 PgC yr⁻¹, that is, 7% lower than the mean of the two observational estimates considered here. 6 out of the 12 GOBMs fall within the 19% range of the observational eMLR(C*) uncertainty. Two thirds of all GOBMs (hereafter “GOBMs low”) have lower than observed ΔC_{ant} accumulation rates (0.39 ± 0.11 PgC yr⁻¹, about 20% lower than the observational estimates). The remaining GOBMs (hereafter “GOBMs high”) have higher than observed ΔC_{ant} accumulation rates (0.58 ± 0.07 PgC yr⁻¹, about 17% higher than the observational estimates). “GOBMs high” have a higher ΔC_{ant} storage than “GOBMs low” throughout the Southern Ocean (Figures 11c, 11d, and 12c), higher C_{ant} air-sea fluxes (Figure 12c), higher SSS in the SPSS and STSS biomes and mixed layer depths especially in the SPSS biome (Texts S3 and S4 and Figure S17 in Supporting Information S1). Along the zonal mean section, all GOBMs show a southward shift in ΔC_{ant} with respect to eMLR(C*) shown by a north-south dipole in the upper 1 km (Figure 12h), as similarly found in the comparison between OCIM-v2021 and eMLR(C*) (Figure 12g). With respect to OCIM-v2021, GOBMs show higher ΔC_{ant} above 1000 m depth and lower ΔC_{ant} beneath (Figure 12i). This could point to insufficient ventilation of C_{ant} in “GOBMs low” models (Figure S19 in Supporting Information S1), which represent the majority of the GOBMs. The amount of spread and the overall underestimate of ΔC_{ant} in the GOBMs is consistent with Earth System Models analyzed by Frölicher et al. (2015) and Terhaar et al. (2021), supporting the argument that biased ocean model dynamics and water mass properties rather than biases in the atmospheric forcing cause the C_{ant} underestimate (Bourgeois et al., 2022; Terhaar et al., 2021).

Integrated over the Southern Ocean, we find that the model spread in ΔC_{ant} accumulation rates from 1994 to 2007 can be largely explained (81% variance explained) by the spread in accumulated C_{ant} until 1994 (Figure 13), suggesting a coherent scaling between long-term and recent C_{ant} accumulation rates. The model spread in ΔC_{ant} accumulation rates is also related with the spread in C_{ant} air-sea fluxes averaged over 1994–2007 (78% variance explained). These results show that past long-term ΔC_{ant} accumulation rates are a better predictor for present ΔC_{ant} accumulation rate than present C_{ant} air-sea fluxes. The reason for this is that C_{ant} air-sea fluxes are linked to changes in C_{ant} storage through ocean transport, which may differ substantially between models (Bourgeois et al., 2022; Frölicher et al., 2015; Terhaar et al., 2021). This becomes obvious when considering the myriad of processes involved, including the strength of the overturning circulation, the strength of the subtropical gyres,

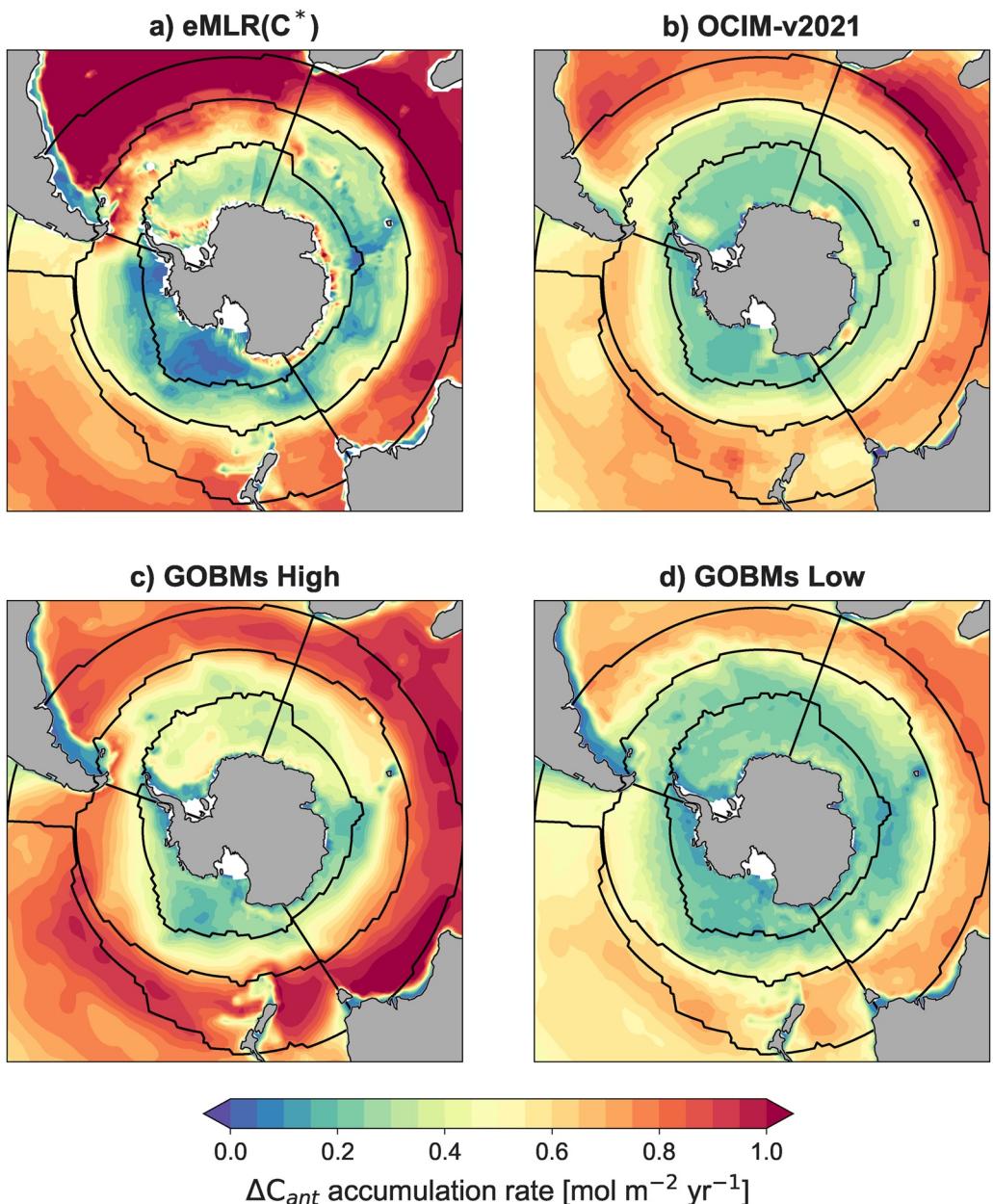


Figure 11. ΔC_{ant} yearly accumulation rate over the period 1994–2007 integrated until 3,000 m depth in the observationally constrained estimates (a) eMLR(C^*) (Gruber, Clement et al., 2019) and (b) OCIM-v2021, in (c) “GOBMs high” (CESM-ETHZ, MRI-ESM2-1, NorESM-OC1.2, and NEMO-PlankTOM12.1) and in (d) “GOBMs low” (CCSM-WHOI, CNRM-ESM2-1, EC-Earth3, FESOM-RECoM-LR, ORCA025-GEOMAR, ORCA1-LIM3-PISCES, and MPIOM-HAMOCC). Individual global ocean biogeochemistry models are shown in Figure S4 in Supporting Information S1. The robustness of the patterns has been tested as explained in Text S4 in Supporting Information S1. Contours show the boundaries of the ice, subpolar seasonally stratified, and subtropical seasonally stratified biomes. Values below 3,000 m are not shown because of the low signal-to-uncertainty ratio in eMLR(C^*).

the isopycnal stirring by mesoscale eddies, and localized subduction dynamics (Morrison et al., 2022; Sallée et al., 2012). The different way in which the GOBMs simulate these transport processes is possibly linked to the large model spread in ΔC_{ant} accumulation rates among GOBMs. Past studies have found that SSS affects the surface ocean density in the formation regions of mode and intermediate waters and could be used as a constraint of the C_{ant} air-sea fluxes, and thus of the C_{ant} storage within the recently ventilated water masses (Terhaar et al., 2021). In this study and in Terhaar et al. (2023), we find that SSS explains a lower variance in the

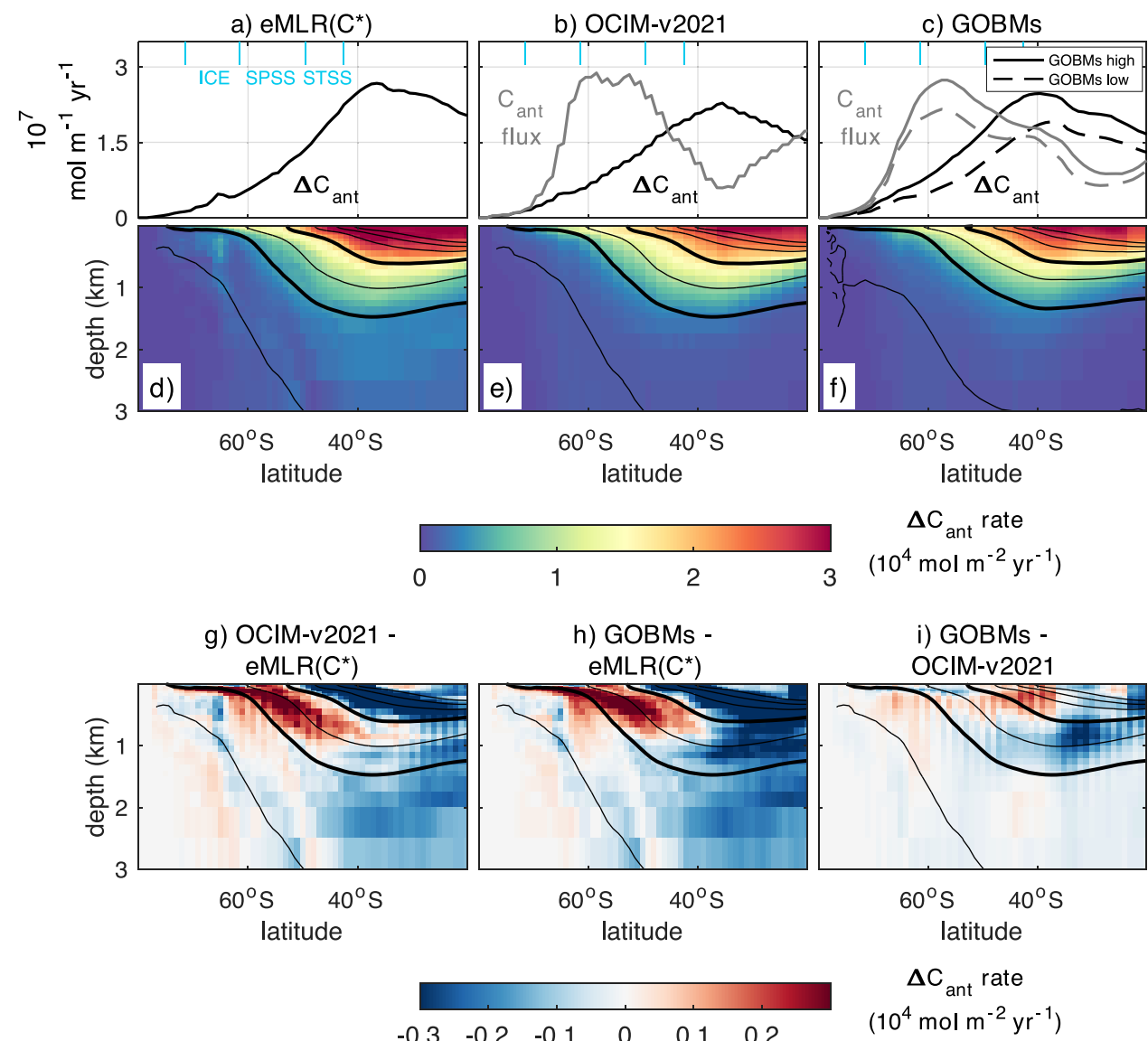


Figure 12. Zonal integrals of ΔC_{ant} yearly accumulation rate from 1994 to 2007 and of air-sea C_{ant} fluxes (positive downwards) averaged between 1994 and 2007 for (a, d) eMLR(C*), (b, e) OCIM-v2021, and (c, f) global ocean biogeochemistry models (GOBM). (a–c) (black line) ΔC_{ant} column inventory (0–3,000 m) and (gray line) air-sea C_{ant} fluxes; for the GOBM, the distinction is made between “GOBM high” (full lines) and “GOBM low” (dashed lines). See figure caption 11 or Figure 13 for a list of GOBM high and GOBM low. (g–i) Anomalies of ΔC_{ant} accumulation rates in (g) OCIM-v2021 with respect to eMLR(C*), (h) GOBM with respect to eMLR(C*), and (i) GOBM with respect to OCIM-v2021. In all sections, contours show mean potential density (with a 0.03 kg m^{-3} spacing) referenced to the surface in World Ocean Atlas 2018 (Boyer et al., 2018), where thick lines indicate the $1,026.9$ and $1,027.5 \text{ kg m}^{-3}$ isopycnals. Anomalies of individual GOBM shown in Figure S18 in Supporting Information S1 (with respect to eMLR(C*)) and Figure S19 in Supporting Information S1 (with respect to OCIMv2021).

ΔC_{ant} accumulation rates ($R^2 = 0.61$; Figure 13) and in the C_{ant} air-sea fluxes ($R^2 = 0.57$, Terhaar et al., 2023) with respect to the ESMs ($R^2 = 0.74$) analyzed by Terhaar et al. (2021). The relationship may be weaker due to the different suite of models used in the ESM and GOBM ensembles and remaining biases associated with incomplete spin-up (Terhaar et al., 2023).

4. Discussion

4.1. Summary and Progress Since RECCAP1

We provide an updated estimate of the Southern Ocean carbon sink (see Figure 1 for regional extent). The numbers we present (Table 3) are not directly comparable with the RECCAP1 estimate (Lenton et al., 2013) due

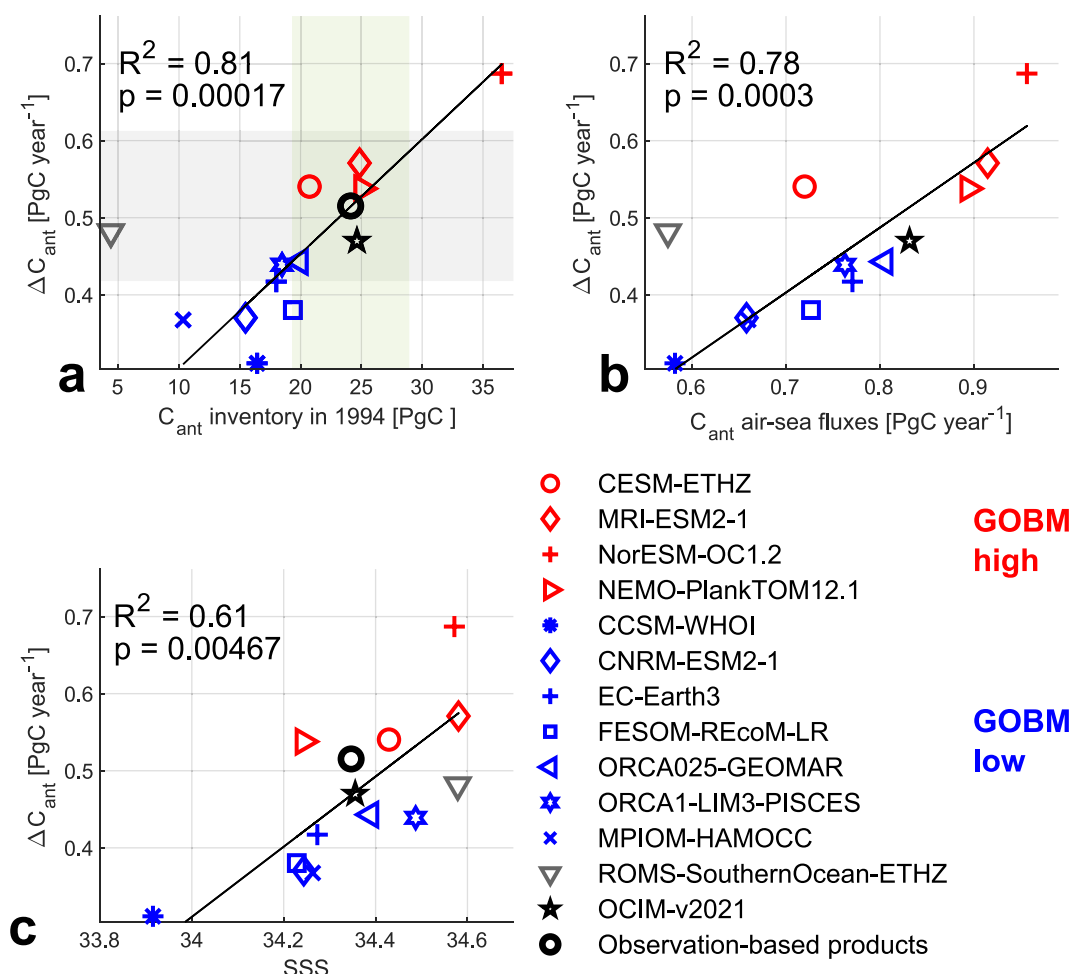


Figure 13. Scatter plots showing relationships between ΔC_{ant} accumulation rates between 1994 and 2007 (integrated to 3,000 m) and different quantities namely (a) the cumulative C_{ant} in 1994 integrated over the Southern Ocean, (b) air-sea C_{ant} fluxes averaged between 1994 and 2007 and integrated over the Southern Ocean, (c) sea surface salinity (SSS) horizontally averaged over the subpolar seasonally stratified and subtropical seasonally stratified biomes (which show consistent SSS anomaly patterns, Figure S17 in Supporting Information S1). Shown are a subset of the global ocean biogeochemistry models (GOBMs) (see Section 2.3), the OCIM-v2021 data-assimilated model, the observation-based cumulative C_{ant} until 1994 (C* method, Sabine et al., 2004) and the 1994–2007 ΔC_{ant} from (eMLR(C*) method, Gruber, Clement, et al., 2019), and SSS from EN4.2.1 (Good et al., 2013). Thin black lines show the linear fit of the data for the GOBMs only, with the explained variance (R^2) and the p -value indicated for each regression. The gray shading in panel (a) indicates the 19% uncertainty levels around the mean of eMLR(C*) (Southern Hemisphere uncertainty estimate, based on Table 1, Gruber, Clement, et al., 2019) and the green shading the 20% uncertainty levels around the C*-based estimate of cumulative C_{ant} until 1994 (global uncertainty estimate Sabine et al., 2004; Matsumoto & Gruber, 2005). Models that have a ΔC_{ant} storage higher than the average of the two observationally constrained data sets (“GOBMs high”) are shown in red, whereas the models in which it is lower (“GOBMs low”) are shown in blue. Because of its different spin-up procedure, ROMS-SouthernOcean-ETHZ is shown in the plots but has been excluded from the regression analysis. For OCIM-v2021, CNRM-ESM2-1, and MPIOM-HAMOCC the ΔC_{ant}^{ss} is shown, whereas in others the sum of steady state and nonsteady state is shown. As discussed in Text S2 in Supporting Information S1, ΔC_{ant}^{ns} accumulation rates are about 10%–20% of the total ΔC_{ant} .

to different region definitions (Figure 1) and periods (1990–2009 vs. 1985–2018). The RECCAP1 regional definition of the Southern Ocean (44–75°S) cut across and missed a large part of the strong CO₂ uptake north of the Subantarctic Front. Recalculating the RECCAP2 numbers for the RECCAP1 region and period each reduces the sink estimate by ~50% resulting in only ~25% of its original value. A key result thus is that RECCAP2 estimates a weaker Southern Ocean carbon sink by 50% compared to RECCAP1. In RECCAP2 we find that the SPSS and ICE biomes are a weaker sink than in RECCAP1, and with the absence of the STSS, a region of strong C_{ant} uptake, the other regions gain importance.

Table 3

Comparison of the Southern Ocean Carbon Sink Estimate With the Estimate Presented in RECCAP1 (Lenton et al., 2013), Which Used a Different Definition of the Southern Ocean Region (44° – 75° S) and Covered a Different Period (1990–2009)

| Estimate | GOBMs (Pg C yr $^{-1}$) | Observation-based (Pg C yr $^{-1}$) |
|--|-----------------------------|---|
| RECCAP2 1985–2018 | -0.75 ± 0.28 | -0.73 ± 0.07 |
| RECCAP2 1985–2018 (44° – 75° S) | -0.39 ± 0.24 | -0.30 ± 0.04 |
| RECCAP2 1990–2009 (44° – 75° S) | -0.22 ± 0.25 | -0.14 ± 0.09 |
| RECCAP1 1990–2009 (44° – 75° S) | -0.43 ± 0.38 | -0.27 ± 0.13 |

Note. GOBMs: Global Ocean Biogeochemistry Models. Reported numbers are means \pm one standard deviation. For RECCAP1, the median of all models is reported.

The observational and modeling communities have made substantial progress on quantifying and characterizing the Southern Ocean carbon sink since RECCAP1 (Lenton et al., 2013). The creation of the Surface Ocean CO_2 Atlas and its annual updates have marked a step-change by facilitating the development of statistical models (a.k.a. $p\text{CO}_2$ -products). The large and diverse ensemble of $p\text{CO}_2$ -products help to identify the robust features of the Southern Ocean carbon sink. The $p\text{CO}_2$ -products have a relatively small spread compared to the global ocean biogeochemistry models in terms of mean and seasonal cycle, indicating that the uncertainty from differences in mapping methods is small. However, the spread in the trend estimates is in fact larger in the products than in the GOBMs (Figure 10). Further, the narrow spread in mean and seasonal cycle does not include the uncertainties due to sparse $p\text{CO}_2$ observations in the Southern Ocean, particularly in winter and before the 2000's (Ritter et al., 2017). In addition, $p\text{CO}_2$ -products share the uncertainties with GOBMs associated with the bulk formulation of air-sea CO_2 exchange (Fay et al., 2021; Wanninkhof et al., 2009). While they do have their shortcomings, the $p\text{CO}_2$ products are an advance for constraining the Southern Ocean carbon sink compared to the atmospheric inversions that were used in RECCAP1 (Lenton et al., 2013). This is because the surface ocean $p\text{CO}_2$ observations provide a more direct constraint on the air-sea

ing the Southern Ocean carbon sink compared to the atmospheric inversions that were used in RECCAP1 (Lenton et al., 2013). This is because the surface ocean $p\text{CO}_2$ observations provide a more direct constraint on the air-sea

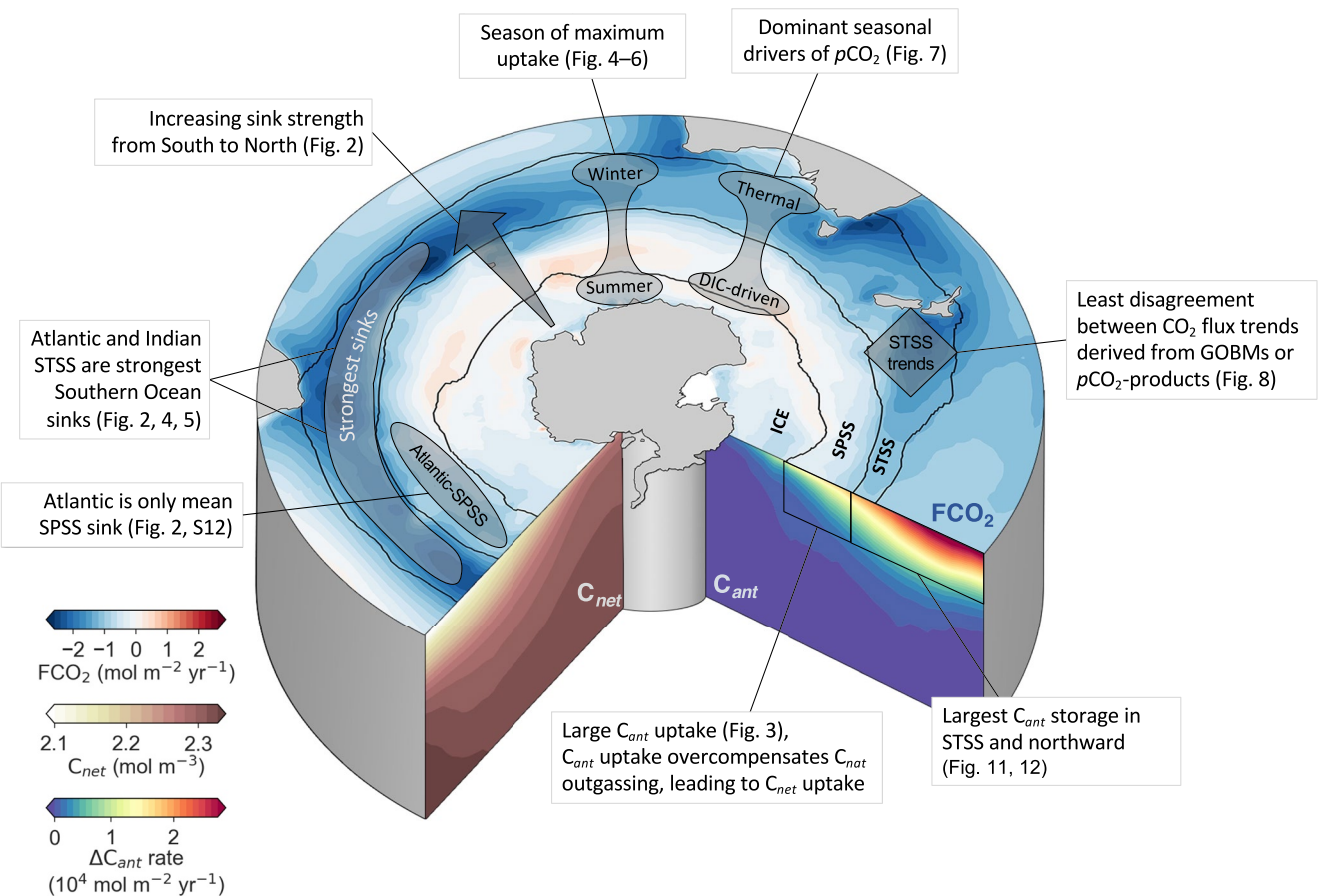


Figure 14. Main characteristics of the Southern Ocean carbon cycle 1985–2018. The surface ocean color shading depicts the net air-sea CO_2 flux (FCO_2) as the average of the ensemble means from $p\text{CO}_2$ -products and Global Ocean Biogeochemistry Models (GOBMs). Blue color denotes a CO_2 flux into the ocean, and red color a flux out of the ocean. The section on the right shows the zonally integrated anthropogenic carbon (C_{ant}) accumulation rate in the ocean interior from GOBMs. The section on the left shows the zonally averaged concentration of total (or “net”) carbon (C_{net}). ICE: ice-covered biome, SPSS: Subpolar Seasonally Stratified Biome, and STSS: Subtopical Seasonally Stratified Biome.

CO₂ flux than the relatively small atmospheric CO₂ signals over the ocean that form the basis of the atmospheric inversions.

4.1.1. Model Deficiencies

The larger GOBM ensemble provides a more representative process-based estimate and the spread in GOBMs has been reduced since RECCAP1 (see Table 3, Lenton et al., 2013). The remaining spread is nevertheless large and points toward critical need for model development, where the largest sources of uncertainty stem from biological process description and circulation, which vary in importance depending on flux component (natural, anthropogenic, etc.), and spatio-temporal scale of interest. In terms of the anthropogenic component, the 12 GOBMs analyzed here have a 24% spread (standard deviation around the mean) in the C_{ant} accumulation rates, which is marginally larger than the ~20% uncertainty associated with the observational estimates of ΔC_{ant} and C_{ant} (even though caution is warranted when directly comparing the uncertainty estimates, which are computed formally different across data classes; Gruber, Clement, et al., 2019; Sabine et al., 2004). Overall, the GOBM ensemble mean underestimates the observation-based estimates of the C_{ant} accumulation up to 1994 by 19% and the change between 1994 and 2007 by 7%. Admittedly, the GOBM ensemble analyzed here is relatively small, and the underestimation of C_{ant} and ΔC_{ant} is in the range of the uncertainty ranges of the observational estimates.

Despite the caveats of small ensemble size and overlapping uncertainty ranges, we can nonetheless speculate that the detected underestimation is likely related to a combination of physical, chemical, and methodological factors. First, our results point to too little or too shallow ventilation of mode and intermediate waters (Figure 12i), the causes of which can be related to insufficient vertical mixing or too sluggish northward export of the subducted waters (Morrison et al., 2022). However, while sea-surface salinity (SSS) was singled out as a strong predictor of C_{ant} air-sea fluxes in an ESM ensemble analyzed by Terhaar et al. (2021), in our study and in Terhaar et al. (2023), SSS was not found to be a clear constraint of the anthropogenic CO₂ uptake and its interior storage in the GOBMs. Rather, Terhaar et al. (2023) find that biases in the normalized surface Revelle factor could explain the underestimation of C_{ant} uptake. Finally, the relatively high pre-industrial CO₂ mixing ratios related to late starting dates in several GOBMs are likely causing an underestimation of the cumulative C_{ant} storage, which is especially large in the Southern Ocean (Terhaar et al., 2023).

For the natural carbon fluxes, the difficulty in capturing the delicate balance between physical and biological processes is clearly manifested by the large model spread (Figure 3). In addition, the different spin-up procedures could play a role. Terhaar et al. (2023) indicate that the natural CO₂ flux component may be biased toward uptake that is too strong, possibly related to GOBMs not being in steady-state (Terhaar et al., 2023), which is particularly relevant in the Southern Ocean where old water masses resurface. While long preindustrial spin-ups would bring the GOBMs closer to steady-state and thus reduce drift, they may come at the cost of less realistic surface conditions and their response to climate change and variability (Séférian et al., 2016). Interestingly, the two data-assimilated GOBMs differ to a large extent, illustrating that dynamical processes in these models may still override information gained from assimilated observations.

4.1.2. GOBM and pCO₂-Product Discrepancies

The averages of the GOBM and pCO₂-product ensembles agree for many key estimates, showing progress over the past 10 years: the mean and spatial distribution of the sink is in good agreement (Figure 2), although discrepancies of the magnitude and, particularly, the trends still persist (Figures 8 and 10; see also Canadell et al., 2021). The fact that these ensemble means agree so well in many respects provides some confidence in the Southern Ocean CO₂ flux estimates because they are nearly independent. However, the agreement of GOBMs and pCO₂-products on the mean CO₂ flux is partly a result of compensation of regional and seasonal discrepancies (Figures 4, 5, and 8).

The concerning discrepancies in the trend cannot be explained by GOBM biases in warming trends as these are well reproduced (Figure 10). Similarly, the GOBM ensemble is not systematically biased toward formation of mode and intermediate waters that is too weak, in contrast to the ESMs, and an effect on the trend of the ocean carbon sink could not be evidenced (Terhaar et al., 2023). Further potential candidates for GOBM biases, which were not explored here, are stratification (Bourgeois et al., 2022), mixing, and mixed layer dynamics, which could also lead to excess carbon accumulation in the surface layer and thus may be the driver for the overestimation of the surface Revelle factor. In the pCO₂-products, the trend is subject to biases by data sparsity (Gloegge et al., 2021; Hauck et al., 2023).

The agreement in the mean air-sea CO_2 flux between GOBMs and $p\text{CO}_2$ -products is also highly susceptible to the choice of river flux adjustment that either locates most outgassing of river-derived carbon in the Southern Ocean (Aumont et al., 2001) or in the tropical Atlantic (Lacroix et al., 2020). Reasons for the discrepancy between Aumont et al. (2001) and Lacroix et al. (2020) may be because of specific choices in nutrient and carbon input, lability of organic matter, resulting ocean model transport (see also the discussion in Terhaar et al., 2023). We here chose to use the river flux adjustment of Lacroix et al. (2020), scaled up to a global value of 0.65 PgC yr^{-1} , resulting in a small adjustment for the Southern Ocean of 0.04 PgC yr^{-1} . In contrast, the Southern Ocean (south of 20°S) adjustment based on Aumont et al. (2001) that is so far used in the Global Carbon Budget is higher by one order of magnitude (0.32 PgC yr^{-1}) and can explain the large mismatch in the mean flux (but not its trend) between GOBMs and $p\text{CO}_2$ products in the Southern Ocean in the Global Carbon Budget (Friedlingstein et al., 2022).

4.2. Seasonal Cycle and Thermal Versus Non-Thermal Drivers

As a community, we have a good understanding of the mechanisms that drive $p\text{CO}_2$ seasonality in the Southern Ocean (Lenton et al., 2013), but we do not fully understand their magnitudes, opposing or synergistic, in different seasons and regions (Mongwe et al., 2018). Part of this lack of understanding is due to a lack of observations throughout all seasons, though particularly acute during winter (Bushinsky et al., 2019; Gray et al., 2018; Sutton et al., 2021). Further, complex biological processes affecting $p\text{CO}_2$ in summer are more difficult to accurately describe in GOBMs (Mongwe et al., 2018).

The poor sampling distribution of $p\text{CO}_2$ in the Southern Ocean, particularly the bias toward summer sampling, could result in a misrepresentation of the seasonal cycle in $p\text{CO}_2$ -products (Ritter et al., 2017). This may be shown by the narrow ensemble spread of the $p\text{CO}_2$ -products during winter (Figures 7g–7i). That being said, an observing system simulation experiment (OSSE) showed that the seasonal cycle in most of the Southern Ocean is in fact well captured by one $p\text{CO}_2$ product (Gloege et al., 2021). The narrower GOBM spread of the non-thermal $p\text{CO}_2$ component during winter may also suggest that winter-time processes (circulation) are less complex than summer (circulation and biology, Figures 7g–7i).

The introduction of biogeochemical Argo floats since the mid 2010's has increased the number of winter observations (relative to the available ship-based observations), albeit inferred from pH and estimated total alkalinity and thus associated with a higher uncertainty (Williams et al., 2017). The machine learning approaches that include float-based observations result in stronger winter outgassing (Figure 4, Bushinsky et al., 2019). Direct $p\text{CO}_2$ measurements showed that the years used to train the machine learning model (2015–2018) may have had anomalously high $p\text{CO}_2$ (Sutton et al., 2021). However, if this is in fact the case, and not related to sampling locations, this may indicate much larger interannual variability in the Southern Ocean than the majority of the $p\text{CO}_2$ -products currently estimate (Figure 8). Incorporating these data is thus potentially an important goal for $p\text{CO}_2$ -products, but it has proven difficult to incorporate the float-based $p\text{CO}_2$ estimates further back in time than 2015, the start of the BGC-float record and account for their higher uncertainty (Bushinsky et al., 2019; Williams et al., 2017).

GOBMs also have a lower $p\text{CO}_2$ ensemble spread during winter compared with summer and agree on the spatial location of the winter flux minimum (Figure 4). Nevertheless, the range in magnitude is still more than twice as large as those of the $p\text{CO}_2$ -products (Figures 7g–7i). Since the thermal component is well captured in GOBMs (Figures 7d–7f), the non-thermal physical drivers (i.e., circulation) determines the uncertainty observed in winter. In summer, GOBMs have difficulty capturing the delicate balance between biological and physical processes that leads to a large spread in model $p\text{CO}_2$ and fluxes (Mongwe et al., 2018). GOBMs may thus benefit from more process-based studies that further our understanding of $p\text{CO}_2$ drivers during summer, that is, biological productivity, respiration, remineralization, and sinking of organic carbon as part of the biological carbon pump.

4.3. Temporal Variability of CO_2 Fluxes

Our analysis reduces the previously reported discrepancy in variability of Southern Ocean air-sea CO_2 fluxes between data classes (GOBMs and $p\text{CO}_2$ -product ensemble means, Gruber, Landschützer, & Lovenduski, 2019). We relate the growing agreement to the larger ensemble of $p\text{CO}_2$ -products in our study, with the newer additions having a substantially lower variability than the two $p\text{CO}_2$ -products (Jena-CarboScope and SOM-FFN) used by Gruber, Landschützer, and Lovenduski (2019). A recent study using the same RECCAP data base also concluded

that there is agreement on the magnitude of interannual variability between GOBMs and $p\text{CO}_2$ -products (Mayot et al., 2023).

The interannual to decadal variability of Southern Ocean air-sea CO_2 fluxes was discussed extensively in the literature, and was often related to variations in the Southern Annual Mode (SAM) (Hauck et al., 2013; Lenton & Matear, 2007; Le Quéré et al., 2007; Lovenduski et al., 2007; Mayot et al., 2023; Nicholson et al., 2022). Also, regional wind variability linked to the zonal wavenumber 3 was suggested as a driver of interannual CO_2 flux variability driving both the weakening in the 1990's and the strengthening in the 2000's (Keppler & Landschützer, 2019; Landschützer et al., 2015). The arguments of SAM or wave number 3 as dominant drivers of CO_2 flux interannual variability might not be fully independent from each other, as previously a wave number 3 like pattern was reported to describe MLD anomalies during positive SAM events (Sallée et al., 2010).

The fact that the maximum IAV of GOBMs is found in the SPSS Indo-Pacific sector (Section 3.4, Figure S12 in Supporting Information S1) supports the argument of the above mentioned references that upwelling of carbon-rich deep water and related outgassing of natural carbon in response to a positive SAM and strengthening of westerly winds may be the dominant driver of interannual variability (DeVries et al., 2017). This is further supported by studies of atmospheric potential oxygen (APO), which can be used as a tracer of ocean-only processes from measurements of CO_2 and O_2 at atmospheric stations (Stephens et al., 1998). Nevison et al. (2020) showed that the interannual variations of APO seasonal minimum from stations in the Southern Hemisphere were strongly correlated with the SAM during years of positive phase. Further, they showed that GOBMs (as analyzed in this study) can capture the variability of CO_2 and APO fluxes driven by the SAM variations during the austral winter months. However, the study of Nevison et al. (2020) also illustrated that the SAM index variability cannot fully explain the changes in APO seasonal winter minima suggesting that other factors or modes of variability such as ENSO could impact the CO_2 and O_2 air-sea fluxes of the Southern Ocean as also previously suggested in an ocean modeling study (Verdy et al., 2007).

On top of the interannual variability, on which $p\text{CO}_2$ products and GOBMs seem to reach reasonable agreement, discrepancies in the CO_2 flux trend since 2000 have emerged (Figure 8, Friedlingstein et al., 2022). These discrepancies highlight a major knowledge gap and urgently need to be resolved by critical analysis of potential biases in $p\text{CO}_2$ -products as well as GOBMs (see Section 4.1). While there is no evidence so far that adjustments of CO_2 fluxes based on model evaluation of interfrontal salinity and Revelle factor affect the trend (Terhaar et al., 2023), data sparsity tends to lead to an overestimation of decadal variability and trend in at least two of the $p\text{CO}_2$ -products (Gloegge et al., 2021; Hauck et al., 2023). Hence, both data classes need to be inspected for deficiencies.

4.4. Zonal Asymmetry of the Fluxes

While the primary spatial mode of variability in the Southern Ocean is from north to south, zonal variability in the dynamics, biogeochemistry, and carbon fluxes have been reported in the literature (Landschützer et al., 2015; Prend et al., 2022; Rintoul, 2018; Tamsitt et al., 2016). Similarly, we find substantial zonal asymmetry in both the mean states, and seasonal and interannual variability of the Southern Ocean CO_2 fluxes (Figures S10 and S12 in Supporting Information S1); yet many of our results have been presented in a zonally averaged perspective for the sake of brevity.

In this work, we find that the largest zonal asymmetries in the Southern Ocean mean air-sea CO_2 flux occur in the SPSS biome (Figures 4b–4e and Figure S12 in Supporting Information S1). Here, the Pacific and Indian sectors are larger sources (or weaker sinks) of CO_2 to the atmosphere than the Atlantic sector. This is consistent with the $p\text{CO}_2$ -based products (Figures S12d–S12f in Supporting Information S1). The float-based $p\text{CO}_2$ -products amplify this winter outgassing dramatically. However, the GOBMs and the assimilative model ensemble averages do not show a coherent and convincing increase in outgassing in the Indian and Pacific relative to the Atlantic. The zonal asymmetry reported in the observation-based products is consistent with a recent BGC-float-based study that reported stronger outgassing in the Indian and Pacific sectors of the Southern Ocean (Prend et al., 2022). The authors attributed this dominance to stronger winter-time entrainment of deep waters to the surface in these regions. The zonal asymmetry is also apparent in the air-sea CO_2 fluxes decomposed into natural and anthropogenic contributions (Figure S7 in Supporting Information S1). Here, too, the SPSS is the region with the greatest asymmetry. In the Indian sector, the large natural outgassing fluxes of the ensemble mean are nearly perfectly opposed by the anthropogenic uptake.

4.5. Link Large-Scale Synthesis to Observational Programs

The analysis presented here provides a synthesis of large-scale data sets with a focus on budgets, spatial, and temporal patterns of fluxes and carbon accumulation, and a first-order assessment of large-scale processes (e.g., thermal vs. non-thermal, anthropogenic vs. natural carbon fluxes). In particular, it highlights spatio-temporal windows for which discrepancies between data classes are largest (e.g., magnitude of winter outgassing, delicate balance of physical vs. biological processes in summer, magnitude of decadal trend of the Southern Ocean carbon sink). Importantly, this synthesis builds on contributions from many individual groups contributing repeat observations of surface and interior ocean biogeochemical properties from research vessels and ships of opportunity (e.g., Hoppe et al., 1998; Metzl et al., 1999; Pardo et al., 2017; Talley et al., 2016; van Heuven et al., 2014). The ship-based observations form the cornerstone for many of the data classes in this study: observation-based ocean interior estimates of CO_2 storage assess changes in deep ocean measurements of CO_2 , the surface $p\text{CO}_2$ estimates use observations from ships of opportunity, and the GOBMs are evaluated against ocean interior observations. And while sampling biases and gaps in the ship-based measurements may be filled by autonomous platforms with lower accuracy (e.g., BGC-floats), they will always require crossover validation measurements from the high-accuracy ship-board measurements. This emphasizes that the ship-based observations need to continue into the future to characterize the evolution of the Southern Ocean carbon cycle. This will only become more important, once stabilization of atmospheric CO_2 will lead to a larger weight on ocean processes for control of air-sea fluxes relative to the current quasi-exponential growth rate of atmospheric CO_2 .

Further, detailed regional process studies employing a wide range of methodologies across disciplines are also important to further our holistic understanding of the Southern Ocean carbon cycle and to improve the description of biogeochemistry and ecosystem dynamics in GOBMs, particularly in summer. One example for such an interdisciplinary field program is along the continental shelf west of the Antarctic Peninsula where shipboard observations indicate a strong, near-shore summer undersaturation of surface $p\text{CO}_2$ (Eveleth et al., 2017) and seasonal reduction in surface DIC (Hauri et al., 2015). The seasonal trends in the ocean CO_2 system on the shelf reflect a combination of biological net community production (Ducklow et al., 2018) and meltwater input diluting surface DIC and alkalinity (Hauri et al., 2015). Regional ocean biogeochemical models simulate similar onshore-offshore gradients in surface chlorophyll, biological productivity, DIC, and $p\text{CO}_2$ as well as the observed large interannual biophysical variability associated with year-to-year variations in seasonal sea-ice advance and retreat phenology (Schultz et al., 2021). Observed decadal trends for the region from the early 1990s to late 2010s indicate that reduced sea-ice extent associated with climate change drives an increase in upper ocean stability, phytoplankton biomass and biological DIC drawdown, resulting in a growing net downward air-sea CO_2 flux during summer (Brown et al., 2019). Recent year-round, autonomous mooring observations of $p\text{CO}_2$ and pH suggest a gradual increase in surface ocean $p\text{CO}_2$ and DIC over the fall and winter, with CO_2 outgassing during winter when $p\text{CO}_2$ is supersaturated largely blocked by sea-ice cover (Shadwick et al., 2021; M. Yang et al., 2021). Similar large-scale programs are needed in other parts of the Southern Ocean given its size and importance in the global carbon cycle. On-going research activities, also as part of the Southern Ocean Observing System, for example, in the Ross (Smith et al., 2021) and Weddell Seas (Arndt et al., 2022) have the potential of being extended.

5. Conclusions

Here, we present a schematic overview that summarizes the main characteristics of the Southern Ocean carbon cycle 1985–2018, as derived in this analysis and its Supporting Information S1 (Figure 14). In general, the sink strength for atmospheric CO_2 (net CO_2 flux, FCO_2) increases from South to North, but with important zonal asymmetry. The Atlantic and Indian Ocean sectors of the Subtropical Seasonally Stratified biome (STSS) are the regions that act as strongest sinks. In the Subpolar Seasonally Stratified biome (SPSS), the Atlantic sector stands out as the only sector acting as an annual mean CO_2 sink. Also the seasonal cycle shows a distinct north-south gradient. In the ice-covered biome (ICE) the peak uptake occurs in summer and is driven by the seasonal cycle of DIC, that is, by physical DIC transport and biological processes. In contrast, the dominant driver of the seasonal cycle of CO_2 uptake in the STSS is temperature, and thus the season of peak uptake occurs in winter. Trends in net CO_2 uptake derived from Global Ocean Biogeochemistry Models (GOBMs) and surface ocean $p\text{CO}_2$ observation based products ($p\text{CO}_2$ -products) disagree in all biomes, but the discrepancy is strongest in the Pacific sector of the STSS. In terms of anthropogenic CO_2 (C_{anth}), the strongest uptake occurs in the SPSS. This is not visible in the map of net CO_2 flux, because the anthropogenic uptake manifests itself as a suppression of natural CO_2 outgassing. The largest anthropogenic carbon storage occurs in the STSS and northward.

Our analysis confirms the important role of the Southern Ocean in the global carbon cycle although RECCAP2 estimates a 50% smaller Southern Ocean CO₂ sink for the same region and timeframe as RECCAP1. We have highlighted key knowledge gaps that need to be closed through extended observation systems and augmented process descriptions in the dynamic models in order to further reduce uncertainties.

Data Availability Statement

All RECCAP2 data is available at Zenodo: Müller (2023).

The processed data for this study is available at Hauck et al. (2023a).

Code for each figure is in the GitHub repository: <https://github.com/RECCAP2-ocean/Southern-Ocean>, with a frozen version deposited at Hauck et al. (2023b).

Acknowledgments

We thank the editor for handling the manuscript and Galen McKinley and one anonymous reviewer for their constructive feedback. Funding to J. Hauck was provided by the Initiative and Networking Fund of the Helmholtz Association (Helmholtz Young Investigator Group Marine Carbon and Ecosystem Feedbacks in the Earth System [MarESys], Grant VH-NG-1301), by the ERC-2022-STG OceanPeak (Grant 101077209) and by the European Union's Horizon Europe research and innovation program under Grant 101083922 (OceanICU Improving Carbon Understanding). J.H., L.G., M.H., N.G., and P.M. acknowledge funding from the European Union's Horizon 2020 research and innovation programme under Grant 820989 (project COMFORT). L. Patara acknowledges funding from the project PA 3075/2-1 by the German Research Foundation and the North German Supercomputing Alliance (HLRN) for providing computing power for the experiments. L. Gregor, M. Hague, and N. Gruber further acknowledge funding from the European Union's Horizon 2020 research and innovation programme under Grant 821001 (SO-CHIC project), 821003 (project 4C). S. Bushinsky acknowledges funding from NASA Carbon Cycle Science (80NSSC22K0156), NOAA Climate Program Office's Climate Observations and Monitoring, Climate Variability and Predictability, and Global Ocean Monitoring and Observation programs (NA21OAR4310260), and NSF (OCE-2049631). S. Doney acknowledges support from the Palmer LTER program National Science Foundation Grant OPP-2026045. C. Le Quéré acknowledges support from the Natural Environment Research Council SONATA Grant NE/P021417/1 and the UK Royal Society Grant RP-R1-191063. J. Terhaar acknowledges funding from the Woods Hole Oceanographic Institution Postdoctoral Scholar Program, and the Swiss National Science Foundation under Grant 200020-20051. The work reflects only the authors' view; the European Commission and their executive agency are not responsible for any use that may be made of the information the work contains. Open Access funding enabled and organized by Projekt DEAL.

References

Armour, K. C., Marshall, J., Scott, J. R., Donohoe, A., & Newsom, E. R. (2016). Southern Ocean warming delayed by circumpolar upwelling and equatorward transport. *Nature Geoscience*, 9(7), 549–554. <https://doi.org/10.1038/geo2731>

Arndt, S., Janout, M., Biddle, L., Campbell, E., & Thomalla, S. (2022). The Weddell Sea and Dronning Maud Land (WSML) regional working group virtual science workshop, 14–16 june 2022 (Tech. Rep.). Zenodo. <https://doi.org/10.5281/ZENODO.6931424>

Arrigo, K. R., & van Dijken, G. L. (2007). Interannual variation in air-sea CO₂ flux in the Ross Sea, Antarctica: A model analysis. *Journal of Geophysical Research*, 112(C3), C03020. <https://doi.org/10.1029/2006JC003492>

Aumont, O., Ethé, C., Tagliabue, A., Bopp, L., & Gehlen, M. (2015). PISCES-v2: An ocean biogeochemical model for carbon and ecosystem studies. *Geoscientific Model Development*, 8(8), 2465–2513. <https://doi.org/10.5194/gmd-8-2465-2015>

Aumont, O., Orr, J. C., Monfray, P., Ludwig, W., Amiotte-Suchet, P., & Probst, J. L. (2001). Riverine-driven interhemispheric transport of carbon. *Global Biogeochemical Cycles*, 15(2), 393–405. <https://doi.org/10.1029/1999GB001238>

Ayers, J. M., & Strutton, P. G. (2013). Nutrient variability in subantarctic mode waters forced by the southern annular mode and ENSO. *Geophysical Research Letters*, 40(13), 3419–3423. <https://doi.org/10.1002/grl.50638>

Bakker, D., Alin, S. R., Becker, M., Bittig, H. C., Castaño-Primo, R., Feely, R. A., et al. (2022). *Surface ocean CO₂ atlas database version 2022 (SOCATv2022)*, NCEI accession 0253659. NOAA National Centers for Environmental Information. <https://doi.org/10.25921/1h9f-nb73>

Bakker, D., De Baar, H., & Bathmann, U. (1997). Changes of carbon dioxide in surface waters during spring in the Southern Ocean. *Deep Sea Research Part II: Topical Studies in Oceanography*, 44(1–2), 91–127. [https://doi.org/10.1016/S0967-0645\(96\)00075-6](https://doi.org/10.1016/S0967-0645(96)00075-6)

Bakker, D., Hoppema, M., Schröder, M., Geibert, W., & Baar, H. J. W. D. (2008). A rapid transition from ice covered CO₂-rich waters to a biologically mediated CO₂ sink in the eastern Weddell Gyre. *Biogeosciences*, 5, 1373–1386. <https://doi.org/10.5194/bg-5-1373-2008>

Bakker, D., Pfeil, B., Landa, C. S., Metzl, N., O'Brien, K. M., Olsen, A., et al. (2016). A multi-decade record of high-quality CO₂ data in version 3 of the Surface Ocean CO₂ Atlas (SOCAT). *Earth System Science Data*, 8(2), 383–413. <https://doi.org/10.5194/essd-8-383-2016>

Beadling, R. L., Russell, J. L., Stouffer, R. J., Mazloff, M., Talley, L. D., Goodman, P. J., et al. (2020). Representation of Southern Ocean properties across coupled model intercomparison project generations: CMIP3 to CMIP6. *Journal of Climate*, 33(15), 6555–6581. <https://doi.org/10.1175/JCLI-D-19-0970.1>

Berthet, S., Séférian, R., Bricaud, C., Chevallier, M., Volodire, A., & Ethé, C. (2019). Evaluation of an online grid-coarsening algorithm in a global eddy-admitting ocean biogeochemical model. *Journal of Advances in Modeling Earth Systems*, 11(6), 1759–1783. <https://doi.org/10.1029/2019MS001644>

Bopp, L., Lévy, M., Resplandy, L., & Sallée, J. B. (2015). Pathways of anthropogenic carbon subduction in the global ocean. *Geophysical Research Letters*, 42(15), 6416–6423. <https://doi.org/10.1002/2015GL065073>

Bourgeois, T., Goris, N., Schwinger, J., & Tjiputra, J. F. (2022). Stratification constrains future heat and carbon uptake in the Southern Ocean between 30°S and 55°S. *Nature Communications*, 13(1), 340. <https://doi.org/10.1038/s41467-022-27979-5>

Boyer, T. P., Garcia, H. E., Locarnini, R. A., Zweng, M. M., Mishonov, A. V., Reagan, J. R., et al. (2018). *World Ocean Atlas 2018*. NOAA National Centers for Environmental Information. Retrieved from <https://www.ncei.noaa.gov/archive/ accession/NCEI-WOA18>

Brown, M. S., Munro, D. R., Feehan, C. J., Sweeney, C., Ducklow, H. W., & Schofield, O. M. (2019). Enhanced oceanic CO₂ uptake along the rapidly changing West Antarctic Peninsula. *Nature Climate Change*, 9(9), 678–683. <https://doi.org/10.1038/s41558-019-0552-3>

Browning, T. J., Achterberg, E. P., Engel, A., & Mawji, E. (2021). Manganese co-limitation of phytoplankton growth and major nutrient drawdown in the Southern Ocean. *Nature Communications*, 12(1), 884. <https://doi.org/10.1038/s41467-021-21122-6>

Buitenhuis, E. T., Le Quéré, C., Bednaršek, N., & Schiebel, R. (2019). Large contribution of Pteropods to shallow CaCO₃ export. *Global Biogeochemical Cycles*, 33(3), 458–468. <https://doi.org/10.1029/2018GB006110>

Bushinsky, S. M., Takeshita, Y., & Williams, N. L. (2019). Observing changes in ocean carbonate chemistry: Our autonomous future. *Current Climate Change Reports*, 5(3), 207–220. <https://doi.org/10.1007/s40641-019-00129-8>

Caldeira, K., & Duffy, P. B. (2000). The role of the southern Ocean in uptake and storage of anthropogenic carbon dioxide. *Science*, 287(5453), 620–622. <https://doi.org/10.1126/science.287.5453.620>

Campin, J.-M., Hill, C., Jones, H., & Marshall, J. (2011). Super-parameterization in ocean modeling: Application to deep convection. *Ocean Modelling*, 36(1–2), 90–101. <https://doi.org/10.1016/j.ocemod.2010.10.003>

Canadell, J., Monteiro, P., Costa, M., Cotrim da Cunha, L., Cox, P., Eliseev, A., et al. (Eds.). (2021). Climate change 2021: The physical science basis. Contribution of working group I to the sixth assessment report of the intergovernmental panel on climate change (pp. 673–816). Cambridge University Press. <https://doi.org/10.1017/9781009157896.007>

Carroll, D., Menemenlis, D., Adkins, J. F., Bowman, K. W., Brix, H., Dutkiewicz, S., et al. (2020). The ECCO-Darwin data-assimilative Global Ocean Biogeochemistry model: Estimates of seasonal to multidecadal Surface Ocean pCO₂ and Air-Sea CO₂ flux. *Journal of Advances in Modeling Earth Systems*, 12(10), 1–28. <https://doi.org/10.1029/2019MS001888>

Carroll, D., Menemenlis, D., Dutkiewicz, S., Lauderdale, J. M., Adkins, J. F., Bowman, K. W., et al. (2022). Attribution of space-time variability in global-ocean dissolved inorganic carbon. *Global Biogeochemical Cycles*, 36(3), 1–24. <https://doi.org/10.1029/2021GB007162>

Carter, B. R., Bittig, H. C., Fassbender, A. J., Sharp, J. D., Takeshita, Y., Xu, Y.-Y., et al. (2021). New and updated global empirical seawater property estimation routines. *Limnology and Oceanography: Methods*, 19(12), 785–809. <https://doi.org/10.1002/lom3.10461>

Carter, B. R., Feely, R. A., Williams, N. L., Dickson, A. G., Fong, M. B., & Takeshita, Y. (2018). Updated methods for global locally interpolated estimation of alkalinity, pH, and nitrate. *Limnology and Oceanography: Methods*, 16(2), 119–131. <https://doi.org/10.1002/lom3.10232>

Carter, B. R., Williams, N. L., Gray, A. R., & Feely, R. A. (2016). Locally interpolated alkalinity regression for global alkalinity estimation. *Limnology and Oceanography: Methods*, 14(4), 268–277. <https://doi.org/10.1002/lom3.10087>

Chau, T. T. T., Gehlen, M., & Chevallier, F. (2022). A seamless ensemble-based reconstruction of surface ocean $p\text{CO}_2$ and air-sea CO_2 fluxes over the global coastal and open oceans. *Biogeosciences*, 19(4), 1087–1109. <https://doi.org/10.5194/bg-19-1087-2022>

Chevallier, F., Fisher, M., Peylin, P., Serran, S., Bousquet, P., Bréon, F. M., et al. (2005). Inferring CO_2 sources and sinks from satellite observations: Method and application to TOVS data. *Journal of Geophysical Research*, 110(24), 1–13. <https://doi.org/10.1029/2005JD006390>

Chien, C. T., Durgadoo, J. V., Ehlert, D., Frenger, I., Keller, D. P., Koeve, W., et al. (2022). FOCI-MOPS v1 - Integration of marine biogeochemistry within the Flexible Ocean and Climate Infrastructure version 1 (FOCI 1) Earth system model. *Geoscientific Model Development*, 15(15), 5987–6024. <https://doi.org/10.5194/gmd-15-5987-2022>

Clement, D., & Gruber, N. (2018). The eMLR(C*) method to determine decadal changes in the Global Ocean storage of anthropogenic CO_2 . *Global Biogeochemical Cycles*, 32(4), 654–679. <https://doi.org/10.1002/2017GB005819>

Crisp, D., Dolman, H., Tanhua, T., McKinley, G. A., Hauck, J., Bastos, A., et al. (2022). How well do we understand the land-ocean-atmosphere carbon cycle? *Reviews of Geophysics*, 60(2), 1–64. <https://doi.org/10.1029/2021RG000736>

De Baar, H. J. W., De Jong, J. T. M., Bakker, D. C. E., Löschner, B. M., Veth, C., Bathmann, U., & Smetacek, V. (1995). Importance of iron for plankton blooms and carbon dioxide drawdown in the Southern Ocean. *Nature*, 373(6513), 412–415. <https://doi.org/10.1038/373412a0>

Denvil-Sommer, A., Gehlen, M., & Vrac, M. (2021). Observation system simulation experiments in the Atlantic Ocean for enhanced surface ocean $p\text{CO}_2$ reconstructions. *Ocean Science*, 17(4), 1011–1030. <https://doi.org/10.5194/os-17-1011-2021>

DeVries, T. (2014). The oceanic anthropogenic CO_2 sink: Storage, air-sea fluxes, and transports over the industrial era. *Global Biogeochemical Cycles*, 28(7), 631–647. <https://doi.org/10.1002/2013GB004739>

DeVries, T. (2022). The ocean carbon cycle. *Annual Review of Environment and Resources*, 47(1), 317–341. <https://doi.org/10.1146/annurev-environ-120920-111307>

DeVries, T., Holzer, M., & Primeau, F. (2017). Recent increase in oceanic carbon uptake driven by weaker upper-ocean overturning. *Nature*, 542(7640), 215–218. <https://doi.org/10.1038/nature21068>

DeVries, T., Yamamoto, K., Wanninkhof, R., Gruber, N., Hauck, J., Müller, J. D., et al. (2023). Magnitude, trends, and variability of the global ocean carbon sink from 1985–2018. *Global Biogeochemical Cycles*, 37(10), e2023GB007780. <https://doi.org/10.1029/2023gb007780>

Djeutchaourang, L. M., Chang, N., Gregor, L., Vichi, M., & Monteiro, P. M. (2022). The sensitivity of $p\text{CO}_2$ reconstructions to sampling scales across a Southern Ocean sub-domain: A semi-idealized ocean sampling simulation approach. *Biogeosciences*, 19(17), 4171–4195. <https://doi.org/10.5194/bg-19-4171-2022>

Dlugokencky, E., Thoning, K., Lan, X., Tans, P., & Laboratory, N. G. M. (2021). NOAA greenhouse gas marine boundary layer reference - CO_2 . NOAA GML. <https://doi.org/10.15138/DVNP-F961>

Doney, S., Lima, I., Moore, J. K., Lindsay, K., Behrenfeld, M. J., Westberry, T. K., et al. (2009). Skill metrics for confronting global upper ocean ecosystem-biogeochemistry models against field and remote sensing data. *Journal of Marine Systems*, 76(1–2), 95–112. <https://doi.org/10.1016/j.jmarsys.2008.05.015>

Doney, S., Yeager, S., Danabasoglu, G., Large, W. G., & McWilliams, J. C. (2007). Mechanisms governing interannual variability of upper-ocean temperature in a global ocean hindcast simulation. *Journal of Physical Oceanography*, 37(7), 1918–1938. <https://doi.org/10.1175/JPO3089.1>

Döscher, R., Acosta, M., Alessandri, A., Anthomis, P., Arsouze, T., Bergman, T., et al. (2022). The EC-Earth3 Earth system model for the coupled model intercomparison project 6. *Geoscientific Model Development*, 15(7), 2973–3020. <https://doi.org/10.5194/gmd-15-2973-2022>

Drucker, R., & Riser, S. C. (2016). In situ phase-domain calibration of oxygen optodes on profiling floats. *Methods in Oceanography*, 17, 296–318. <https://doi.org/10.1016/j.mio.2016.09.007>

Ducklow, H. W., Stukel, M. R., Eveleth, R., Doney, S. C., Jickells, T., Schofield, O., et al. (2018). Spring-summer net community production, new production, particle export and related water column biogeochemical processes in the marginal sea ice zone of the Western Antarctic Peninsula 2012–2014. *Philosophical Transactions of the Royal Society A: Mathematical, Physical & Engineering Sciences*, 376(2122), 20170177. <https://doi.org/10.1098/rsta.2017.0177>

Dutkiewicz, S., Follows, M. J., & Bragg, J. G. (2009). Modeling the coupling of ocean ecology and biogeochemistry. *Global Biogeochemical Cycles*, 23(4), 1–15. <https://doi.org/10.1029/2008GB003405>

Easterling, D. R., & Wehner, M. F. (2009). Is the climate warming or cooling? *Geophysical Research Letters*, 36(8), L08706. <https://doi.org/10.1029/2009GL037810>

Eddebar, Y. A., Rodgers, K. B., Long, M. C., Subramanian, A. C., Xie, S.-P., & Keeling, R. F. (2019). El Niño-like physical and biogeochemical ocean response to tropical eruptions. *Journal of Climate*, 32(9), 2627–2649. <https://doi.org/10.1175/JCLI-D-18-0458.1>

Eveleth, R., Cassar, N., Doney, S. C., Munro, D. R., & Sweeney, C. (2017). Biological and physical controls on O_2/Ar , Ar and $p\text{CO}_2$ variability at the western Antarctic Peninsula and in the drake passage. *Deep-Sea Research Part II Topical Studies in Oceanography*, 139, 77–88. <https://doi.org/10.1016/j.dsr2.2016.05.002>

Fay, A. R., Gregor, L., Landschützer, P., McKinley, G. A., Gruber, N., Gehlen, M., et al. (2021). SeaFlux: Harmonization of air-sea CO_2 fluxes from surface $p\text{CO}_2$ data products using a standardized approach. *Earth System Science Data*, 13(10), 4693–4710. <https://doi.org/10.5194/essd-13-4693-2021>

Fay, A. R., & McKinley, G. A. (2013). Global trends in surface ocean $p\text{CO}_2$ from in situ data. *Global Biogeochemical Cycles*, 27(2), 541–557. <https://doi.org/10.1002/gbc.20051>

Fay, A. R., & McKinley, G. A. (2014). Global open-ocean biomes: Mean and temporal variability. *Earth System Science Data*, 6(2), 273–284. <https://doi.org/10.5194/essd-6-273-2014>

Fay, A. R., & McKinley, G. A. (2021). Observed regional fluxes to constrain modeled estimates of the Ocean Carbon sink. *Geophysical Research Letters*, 48(20), e2021GL095325. <https://doi.org/10.1029/2021GL095325>

Feng, L., Palmer, P. I., Parker, R. J., Deutscher, N. M., Feist, D. G., Kivi, R., et al. (2016). Estimates of European uptake of CO_2 inferred from GOSAT XCO_2 retrievals: Sensitivity to measurement bias inside and outside Europe. *Atmospheric Chemistry and Physics*, 16(3), 1289–1302. <https://doi.org/10.5194/acp-16-1289-2016>

Friedlingstein, P., O'Sullivan, M., Jones, M. W., Andrew, R. M., Gregor, L., Hauck, J., et al. (2022). Global carbon budget 2022. *Earth System Science Data*, 14(11), 4811–4900. <https://doi.org/10.5194/essd-14-4811-2022>

Frölicher, T. L., Sarmiento, J. L., Payne, D. J., Dunne, J. P., Krasting, J. P., & Winton, M. (2015). Dominance of the Southern Ocean in anthropogenic carbon and heat uptake in CMIP5 models. *Journal of Climate*, 28(2), 862–886. <https://doi.org/10.1175/JCLI-D-14-00117.1>

Galbraith, E. D., Gnanadesikan, A., Dunne, J. P., & Hiscock, M. R. (2010). Regional impacts of iron-light colimitation in a global biogeochemical model. *Biogeosciences*, 7(3), 1043–1064. <https://doi.org/10.5194/bg-7-1043-2010>

Gloegel, L., McKinley, G. A., Landschützer, P., Fay, A. R., Frölicher, T. L., Fyfe, J. C., et al. (2021). Quantifying errors in observationally based estimates of Ocean Carbon sink variability. *Global Biogeochemical Cycles*, 35(4), 1–14. <https://doi.org/10.1029/2020GB006788>

Gloegel, L., Yan, M., Zheng, T., & McKinley, G. A. (2022). Improved quantification of Ocean Carbon uptake by using machine learning to merge global models and pCO₂ data. *Journal of Advances in Modeling Earth Systems*, 14(2), 1–19. <https://doi.org/10.1029/2021MS002620>

Good, S. A., Martin, M. J., & Rayner, N. A. (2013). EN4: Quality controlled ocean temperature and salinity profiles and monthly objective analyses with uncertainty estimates. *Journal of Geophysical Research: Oceans*, 118(12), 6704–6716. <https://doi.org/10.1002/2013JC009067>

Gray, A. R., Johnson, K. S., Bushinsky, S. M., Riser, S. C., Russell, J. L., Talley, L. D., et al. (2018). Autonomous biogeochemical floats detect significant carbon dioxide outgassing in the high-latitude Southern Ocean. *Geophysical Research Letters*, 45(17), 9049–9057. <https://doi.org/10.1029/2018GL078013>

Gregor, L., & Gruber, N. (2021). OceanSODA-ETHZ: A global gridded data set of the surface ocean carbonate system for seasonal to decadal studies of ocean acidification. *Earth System Science Data*, 13(2), 777–808. <https://doi.org/10.5194/essd-13-777-2021>

Gregor, L., Kok, S., & Monteiro, P. M. S. (2017). Empirical methods for the estimation of southern Ocean CO₂: Support vector and random forest regression. *Biogeosciences*, 14(23), 5551–5569. <https://doi.org/10.5194/bg-14-5551-2017>

Gregor, L., Lebehot, A. D., Kok, S., & Scheel Monteiro, P. M. (2019). A comparative assessment of the uncertainties of global surface ocean CO₂ estimates using a machine-learning ensemble (CSIR-ML6 version 2019a) - Have we hit the wall? *Geoscientific Model Development*, 12(12), 5113–5136. <https://doi.org/10.5194/gmd-12-5113-2019>

Gruber, N., Bakker, D. C. E., DeVries, T., Gregor, L., Hauck, J., Landschützer, P., et al. (2023). Trends and variability in the ocean carbon sink. *Nature Reviews Earth & Environment*, 4(2), 119–134. <https://doi.org/10.1038/s43017-022-00381-x>

Gruber, N., Clement, D., Carter, B. R., Feely, R. A., van Heuven, S., Hoppema, M., et al. (2019). The oceanic sink for anthropogenic CO₂ from 1994 to 2007. *Science*, 363(6432), 1193–1199. <https://doi.org/10.1126/science.aau5153>

Gruber, N., Gloo, M., Mikaloff Fletcher, S. E., Doney, S. C., Dutkiewicz, S., Follows, M. J., et al. (2009). Oceanic sources, sinks, and transport of atmospheric CO₂. *Global Biogeochemical Cycles*, 23(1), GB1005. <https://doi.org/10.1029/2008GB003349>

Gruber, N., Landschützer, P., & Lovenduski, N. S. (2019). The variable southern Ocean Carbon sink. *Annual Review of Marine Science*, 11(1), 159–186. <https://doi.org/10.1146/annurev-marine-121916-063407>

Gruber, N., Sarmiento, J. L., & Stocker, T. F. (1996). An improved method for detecting anthropogenic CO₂ in the oceans. *Global Biogeochemical Cycles*, 10(4), 809–837. <https://doi.org/10.1029/96GB01608>

Hauck, J., Gregor, L., Nissen, C., Patara, L., Hague, M., Mongwe, P., et al. (2023a). The Southern Ocean carbon cycle 1985–2018: Mean, seasonal cycle, trends and storage - Data [Dataset]. Zenodo. <https://zenodo.org/records/10074671>

Hauck, J., Gregor, L., Nissen, C., Patara, L., Hague, M., Mongwe, P., et al. (2023b). The Southern Ocean carbon cycle 1985–2018: Mean, seasonal cycle, trends and storage - Scripts [Dataset]. Zenodo. <https://zenodo.org/records/10076121>

Hauck, J., Nissen, C., Landschützer, P., Rödenbeck, C., Bushinsky, S., & Olsen, A. (2023). Sparse observations induce large biases in estimates of the global ocean CO₂ sink: An ocean model subsampling experiment. *Philosophical Transactions of the Royal Society A: Mathematical, Physical & Engineering Sciences*, 381(2249), 20220063. <https://doi.org/10.1098/rsta.2022.0063>

Hauck, J., Völker, C., Wang, T., Hoppema, M., Losch, M., & Wolf-Gladrow, D. A. (2013). Seasonally different carbon flux changes in the Southern Ocean in response to the southern annular mode. *Global Biogeochemical Cycles*, 27(4), 1236–1245. <https://doi.org/10.1002/2013GB004600>

Hauck, J., Völker, C., Wolf-Gladrow, D. A., Laufkötter, C., Vogt, M., Aumont, O., et al. (2015). On the Southern Ocean CO₂ uptake and the role of the biological carbon pump in the 21st century. *Global Biogeochemical Cycles*, 29(9), 1451–1470. <https://doi.org/10.1002/2015GB005140>

Hauck, J., Zeising, M., Le Quéré, C., Gruber, N., Bakker, D. C. E., Bopp, L., et al. (2020). Consistency and challenges in the Ocean Carbon sink estimate for the global carbon budget. *Frontiers in Marine Science*, 7, 571720. <https://doi.org/10.3389/fmars.2020.571720>

Haumann, A. (2016). Southern ocean response to recent changes in surface freshwater fluxes (Doctoral dissertation). <https://doi.org/10.3929/ETHZ-B-000166276>

Haumann, F., Gruber, N., & Münnich, M. (2020). Sea-ice induced Southern Ocean subsurface warming and surface cooling in a warming climate. *AGU Advances*, 1(2), e2019AV000132. <https://doi.org/10.1029/2019av000132>

Hauri, C., Doney, S. C., Takahashi, T., Erickson, M., Jiang, G., & Ducklow, H. (2015). Two decades of inorganic carbon dynamics along the West Antarctic Peninsula. *Biogeosciences*, 12(22), 6761–6779. <https://doi.org/10.5194/bg-12-6761-2015>

Holzer, M., & DeVries, T. (2022). Source-labeled anthropogenic carbon reveals a large shift of preindustrial carbon from the Ocean to the atmosphere. *Global Biogeochemical Cycles*, 36(10), e2022GB007405. <https://doi.org/10.1029/2022GB007405>

Hoppema, M. (2004). Weddell Sea turned from source to sink for atmospheric CO₂ between pre-industrial time and present. *Global and Planetary Change*, 40(3–4), 219–231. <https://doi.org/10.1016/j.gloplacha.2003.08.001>

Hoppema, M., Bakker, K., van Heuven, S. M., van Ooijen, J. C., & de Baar, H. J. (2015). Distributions, trends and inter-annual variability of nutrients along a repeat section through the Weddell Sea (1996–2011). *Marine Chemistry*, 177, 545–553. <https://doi.org/10.1016/j.marchem.2015.08.007>

Hoppema, M., Fahrbach, E., Schröder, M., Wisotzki, A., & De Baar, H. J. (1995). Winter–summer differences of carbon dioxide and oxygen in the Weddell Sea surface layer. *Marine Chemistry*, 51(3), 177–192. [https://doi.org/10.1016/0304-4203\(95\)00065-8](https://doi.org/10.1016/0304-4203(95)00065-8)

Hoppema, M., Fahrbach, E., Stoll, M. H., & de Baar, H. J. (1998). Increase of carbon dioxide in the bottom water of the Weddell Sea, Antarctica. *Marine Chemistry*, 59(3–4), 201–210. [https://doi.org/10.1016/S0304-4203\(97\)00094-7](https://doi.org/10.1016/S0304-4203(97)00094-7)

Hoppema, M., Fahrbach, E., Stoll, M. H., & De Baar, H. J. (1999). Annual uptake of atmospheric CO₂ by the Weddell Sea derived from a surface layer balance, including estimations of entrainment and new production. *Journal of Marine Systems*, 19(4), 219–233. [https://doi.org/10.1016/S0924-7963\(98\)00091-8](https://doi.org/10.1016/S0924-7963(98)00091-8)

Huang, B., Thorne, P. W., Banzon, V. F., Boyer, T. P., Chepurin, G., Lawrimore, J. H., et al. (2017). NOAA Extended Reconstructed Sea Surface temperature (ERSST), version 5. NOAA National Centers for Environmental Information. <https://doi.org/10.7289/V5T72FNM>

Iida, T., Odate, T., & Fukuchi, M. (2013). Long-term trends of nutrients and apparent oxygen utilization south of the polar front in Southern Ocean intermediate water from 1965 to 2008. *PLoS One*, 8(8), e71766. <https://doi.org/10.1371/journal.pone.0071766>

Iida, Y., Takatani, Y., Kojima, A., & Ishii, M. (2021). Global trends of ocean CO₂ sink and ocean acidification: An observation-based reconstruction of surface ocean inorganic carbon variables. *Journal of Oceanography*, 77(2), 323–358. <https://doi.org/10.1007/s10872-020-00571-5>

Ilyina, T., Six, K. D., Segschneider, J., Maier-Reimer, E., Li, H., & Núñez-Riboni, I. (2013). Global ocean biogeochemistry model HAMOCC: Model architecture and performance as component of the MPI-Earth system model in different CMIP5 experimental realizations. *Journal of Advances in Modeling Earth Systems*, 5(2), 287–315. <https://doi.org/10.1029/2012MS000178>

Ito, T., Woloszyn, M., & Mazloff, M. (2010). Anthropogenic carbon dioxide transport in the Southern Ocean driven by Ekman flow. *Nature*, 463(7277), 80–83. <https://doi.org/10.1038/nature08687>

Judicone, D., Rodgers, K. B., Plancherel, Y., Aumont, O., Ito, T., Key, R. M., et al. (2016). The formation of the ocean's anthropogenic carbon reservoir. *Scientific Reports*, 6(1), 35473. <https://doi.org/10.1038/srep35473>

Jacobs, S. S. (2004). Bottom water production and its links with the thermohaline circulation. *Antarctic Science*, 16(4), 427–437. <https://doi.org/10.1017/S095410200400224X>

Johnson, K. S., Plant, J. N., Coletti, L. J., Jannasch, H. W., Sakamoto, C. M., Riser, S. C., et al. (2017). Biogeochemical sensor performance in the SOCCOM profiling float array. *Journal of Geophysical Research: Oceans*, 122(8), 6416–6436. <https://doi.org/10.1002/2017JC012838>

Jones, D. C., Meijers, A. J. S., Shuckburgh, E., Sallée, J.-B., Haynes, P., McAuliffe, E. K., & Mazloff, M. R. (2016). How does subantarctic mode water ventilate the southern hemisphere subtropics? *Journal of Geophysical Research: Oceans*, 121(9), 6558–6582. <https://doi.org/10.1002/2016JC011680>

Jones, E., Bakker, D. C., Venables, H. J., & Hardman-Mountford, N. J. (2015). Seasonal cycle of CO₂ from the sea ice edge to island blooms in the Scotia Sea, Southern Ocean. *Marine Chemistry*, 177, 490–500. <https://doi.org/10.1016/j.marchem.2015.06.031>

Jones, E., Bakker, D. C., Venables, H. J., & Watson, A. J. (2012). Dynamic seasonal cycling of inorganic carbon downstream of South Georgia, Southern Ocean. *Deep Sea Research Part II: Topical Studies in Oceanography*, 59–60, 25–35. <https://doi.org/10.1016/j.dsrr.2011.08.001>

Katavouta, A., & Williams, R. G. (2021). Ocean carbon cycle feedbacks in CMIP6 models: Contributions from different basins. *Biogeosciences*, 18(10), 3189–3218. <https://doi.org/10.5194/bg-18-3189-2021>

Keppler, L., & Landschützer, P. (2019). Regional wind variability modulates the southern Ocean Carbon sink. *Scientific Reports*, 9(1), 7384. <https://doi.org/10.1038/s41598-019-43826-y>

Kessler, A., & Tjiputra, J. (2016). The Southern Ocean as a constraint to reduce uncertainty in future ocean carbon sinks. *Earth System Dynamics*, 7(2), 295–312. <https://doi.org/10.5194/esd-7-295-2016>

Khatiwala, S., Primeau, F., & Hall, T. (2009). Reconstruction of the history of anthropogenic CO₂ concentrations in the ocean. *Nature*, 462(7271), 346–349. <https://doi.org/10.1038/nature08526>

Klatt, O., Fahrbach, E., Hoppe, M., & Rohardt, G. (2005). The transport of the weddell gyre across the prime meridian. *Deep Sea Research Part II: Topical Studies in Oceanography*, 52(3), 513–528. <https://doi.org/10.1016/j.dsrr.2004.12.015>

Kriest, I., & Oschlies, A. (2015). MOPS-1.0: Towards a model for the regulation of the global oceanic nitrogen budget by marine biogeochemical processes. *Geoscientific Model Development*, 8(9), 2929–2957. <https://doi.org/10.5194/gmd-8-2929-2015>

Lacroix, F., Ilyina, T., & Hartmann, J. (2020). Oceanic CO₂ outgassing and biological production hotspots induced by pre-industrial river loads of nutrients and carbon in a global modeling approach. *Biogeosciences*, 17(1), 55–88. <https://doi.org/10.5194/bg-17-55-2020>

Landschützer, P., Gruber, N., & Bakker, D. C. (2016). Decadal variations and trends of the global ocean carbon sink. *Global Biogeochemical Cycles*, 30(10), 1396–1417. <https://doi.org/10.1002/2015GB005359>

Landschützer, P., Gruber, N., & Bakker, D. C. E. (2020). An observation-based global monthly gridded sea surface pCO₂ product from 1982 onward and its monthly climatology (NCEI Accession 0160558) (Tech. Rep.). Retrieved from [https://www.ncei.noaa.gov/access/ocean-carbon-acidification-data-system/oceans/SPCO2\(_1982\(_present\(_\)ETH\(_\)SOM\(_\)FFN.html](https://www.ncei.noaa.gov/access/ocean-carbon-acidification-data-system/oceans/SPCO2(_1982(_present(_)ETH(_)SOM(_)FFN.html)

Landschützer, P., Gruber, N., Bakker, D. C. E., & Schuster, U. (2014). Recent variability of the global ocean carbon sink. *Global Biogeochemical Cycles*, 28(9), 927–949. <https://doi.org/10.1002/2014GB004853>

Landschützer, P., Gruber, N., Haumann, F. A., Rödenbeck, C., Bakker, D. C. E., van Heuven, S., et al. (2015). The reinvigoration of the Southern Ocean carbon sink. *Science*, 349(6253), 1221–1224. <https://doi.org/10.1126/science.aab2620>

Langlais, C. E., Lenton, A., Matear, R., Monselesan, D., Legresy, B., Cugnon, E., & Rintoul, S. (2017). Stationary Rossby waves dominate subduction of anthropogenic carbon in the Southern Ocean. *Scientific Reports*, 7(1), 17076. <https://doi.org/10.1038/s41598-017-1729-3>

Large, W. G., McWilliams, J. C., & Doney, S. C. (1994). Oceanic vertical mixing - A review and a model with a nonlocal boundary-layer parameterization. *Reviews of Geophysics*, 32(94), 363–403. <https://doi.org/10.1029/94rg01872>

Lauderdale, J. M., Dutkiewicz, S., Williams, R. G., & Follows, M. J. (2016). Quantifying the drivers of ocean-atmosphere CO₂ fluxes. *Global Biogeochemical Cycles*, 30(7), 983–999. <https://doi.org/10.1002/2016GB005400>

Lenton, A., & Matear, R. J. (2007). Role of the southern annular mode (SAM) in southern Ocean CO₂ uptake. *Global Biogeochemical Cycles*, 21(2), 1–17. <https://doi.org/10.1029/2006GB002714>

Lenton, A., Tilbrook, B., Law, R. M., Bakker, D., Doney, S. C., Gruber, N., et al. (2013). Sea-Air CO₂ fluxes in the Southern Ocean for the period 1990–2009. *Biogeosciences*, 10(6), 4037–4054. <https://doi.org/10.5194/bg-10-4037-2013>

Le Quéré, C., Andrew, R. M., Friedlingstein, P., Sitch, S., Hauck, J., Pongratz, J., et al. (2018). Global carbon budget 2018. *Earth System Science Data*, 10(4), 2141–2194. <https://doi.org/10.5194/essd-10-2141-2018>

Le Quéré, C., Buitenhuis, E. T., Moriarty, R., Alvain, S., Aumont, O., Bopp, L., et al. (2016). Role of zooplankton dynamics for Southern Ocean phytoplankton biomass and global biogeochemical cycles. *Biogeosciences*, 13(14), 4111–4133. <https://doi.org/10.5194/bg-13-4111-2016>

Le Quéré, C., Rödenbeck, C., Buitenhuis, E. T., Conway, T. J., Langenfelds, R., Gomez, A., et al. (2007). Saturation of the Southern Ocean CO₂ sink due to recent climate change. *Science*, 316(5832), 1735–1738. <https://doi.org/10.1126/science.1136188>

Le Quéré, C., Takahashi, T. T., Buitenhuis, E. T., Rödenbeck, C., & Sutherland, S. C. (2010). Impact of climate change and variability on the global oceanic sink of CO₂. *Global Biogeochemical Cycles*, 24(4), 1–10. <https://doi.org/10.1029/2009GB003599>

Liao, E., Resplandy, L., Liu, J., & Bowman, K. W. (2020). Amplification of the Ocean Carbon sink during El Niños: Role of Poleward Ekman transport and influence on atmospheric CO₂. *Global Biogeochemical Cycles*, 34(9), 1–23. <https://doi.org/10.1029/2020GB006574>

Lindsay, K., Bonan, G. B., Doney, S. C., Hoffman, F. M., Lawrence, D. M., Long, M. C., et al. (2014). Preindustrial-control and twentieth-century carbon cycle experiments with the Earth system model CESM1(BGC). *Journal of Climate*, 27(24), 8981–9005. <https://doi.org/10.1175/JCLI-D-12-00565.1>

Liu, J., Baskaran, L., Bowman, K., Schimel, D., Anthony Bloom, A., Parazoo, C. N., et al. (2021). Carbon monitoring system flux net biosphere exchange 2020 (CMS-Flux NBE 2020). *Earth System Science Data*, 13(2), 299–330. <https://doi.org/10.5194/essd-13-299-2021>

Long, M. C., Stephens, B. B., McKain, K., Sweeney, C., Keeling, R. F., Kort, E. A., et al. (2021). Strong Southern Ocean carbon uptake evident in airborne observations. *Science*, 374(6572), 1275–1280. <https://doi.org/10.1126/science.abi4355>

Lovenduski, N. S., Gruber, N., Doney, S. C., & Lima, I. D. (2007). Enhanced CO₂ outgassing in the Southern Ocean from a positive phase of the southern annular mode. *Global Biogeochemical Cycles*, 21(2), GB2026. <https://doi.org/10.1029/2006GB002900>

Madec, G., & the NEMO team. (2016). *NEMO reference manual 3_6_STABLE: "NEMO ocean engine" note du Pôle de modélisation*. Institut Pierre-Simon Laplace (IPSL).

Marshall, J., & Speer, K. (2012). Closure of the meridional overturning circulation through Southern Ocean upwelling. *Nature Geoscience*, 5(3), 171–180. <https://doi.org/10.1038/ngeo1391>

Matsumoto, K., & Gruber, N. (2005). How accurate is the estimation of anthropogenic carbon in the ocean? An evaluation of the ΔC* method. *Global Biogeochemical Cycles*, 19(3), GB3014. <https://doi.org/10.1029/2004GB002397>

Mauritsen, T., Bader, J., Becker, T., Behrens, J., Bittner, M., Brokopf, R., et al. (2019). Developments in the MPI-M Earth system model version 1.2 (MPI-ESM1.2) and its response to increasing CO₂. *Journal of Advances in Modeling Earth Systems*, 11(4), 998–1038. <https://doi.org/10.1029/2018MS001400>

Mayot, N., Le Quéré, C., Rödenbeck, C., Bernardello, R., Bopp, L., Djedchouang, L. M., et al. (2023). Climate-driven variability of the southern Ocean CO₂ sink. *Philosophical Transactions of the Royal Society A: Mathematical, Physical & Engineering Sciences*, 381(2249), 20220055. <https://doi.org/10.1098/rsta.2022.0055>

McKinley, G. A., Fay, A. R., Eddebar, Y. A., Gloege, L., & Lovenduski, N. S. (2020). External forcing explains recent decadal variability of the Ocean Carbon sink. *AGU Advances*, 1(2), e2019AV000149. <https://doi.org/10.1029/2019AV000149>

McNeil, B. I., & Matear, R. J. (2013). The non-steady state oceanic CO₂ signal: Its importance, magnitude and a novel way to detect it. *Biogeoosciences*, 10(4), 2219–2228. <https://doi.org/10.5194/bg-10-2219-2013>

Metzl, N., Brunet, C., Jabaud-Jan, A., Poisson, A., & Schauer, B. (2006). Summer and winter air-sea CO₂ fluxes in the Southern Ocean. *Deep-Sea Research Part I Oceanographic Research Papers*, 53(9), 1548–1563. <https://doi.org/10.1016/j.dsri.2006.07.006>

Metzl, N., Tilbrook, B., & Poisson, A. (1999). The annual fCO₂ cycle and the air-sea CO₂ flux in the sub-Antarctic Ocean. *Tellus B: Chemical and Physical Meteorology*, 51(4), 849. <https://doi.org/10.3402/tellusb.v51i4.16495>

Mikaloff Fletcher, S. E., Gruber, N., Jacobson, A. R., Doney, S. C., Dutkiewicz, S., Gerber, M., et al. (2006). Inverse estimates of anthropogenic CO₂ uptake, transport, and storage by the ocean. *Global Biogeochemical Cycles*, 20(2), GB2002. <https://doi.org/10.1029/2005GB002530>

Mikaloff Fletcher, S. E., Gruber, N., Jacobson, A. R., Gloor, M., Doney, S. C., Dutkiewicz, S., et al. (2007). Inverse estimates of the oceanic sources and sinks of natural CO₂ and the implied oceanic carbon transport. *Global Biogeochemical Cycles*, 21(1), GB1010. <https://doi.org/10.1029/2006GB002751>

Mongwe, N. P., Chang, N., & Monteiro, P. M. S. (2016). The seasonal cycle as a mode to diagnose biases in modelled CO₂ fluxes in the Southern Ocean. *Ocean Modelling*, 106, 90–103. <https://doi.org/10.1016/j.ocemod.2016.09.006>

Mongwe, N. P., Vichi, M., & Monteiro, P. M. S. (2018). The seasonal cycle of pCO₂ and CO₂ fluxes in the Southern Ocean: Diagnosing anomalies in CMIP5 Earth system models. *Biogeosciences*, 15(9), 2851–2872. <https://doi.org/10.5194/bg-15-2851-2018>

Morrison, A. K., Waugh, D. W., Hogg, A. M., Jones, D. C., & Abernathey, R. P. (2022). Ventilation of the Southern Ocean Pycnocline. *Annual Review of Marine Science*, 14(1), 405–430. <https://doi.org/10.1146/annurev-marine-010419-011012>

Müller, J. D. (2023). RECCAP2-ocean data collection [Dataset]. Zenodo. <https://doi.org/10.5281/zenodo.7990823>

Murnane, R. J., Sarmiento, J. L., & Le Quéré, C. (1999). Spatial distribution of air-sea CO₂ fluxes and the interhemispheric transport of carbon by the oceans. *Global Biogeochemical Cycles*, 13(2), 287–305. <https://doi.org/10.1029/1998GB900009>

Nevison, C. D., Munro, D. R., Lovenduski, N. S., Keeling, R. F., Manizza, M., Morgan, E. J., & Rödenbeck, C. (2020). Southern annular mode influence on wintertime ventilation of the Southern Ocean detected in atmospheric O₂ and CO₂ measurements. *Geophysical Research Letters*, 47(4), 1–9. <https://doi.org/10.1029/2019GL085667>

Nicholson, S. A., Whitt, D. B., Fer, I., du Plessis, M. D., Lebéhot, A. D., Swart, S., et al. (2022). Storms drive outgassing of CO₂ in the subpolar Southern Ocean. *Nature Communications*, 13(1), 1–12. <https://doi.org/10.1038/s41467-021-27780-w>

Nissen, C., Vogt, M., Münnich, M., Gruber, N., & Alexander Haumann, F. (2018). Factors controlling coccolithophore biogeography in the Southern Ocean. *Biogeosciences*, 15(22), 6997–7024. <https://doi.org/10.5194/bg-15-6997-2018>

Niwa, Y., Fujii, Y., Sawa, Y., Iida, Y., Ito, A., Satoh, M., et al. (2017). A 4D-Var inversion system based on the icosahedral grid model (NICAM-TM 4D-Var v1.0) - Part 2: Optimization scheme and identical twin experiment of atmospheric CO₂ inversion. *Geoscientific Model Development*, 10(6), 2201–2219. <https://doi.org/10.5194/gmd-10-2201-2017>

Olsen, A., Key, R. M., van Heuven, S., Lauvset, S. K., Velo, A., Lin, X., et al. (2016). The Global Ocean Data Analysis Project version 2 (GLODAPv2) - An internally consistent data product for the world ocean. *Earth System Science Data*, 8(2), 297–323. <https://doi.org/10.5194/essd-8-297-2016>

Orr, J. C., Maier-Reimer, E., Mikolajewicz, U., Monfray, P., Sarmiento, J. L., Toggweiler, J. R., et al. (2001). Estimates of anthropogenic carbon uptake from four three-dimensional global ocean models. *Global Biogeochemical Cycles*, 15(1), 43–60. <https://doi.org/10.1029/2000GB001273>

Orsi, A., Johnson, G., & Bullister, J. (1999). Circulation, mixing, and production of Antarctic bottom water. *Progress in Oceanography*, 43(1), 55–109. [https://doi.org/10.1016/S0079-6611\(99\)00004-X](https://doi.org/10.1016/S0079-6611(99)00004-X)

Panassa, E., Santana-Casiano, J. M., González-Dávila, M., Hoppema, M., van Heuven, S. M., Völker, C., et al. (2018). Variability of nutrients and carbon dioxide in the Antarctic intermediate water between 1990 and 2014. *Ocean Dynamics*, 68(3), 295–308. <https://doi.org/10.1007/s10236-018-1131-2>

Pardo, P. C., Tilbrook, B., Langlais, C., Trull, T. W., & Rintoul, S. R. (2017). Carbon uptake and biogeochemical change in the Southern Ocean, south of Tasmania. *Biogeosciences*, 14(22), 5217–5237. <https://doi.org/10.5194/bg-14-5217-2017>

Paulsen, H., Ilyina, T., Six, K. D., & Stemmler, I. (2017). Incorporating a prognostic representation of marine nitrogen fixers into the global ocean biogeochemical model HAMOCC. *Journal of Advances in Modeling Earth Systems*, 9(1), 438–464. <https://doi.org/10.1002/2016MS000737>

Prend, C. J., Keerthi, M. G., Lévy, M., Aumont, O., Gille, S. T., & Talley, L. D. (2022). Sub-seasonal forcing drives year-to-year variations of Southern Ocean primary productivity. *Global Biogeochemical Cycles*, 36(7), 1–15. <https://doi.org/10.1029/2022GB007329>

Regnier, P. A., Resplandy, L., Najjar, R. G., & Cai, P. (2022). The land-to-ocean loops of the global carbon cycle. *Nature*, 603(7901), 401–410. <https://doi.org/10.1038/s41586-021-04339-9>

Rintoul, S. R. (2018). The global influence of localized dynamics in the Southern Ocean. *Nature*, 558(7709), 209–218. <https://doi.org/10.1038/s41586-018-0182-3>

Riser, S. C., Swift, D., & Drucker, R. (2018). Profiling floats in SOCCOM: Technical capabilities for studying the Southern Ocean. *Journal of Geophysical Research: Oceans*, 123(6), 4055–4073. <https://doi.org/10.1002/2017JC013419>

Ritter, R., Landschützer, P., Gruber, N., Fay, A. R., Iida, Y., Jones, S. D., et al. (2017). Observation-based trends of the southern Ocean Carbon sink. *Geophysical Research Letters*, 44(24), 12339–12348. <https://doi.org/10.1002/2017GL074837>

Rödenbeck, C., Bakker, D. C., Gruber, N., Iida, Y., Jacobson, A. R., Jones, S. D., et al. (2015). Data-based estimates of the ocean carbon sink variability - First results of the Surface Ocean pCO₂ Mapping intercomparison (SOCOM). *Biogeosciences*, 12(23), 7251–7278. <https://doi.org/10.5194/bg-12-7251-2015>

Rödenbeck, C., Bakker, D. C., Metzl, N., Olsen, A., Sabine, C. L., Cassar, N., et al. (2014). Interannual sea-air CO₂ flux variability from an observation-driven ocean mixed-layer scheme. *Biogeosciences*, 11(17), 4599–4613. <https://doi.org/10.5194/bg-11-4599-2014>

Rödenbeck, C., Devries, T., Hauck, J., Le Quéré, C., & Keeling, R. F. (2022). Data-based estimates of interannual sea-air CO₂ flux variations 1957–2020 and their relation to environmental drivers. *Biogeosciences*, 19(10), 2627–2652. <https://doi.org/10.5194/bg-19-2627-2022>

Rödenbeck, C., Keeling, R. F., Bakker, D. C., Metzl, N., Olsen, A., Sabine, C. L., & Heimann, M. (2013). Global surface-ocean pCO₂ and sea-air CO₂ flux variability from an observation-driven ocean mixed-layer scheme. *Ocean Science*, 9(2), 193–216. <https://doi.org/10.5194/os-9-193-2013>

Rödenbeck, C., Zaehle, S., Keeling, R., & Heimann, M. (2018). How does the terrestrial carbon exchange respond to inter-annual climatic variations? A quantification based on atmospheric CO₂ data. *Biogeosciences*, 15(8), 2481–2498. <https://doi.org/10.5194/bg-15-2481-2018>

Russell, J. L., Dixon, K. W., Gnanadesikan, A., Stouffer, R. J., & Toggweiler, J. R. (2006). The southern hemisphere westerlies in a warming world: Propping open the door to the deep ocean. *Journal of Climate*, 19(24), 6382–6390. <https://doi.org/10.1175/JCLI3984.1>

Ryan-Keogh, T. J., Thomalla, S. J., Monteiro, P. M. S., & Tagliabue, A. (2023). Multidecadal trend of increasing iron stress in Southern Ocean phytoplankton. *Science*, 379(6634), 834–840. <https://doi.org/10.1126/science.abl5237>

Sabine, C. L., Feely, R. A., Gruber, N., Key, R. M., Lee, K., Bullister, J. L., et al. (2004). The oceanic sink for anthropogenic CO₂. *Science*, 305(5682), 367–371. <https://doi.org/10.1126/science.1097403>

Sabine, C. L., Hankin, S., Koyuk, H., Bakker, D. C., Pfeil, B., Olsen, A., et al. (2013). Surface Ocean CO₂ Atlas (SOCAT) gridded data products. *Earth System Science Data*, 5(1), 145–153. <https://doi.org/10.5194/essd-5-145-2013>

Sallée, J.-B., Matear, R. J., Rintoul, S. R., & Lenton, A. (2012). Localized subduction of anthropogenic carbon dioxide in the southern hemisphere oceans. *Nature Geoscience*, 5(8), 579–584. <https://doi.org/10.1038/ngeo1523>

Sallée, J.-B., Speer, K., & Rintoul, S. R. (2010). Zonally asymmetric response of the Southern Ocean mixed-layer depth to the southern annular mode. *Nature Geoscience*, 3(4), 273–279. <https://doi.org/10.1038/ngeo812>

Sarmiento, J. L., & Gruber, N. (2006). *Ocean biogeochemical dynamics*. Princeton University Press.

Sarmiento, J. L., Orr, J. C., & Siegenthaler, U. (1992). A perturbation simulation of CO₂ uptake in an ocean general circulation model. *Journal of Geophysical Research*, 97(C3), 3621–3645. <https://doi.org/10.1029/91JC02849>

Schourop-Kristensen, V., Sidorenko, D., Wolf-Gladrow, D. A., & Völker, C. (2014). A skill assessment of the biogeochemical model REcoM2 coupled to the finite element sea ice-ocean model (FESOM 1.3). *Geoscientific Model Development*, 7(6), 2769–2802. <https://doi.org/10.5194/gmd-7-2769-2014>

Schourop-Kristensen, V., Wekerle, C., Wolf-Gladrow, D. A., & Völker, C. (2018). Arctic Ocean biogeochemistry in the high resolution FESOM1.4-REcoM2 model. *Progress in Oceanography*, 168(August), 65–81. <https://doi.org/10.1016/j.pocean.2018.09.006>

Schultz, C., Doney, S. C., Hauck, J., Kavanaugh, M. T., & Schofield, O. (2021). Modeling phytoplankton blooms and inorganic carbon responses to sea-ice variability in the west Antarctic Peninsula. *Journal of Geophysical Research: Biogeosciences*, 126(4), 1–21. <https://doi.org/10.1029/2020JG006227>

Schwinger, J., Goris, N., Tjiputra, J. F., Kriest, I., Bentsen, M., Bethke, I., et al. (2016). Evaluation of NorESM-OC (versions 1 and 1.2), the ocean carbon-cycle stand-alone configuration of the Norwegian Earth system model (NorESM1). *Geoscientific Model Development*, 9(8), 2589–2622. <https://doi.org/10.5194/gmd-9-2589-2016>

Séférian, R., Berthet, S., Yool, A., Palmiéri, J., Bopp, L., Tagliabue, A., et al. (2020). Tracking improvement in simulated marine biogeochemistry between CMIP5 and CMIP6. *Current Climate Change Reports*, 6(3), 95–119. <https://doi.org/10.1007/s40641-020-00160-0>

Séférian, R., Gehlen, M., Bopp, L., Resplandy, L., Orr, J. C., Marti, O., et al. (2016). Inconsistent strategies to spin up models in CMIP5: Implications for ocean biogeochemical model performance assessment. *Geoscientific Model Development*, 9(5), 1827–1851. <https://doi.org/10.5194/gmd-9-1827-2016>

Séférian, R., Nabat, P., Michou, M., Saint-Martin, D., Volodire, A., Colin, J., et al. (2019). Evaluation of CNRM Earth system model, CNRM-ESM2-1: Role of Earth system processes in present-day and future climate. *Journal of Advances in Modeling Earth Systems*, 11(12), 4182–4227. <https://doi.org/10.1029/2019MS001791>

Shadwick, E. H., De Meo, O. A., Schroeter, S., Arroyo, M. C., Martinson, D. G., & Ducklow, H. (2021). Sea ice suppression of CO₂ outgassing in the west Antarctic Peninsula: Implications for the evolving southern Ocean Carbon sink. *Geophysical Research Letters*, 48(11), 1–10. <https://doi.org/10.1029/2020GL091835>

Smetacek, V., Klaas, C., Strass, V. H., Assmy, P., Montresor, M., Cisewski, B., et al. (2012). Deep carbon export from a Southern Ocean iron-fertilized diatom bloom. *Nature*, 487(7407), 313–319. <https://doi.org/10.1038/nature11229>

Smith, W., Rivaro, P., Wang, Z., Larue, M., Heywood, K., Park, J., et al. (2021). Observational activities in the Ross Sea: Current and future national contributions to SOOS - An update (Tech. Rep.). <https://doi.org/10.5281/ZENODO.5762638>

Stammer, D., Wunsch, C., Giering, R., Eckert, C., Heimbach, P., Marotzke, J., et al. (2002). Global ocean circulation during 1992–1997, estimated from ocean observations and a general circulation model. *Journal of Geophysical Research*, 107(9), 3118. <https://doi.org/10.1029/2001jc000888>

Stephens, B. B., Keeling, R. F., Heimann, M., Six, K. D., Murnane, R., & Caldeira, K. (1998). Testing global ocean carbon cycle models using measurements of atmospheric O₂ and CO₂ concentration. *Global Biogeochemical Cycles*, 12(2), 213–230. <https://doi.org/10.1029/97GB03500>

Stock, C. A., Dunne, J. P., Fan, S., Ginoux, P., John, J., Krasting, J. P., et al. (2020). Ocean biogeochemistry in GFDL's Earth system model 4.1 and its response to increasing atmospheric CO₂. *Journal of Advances in Modeling Earth Systems*, 12(10), e2019MS002043. <https://doi.org/10.1029/2019MS002043>

Sutton, A. J., Williams, N. L., & Tilbrook, B. (2021). Constraining southern Ocean CO₂ flux uncertainty using uncrewed surface vehicle observations. *Geophysical Research Letters*, 48(3), 1–9. <https://doi.org/10.1029/2020GL091748>

Takahashi, T., Olafsson, J., Goddard, J. G., Chipman, D. W., & Sutherland, S. C. (1993). Seasonal variation of CO₂ and nutrients in the high-latitude surface oceans: A comparative study. *Global Biogeochemical Cycles*, 7(4), 843–878. <https://doi.org/10.1029/93GB02263>

Takahashi, T., Sutherland, S. C., Sweeney, C., Poisson, A., Metzl, N., Tilbrook, B., et al. (2002). Global sea-air CO₂ flux based on climatological surface ocean pCO₂, and seasonal biological and temperature effects. *Deep-Sea Research Part II Topical Studies in Oceanography*, 49(9–10), 1601–1622. [https://doi.org/10.1016/S0967-0645\(02\)00003-6](https://doi.org/10.1016/S0967-0645(02)00003-6)

Takahashi, T., Sutherland, S. C., Wanninkhof, R., Sweeney, C., Feely, R. A., Chipman, D. W., et al. (2009). Climatological mean and decadal change in surface ocean pCO₂, and net sea-air CO₂ flux over the global oceans. *Deep Sea Research Part II: Topical Studies in Oceanography*, 56(8–10), 554–577. <https://doi.org/10.1016/j.dsr2.2008.12.009>

Talley, L. (2013). Closure of the global overturning circulation through the Indian, Pacific, and southern oceans: Schematics and transports. *Oceanography*, 26(1), 80–97. <https://doi.org/10.5670/oceanog.2013.07>

Talley, L., Feely, R., Sloyan, B., Wanninkhof, R., Baringer, M., Bullister, J., et al. (2016). Changes in ocean heat, carbon content, and ventilation: A review of the first decade of GO-SHIP global repeat hydrography. *Annual Review of Marine Science*, 8(1), 185–215. <https://doi.org/10.1146/annurev-marine-052915-100829>

Tamsitt, V., Talley, L. D., Mazloff, M. R., Cerovecki, I., Cerovečki, I., Tamsitt, V., & Cerovečki, I. (2016). Zonal variations in the Southern Ocean heat budget. *Journal of Climate*, 29(18), 6563–6579. <https://doi.org/10.1175/JCLI-D-15-0630.1>

Terhaar, J., Frölicher, T. L., & Joos, F. (2021). Southern Ocean anthropogenic carbon sink constrained by sea surface salinity. *Science Advances*, 7(18), eabd5964. <https://doi.org/10.1126/sciadv.abd5964>

Terhaar, J., Frölicher, T. L., & Joos, F. (2022). Observation-constrained estimates of the global ocean carbon sink from Earth system models. *Biogeosciences*, 19(18), 4431–4457. <https://doi.org/10.5194/bg-19-4431-2022>

Terhaar, J., Goris, N., Müller, J. D., DeVries, T., Gruber, N., Hauck, J., et al. (2023). Assessment of global ocean biogeochemical models for ocean carbon sink estimates in RECCAP2 and recommendations for future studies. *Global Biogeochemical Cycles*. <https://doi.org/10.22541/essoar.168394734.41886821>

Tohjima, Y., Mukai, H., MacHida, T., Hoshina, Y., & Nakaoka, S. I. (2019). Global carbon budgets estimated from atmospheric O₂:N₂ and CO₂ observations in the western Pacific region over a 15-year period. *Atmospheric Chemistry and Physics*, 19(14), 9269–9285. <https://doi.org/10.5194/acp-19-9269-2019>

Urakawa, L. S., Tsujino, H., Nakano, H., Sakamoto, K., Yamanaka, G., & Toyoda, T. (2020). The sensitivity of a depth-coordinate model to diapycnal mixing induced by practical implementations of the isopycnal tracer diffusion scheme. *Ocean Modelling*, 154(August), 101693. <https://doi.org/10.1016/j.ocemod.2020.101693>

van der Laan-Luijkx, I. T., van der Velde, I. R., van der Veen, E., Tsuruta, A., Stanislawska, K., Babenhauserheide, A., et al. (2017). The Carbon-Tracker data assimilation shell (CTDAS) v1.0: Implementation and global carbon balance 2001–2015. *Geoscientific Model Development*, 10(7), 2785–2800. <https://doi.org/10.5194/gmd-10-2785-2017>

van Heuven, S., Hoppema, M., Jones, E. M., & de Baar, H. J. (2014). Rapid invasion of anthropogenic CO₂ into the deep circulation of the Weddell Gyre. *Philosophical Transactions of the Royal Society A: Mathematical, Physical & Engineering Sciences*, 372(2019), 20130056. <https://doi.org/10.1098/rsta.2013.0056>

Verdy, A., Dutkiewicz, S., Follows, M. J., Marshall, J., & Czaja, A. (2007). Carbon dioxide and oxygen fluxes in the Southern Ocean: Mechanisms of interannual variability. *Global Biogeochemical Cycles*, 21(2), 1–10. <https://doi.org/10.1029/2006GB002916>

Verdy, A., & Mazloff, M. R. (2017). A data assimilating model for estimating Southern Ocean biogeochemistry. *Journal of Geophysical Research: Oceans*, 122(9), 6968–6988. <https://doi.org/10.1002/2016JC012650>

Wanninkhof, R. H. (1992). Relationship between wind speed and gas exchange. *Journal of Geophysical Research*, 97(92), 7373–7382. <https://doi.org/10.1029/92jc00188>

Wanninkhof, R. H. (2014). Relationship between wind speed and gas exchange over the ocean revisited. *Limnology and Oceanography: Methods*, 12(JUN), 351–362. <https://doi.org/10.4319/lom.2014.12.351>

Wanninkhof, R. H., Asher, W. E., Ho, D. T., Sweeney, C., & McGillivray, W. R. (2009). Advances in quantifying Air-Sea gas exchange and environmental forcing. *Annual Review of Marine Science*, 1(1), 213–244. <https://doi.org/10.1146/annurev.marine.010908.163742>

Wanninkhof, R. H., Asher, W. E., Weppernig, R., Chen, H., Schlosser, P., Langdon, C., & Sambrotto, R. (1993). Gas transfer experiment on Georges Bank using two volatile deliberate tracers. *Journal of Geophysical Research*, 98(C11), 20237–20248. <https://doi.org/10.1029/93jc01844>

Wanninkhof, R. H., Park, G.-H. H., Takahashi, T. T., Sweeney, C., Feely, R. A., Nojiri, Y., et al. (2013). Global ocean carbon uptake: Magnitude, variability and trends. *Biogeosciences*, 10(3), 1983–2000. <https://doi.org/10.5194/bg-10-1983-2013>

Wanninkhof, R. H., & Triñanes, J. (2023). Impact predictor variables on magnitude, variability and trend of global air-sea CO₂ fluxes using an Extra Trees machine learning approach. *Global Biogeochemical Cycles*, 31(6), 961–974. <https://doi.org/10.1002/2016gb005592>

Watson, A. J., Schuster, U., Shutler, J. D., Holding, T., Ashton, I. G., Landschützer, P., et al. (2020). Revised estimates of ocean-atmosphere CO₂ flux are consistent with ocean carbon inventory. *Nature Communications*, 11(1), 1–6. <https://doi.org/10.1038/s41467-020-18203-3>

Waugh, D. W., Hall, T. M., Mcneil, B. I., Key, R., & Matear, R. J. (2006). Anthropogenic CO₂ in the oceans estimated using transit time distributions. *Tellus Series B Chemical and Physical Meteorology*, 58(5), 376–389. <https://doi.org/10.1111/j.1600-0889.2006.00222.x>

Waugh, D. W., Hogg, A. M., Spence, P., England, M. H., & Haine, T. W. (2019). Response of Southern Ocean ventilation to changes in midlatitude westerly winds. *Journal of Climate*, 32(17), 5345–5361. <https://doi.org/10.1175/JCLI-D-19-0039.1>

Williams, N. L., Juranek, L. W., Feely, R. A., Johnson, K. S., Sarmiento, J. L., Talley, L. D., et al. (2017). Calculating surface ocean pCO₂ from biogeochemical Argo floats equipped with pH: An uncertainty analysis. *Global Biogeochemical Cycles*, 31(3), 591–604. <https://doi.org/10.1002/2016GB005541>

Williams, N. L., Juranek, L. W., Johnson, K. S., Feely, R. A., Riser, S. C., Talley, L. D., et al. (2016). Empirical algorithms to estimate water column pH in the Southern Ocean. *Geophysical Research Letters*, 43(7), 3415–3422. <https://doi.org/10.1002/2016GL068539>

Woolf, D. K., Land, P. E., Shutler, J. D., Goddijn-Murphy, L., & Donlon, C. J. (2016). On the calculation of air-sea fluxes of CO₂ in the presence of temperature and salinity gradients. *Journal of Geophysical Research: Oceans*, 121(2), 1229–1248. <https://doi.org/10.1002/2015JC011427>

Wright, R. M., Le Quéré, C., Buitenhuis, E., Pitois, S., & Gibbons, M. J. (2021). Role of jellyfish in the plankton ecosystem revealed using a global ocean biogeochemical model. *Biogeosciences*, 18(4), 1291–1320. <https://doi.org/10.5194/bg-18-1291-2021>

Wunsch, C., & Heimbach, P. (2013). *Dynamically and kinematically consistent global ocean circulation and ice state estimates* (2nd ed., Vol. 103). Elsevier Ltd. <https://doi.org/10.1016/B978-0-12-391851-2.00021-0>

Yang, M., Smyth, T. J., Kitidis, V., Brown, I. J., Wohl, C., Yelland, M. J., & Bell, T. G. (2021). Natural variability in air-sea gas transfer efficiency of CO₂. *Scientific Reports*, 11(1), 1–9. <https://doi.org/10.1038/s41598-021-92947-w>

Yang, S., & Gruber, N. (2016). The anthropogenic perturbation of the marine nitrogen cycle by atmospheric deposition: Nitrogen cycle feedbacks and the ¹⁵N Haber-Bosch effect. *Global Biogeochemical Cycles*, 30(10), 1418–1440. <https://doi.org/10.1002/2016GB005421>

Zeng, J., Iida, Y., Matsunaga, T., & Shirai, T. (2022). Surface ocean CO₂ concentration and air-sea flux estimate by machine learning with modelled variable trends. *Frontiers in Marine Science*, 9(September), 1–14. <https://doi.org/10.3389/fmars.2022.989233>